

Studies of Climate Variability in a Simple Coupled Model

by

Claude Abiven

M.S. in Engineering Science and Mechanics
Virginia Polytechnic Institute and State University, 2002

Submitted to the Department of Earth, Atmosphere and Planetary Sciences in
partial fulfillment of the requirements for the degree of

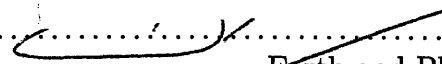
Master of Science

at the

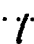
MASSACHUSETTS INSTITUTE OF TECHNOLOGY

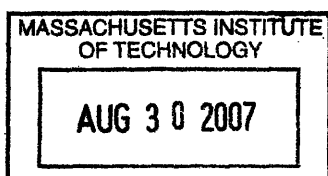
June 2007

© Massachusetts Institute of Technology 2007. All rights reserved.

Author 
Earth and Planetary Sciences
Massachusetts Institute of Technology

Certified by 
John Marshall
Professor
Thesis Supervisor

Accepted by 
Maria T. Zuber
E.A. Griswold Professor of Geophysics and Planetary Science
Department Head, Department of Earth, Atmosphere and Planetary Sciences



ARCHIVES

Studies of Climate Variability in a Simple Coupled Model

by

Claude Abiven

Submitted to the Massachusetts Institute of Technology
in partial fulfillment of the requirements for the degree of
Master of Science

Abstract

The mechanisms of variability of a coupled atmosphere-ocean model are investigated through the study of two coupled configurations: an aquaplanet in which gyres are absent, and an aquaplanet in which a ridge extending from pole to pole supports gyres. Empirical Orthogonal Functions (EOFs) are used to explore the main features of variability exhibited by extended integrations of both configurations. In the aquaplanet a decadal variability is observed in the atmosphere and the ocean. Stochastic driving of the annular modes in the atmosphere generates an anomalous Sea Surface Temperature (SST) dipole through latent heat fluxes and Ekman pumping. A feedback of this SST dipole on the atmosphere enables a damping slow enough for anomalies to persist over decadal time scales. This air-sea feedback combined with a slow advection of the anomalies by mean ocean currents result in the observed decadal oscillation. A simple stochastic model captures the essence of this mechanism. In the ridge decadal variability is absent but centennial variability is observed in the atmosphere and the ocean. Stochastic driving of the annular modes in the atmosphere generates a weak SST tripole due to latent heat fluxes. The weak amplitude of this tripole prevents the existence of any significant air-sea feedback, implies a stronger damping than in the aquaplanet, and ultimately results in the absence of oscillations. The classic stochastic model of Hasselmann [19] explains the evolution of the SST anomaly through time. Within a delay of one year stochastic atmospheric variability additionally generates a baroclinic streamfunction as well as baroclinic Rossby waves at the eastern boundary of the basin. The former is slowly advected by the mean flow while the latter propagates towards the western boundary, inducing a feedback on the atmosphere with a delay of sixty years. A simple model is found to capture the essence of this mechanism. The results of the aquaplanet and the ridge are used to interpret the Drake, a third configuration in which a band of land extends from the North Pole to the line of -45° of latitude. In the northern hemisphere of the Drake mean state and variability are similar to the ones observed in the ridge. The observed centennial oscillation would correspond to a decadal oscillation in the Atlantic. In the southern hemisphere of the Drake, mean state and variability have elements of both the ridge and the aquaplanet.

Thesis Supervisor: John Marshall
Title: Professor

Acknowledgments

In the first place, I would like to express my deepest thanks to Dr John Marshall who gave me the opportunity to come study at MIT, and whose striking ability to transmit his knowledge, relentless intellectual curiosity, and constant encouragement led me through the completion of this thesis.

I wish to show my gratitude to David Ferreira, whom I consider to be my informal second adviser for this thesis. This work would most likely be still on-going without his ceaseless pragmatism. His insightful reflections greatly improved the quality of my work.

I am also very thankful to Jean-Michel Campin and Daniel Enderton whose lively technical comments proved very valuable during the completion of this thesis.

I wish to thank Dr Claude Frankignoul for his acute remarks about this work.

I am grateful to the Department of Earth, Atmosphere And Planetary Sciences, especially to all the professors whose instructive classes and insightful discussions provided me with valuable knowledge. I also thank Mary Elliff, Carol A. Sprague, and Beth MacEachran for their kind administrative assistance.

It is not clear to me whether I would have been able to complete this work without the genuine friendship of Brian Rose, who enlightened me with his bright, deep, grounded discussions on just about everything from arduous homework to philosophical matters. I also thank my officemates and my fellow students from the department, especially Beatriz Peña-Molino who made my stay more pleasant both in and out of work.

Very special thanks to my roommates Cooper, Cornelia, Jason, Jen, Katie, MaryAnn, and Rodrigo who shared my ups and downs and enlightened my semesters in Boston.

I am very thankful for having such great friends as JP, Manu, Ronan, Carole, Virginie, Mr Alex, Mlle Kat, Mr Wi, Katja, and all the others. I would also like to thank my amazing family, especially Maman, Papa, Emmanuelle, Geneviève, Philippe, Anne, Mamie, and Papi for their affection, support, and understanding throughout all these years of studies abroad.

Finally this work shall always remind me of the love of Neda, my sweet and colorful butterfly, whose patience and tenderness rendered meaningful the life I led in Boston.

Il arrive que les décors s'écroulent. Lever, tramway, quatre heures de bureau ou d'usine, repas, tramway, quatre heures de travail, repas, sommeil et lundi mardi mercredi jeudi vendredi et samedi sur le même rythme, cette route se suit aisément la plupart du temps. Un jour seulement, le *pourquoi* s'élève et tout commence dans cette lassitude teintée d'étonnement.

Albert Camus, Le Mythe de Sisyphe

Contents

1	Introduction	8
2	Mean state of aquaplanet and ridge worlds	10
2.1	Aquaplanet and ridge worlds	10
2.2	Mean state of aquaplanet and ridge worlds	11
2.2.1	Zonal wind	11
2.2.2	Oceanic currents	12
2.2.3	Sea surface temperature	14
2.2.4	Thermocline	15
3	Variability in coupled climate models	17
3.1	Annular modes	17
3.2	Variability in gyres	20
3.2.1	Barotropic variability	20
3.2.2	Baroclinic variability	20
3.3	Sea surface temperature	23
4	Decadal variability in the aquaplanet	26
4.1	Dipole formation	26
4.2	Dipole evolution	28
4.3	Simple model	31
4.3.1	Idealized equation for the evolution of SST anomalies	31
4.3.2	Quantitative analysis	32
5	Climate variability in the ridge	35
5.1	Decadal variability in the ridge	35
5.1.1	Tripole formation	35
5.1.2	Tripole evolution	37
5.1.3	Simple model	38
5.2	Centennial variability in the ridge	43
5.2.1	Idealized model of centennial variability	48
5.2.2	Quantitative analysis	49

6	Drake	52
6.1	Mean state	52
6.2	Variability in the northern hemisphere	53
6.3	Variability in the southern hemisphere	53
7	Conclusions	57
8	Appendix	59
8.1	Power spectrum of baroclinic waves	59
8.2	Forcing of the first EOF of SST in the aquaplanet	60
8.3	Solution of the idealized coupled model in the aquaplanet	63
8.4	Forcing of the first EOF of SST in the ridge	65
8.5	Power spectrum of baroclinic waves with air-sea feedback	68
8.6	Determination of f_r from atmosphere-only runs	69
8.6.1	Forcing with the first EOF of SST in the ridge	70
8.6.2	Forcing with the second EOF of SST in the ridge	71
8.6.3	Forcing with the first EOF of SST in the aquaplanet	71

Chapter 1

Introduction

The El Niño Southern Oscillation (ENSO) is the prime example of atmosphere-ocean coupling which gives rise to interannual to decadal climate variability. However coupling is not confined to the tropics. The atmosphere and ocean can couple in middle to high-latitude and significantly impact the Earth's climate. In the North Atlantic for example, the North Atlantic Oscillation (NAO) and the Meridional Overturning Circulation (MOC) are examples of systems exhibiting decadal climate variability.

The fluctuations of the NAO are largely stochastic in time. To first order, the spectrum of the NAO is essentially white. Various components of the ocean that tend to have longer time scales than the NAO respond passively to this forcing and exhibit red spectra. For example red spectra of Sea Surface Temperature (SST) anomalies can be explained by their passive response to air-sea fluxes, as described by Hasselmann and Frankignoul [5]. But the ocean also reddens this essentially white atmospheric spectrum through a wide variety of processes affecting Sea Surface Temperature (SST), such as Rossby waves propagation (Frankignoul et al. [6] or Cessi [21]), mean flow advection (Saravanan and McWilliams [23]), ocean gyres, or thermohaline circulation (Marshall et al. [18]). To second order, these long oceanic time scales could feed back on the atmosphere through their effect on SST, possibly yielding to oscillatory modes associated with long time scales. There is increasing evidence of the existence of decadal oscillations in the oceans (Deser and Blackmon [3], Kushnir [28]), but the briefness of the instrumental record renders quite difficult the understanding of their mechanisms. Experiments making use of simple models of air-sea coupling can easily be built (Hasselmann [19], Frankignoul et al. [6]) and provide much insight. Experiments making use of complex General Circulation Models (GCMs) can also be built, as here, and provide a climate record long enough to enable the capture of phenomena associated with decadal time scales.

We choose here to use a GCM, which enables a proper simulation of the physics, but in two simple coupled configurations in order to simplify the problem and to enable a proper understanding of the underlying physics. The first configuration is an aquaplanet, i.e. a planet similar to the Earth without any land. Such an aquaplanet is a coupled system in which the ocean is set in motion by the winds through Ekman processes, but in which gyre dynamics are absent. The second configuration is a ridgeworld in which a ridge extending from pole to pole supports gyres. Since, as men-

tioned above, gyre dynamics are expected to fundamentally affect climate variability, we expect the modes of variability to be different in the two configurations.

The plan of work is as follows. In chapter 2 we present the coupled model and the two configurations: aquaplanet and ridge. We then describe the mean state in the ridge and in the aquaplanet. Wind, ocean currents, SST, and thermocline are described in turn. In chapter 3 we use Empirical Orthogonal Functions (EOFs) to study the variability in the two configurations. EOFs of zonal wind stress, barotropic and baroclinic streamfunctions, and SST are analyzed in turn. In chapter 4 we study the mode of decadal variability observed in the aquaplanet. The generation and the evolution of this mode is described using regressions of selected fields onto the Principal Components (PCs) of the EOFs of SST. A simple model in the spirit of Saravanan and McWilliams [23] is used in order to explain the essence of the mechanism. In chapter 5 we study the modes of decadal and centennial variability observed in the ridge in a similar manner to that of the aquaplanet. Simple models in the spirit of Hasselmann and Frankignoul [5] are used to explain the essence of the mechanisms. In chapter 6 we discuss whether the results of the ridge and the aquaplanet experiments can be used to interpret a third experiment, the Drake, in which the band of land extends from the North pole to the line of -45° of latitude. Finally chapter 7 provides a summary of the main results presented in this thesis.

Chapter 2

Mean state of aquaplanet and ridge worlds

2.1 Aquaplanet and ridge worlds

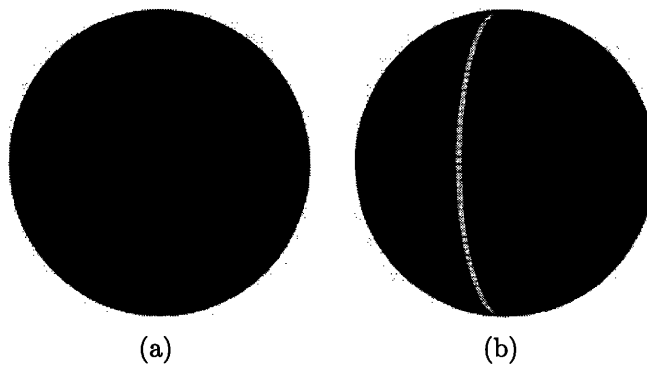


Figure 2-1: Illustration of the two cases of study: (a) aquaplanet, (b) ridge

The General Circulation Model (GCM) employed for the purpose of this work is the MITGCM (see Marshall et al. 1997 [15] [16]). In order to avoid problems associated with the convergence of meridians at the pole it is integrated forward on a cubed sphere, as proposed by Adcroft et al. [1]. Its resolution is of approximately 2.8° of latitude. The atmosphere has five vertical levels. It employs the physics package described by Molteni [11] including a four-band radiation scheme, a parametrization of moist convection and a boundary layer scheme. The absence of land in the aquaplanet simplifies the physics at stake and justifies the use of such a simplified model. These simplifications enable an integration over 1000 years in a reasonable amount of time. The ocean has a flat bottom at a depth of 5.2 kilometers defined by fifteen levels of height ranging from 50 meters at the top of the ocean to 690 meters at the bottom. Eddies are parametrized using the scheme of Gent and McWilliams [22]. A thermodynamic model of ice following Winton [20] is also used in the model.

The aquaplanet is a model of the present Earth, with the same radius, length of the day, incoming solar radiation, except there is no land, as sketched on figure 2-1(a).

This enabled Marshall et al. [17] to study the climate of a simplified system without mountain torques or land-sea contrast. Jet streams and strong temperature gradients are observed in mid-latitudes, but the ocean circulation is very different from the one observed on Earth. Indeed while the present Earth features gyres the aquaplanet features zonal jets due to the absence of boundaries, as described in section three. The ridge, sketched on figure 2-1(b) is an aquaplanet with a strip of land that extends from pole to pole (over 180°), supporting gyres and therefore an oceanic circulation somewhat more similar to the present one. This land does not feature any topography and is best viewed as a thin straight wall extending from the bottom of the ocean to the sea surface.

2.2 Mean state of aquaplanet and ridge worlds

In this section we describe the mean state in the ridge. Key differences with the aquaplanet are highlighted. The mean state, although potentially of great interest, is not the main focus of the present work and is accordingly only briefly described. Zonal wind, barotropic streamfunction and sea surface temperature are described in turn. A thousand years of simulated data were used in order to compute the time-mean patterns presented here. Zonal states are symmetric across the equator, a consequence of the symmetric setups chosen for the ridge and the aquaplanet. This is the reason why only northern hemisphere patterns are presented in the following figures. In all figures solid contours represent positive values and dashed contours represent negative values.

2.2.1 Zonal wind

It is important to highlight the differences in zonal wind observed between the ridge and the aquaplanet because the interaction between the atmosphere and ocean is mediated by the surface wind stress.

Figure 2-2(a) shows zonal winds in the ridge as a function of latitude and pressure. It exhibits strong westerly jets at $\pm 40^\circ$ of latitude, which reach a maximum of 40 m/s at a pressure level of 25 hPa. Easterlies can be noted at the poles and in the tropics, as well as weak easterlies at the equator. Figure 2-2(b) shows zonal winds in the aquaplanet. Westerly jets are now weaker, reaching a maximum of 29 m/s. This maximum is shifted 10 degrees polewards compared to the ridge. There are no easterlies at the poles.

Gyres are present in the ocean in the ridge but not in the aquaplanet (as explained below), leading to more poleward heat transport by the ocean at high latitudes in the ridge compared with the aquaplanet. This difference in heat transport is fundamentally associated with the absence of ice in the ridge and the presence of ice caps in the aquaplanet. Marshall et al. [17] provide a more detailed discussion of the mean state.

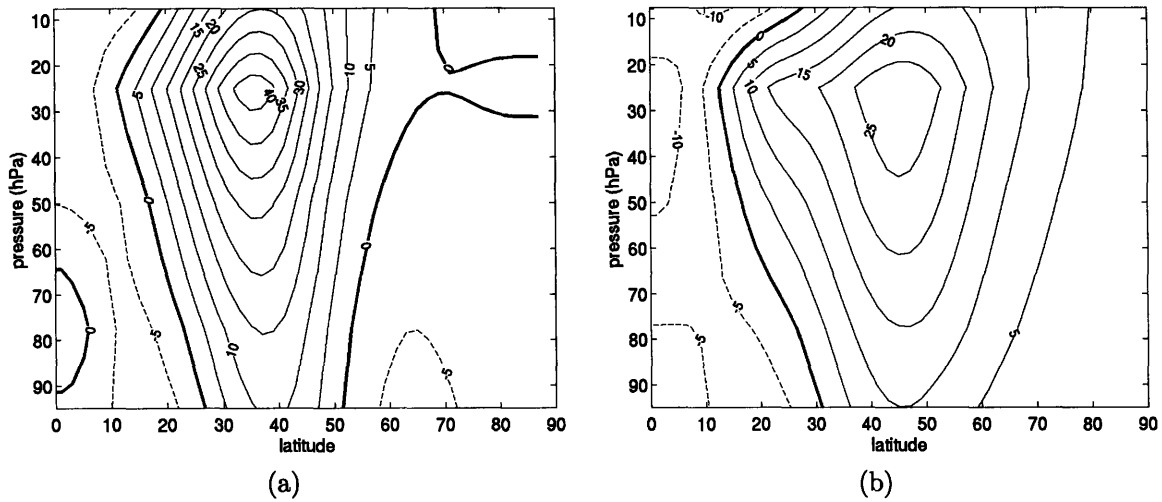


Figure 2-2: (a) zonal wind in the ridge as a function of latitude and pressure, in units of m/s. (b) same as (a) for the aquaplanet

2.2.2 Oceanic currents

Figure 2-3(b) shows the barotropic (i.e. integrated over the depth of the ocean) streamfunction in the ridge. Note that the ridge is located at 0° of longitude and extends from pole to pole (over 180°). The contours are streamlines for the flow and are expressed in Sverdrups ($1Sv = 10^6 m^3/s$). Positive and negative values correspond respectively to anticyclonic and cyclonic gyre circulations. The pattern sketched in figure 2-3(b) exhibits a strong anticyclonic subtropical gyre (from 15 to 40° of latitude) which reaches a maximum value of about $100Sv$ at the western boundary, a cyclonic subpolar gyre (from 40 to 65° of latitude) of similar strength, and a weaker anticyclonic polar gyre.

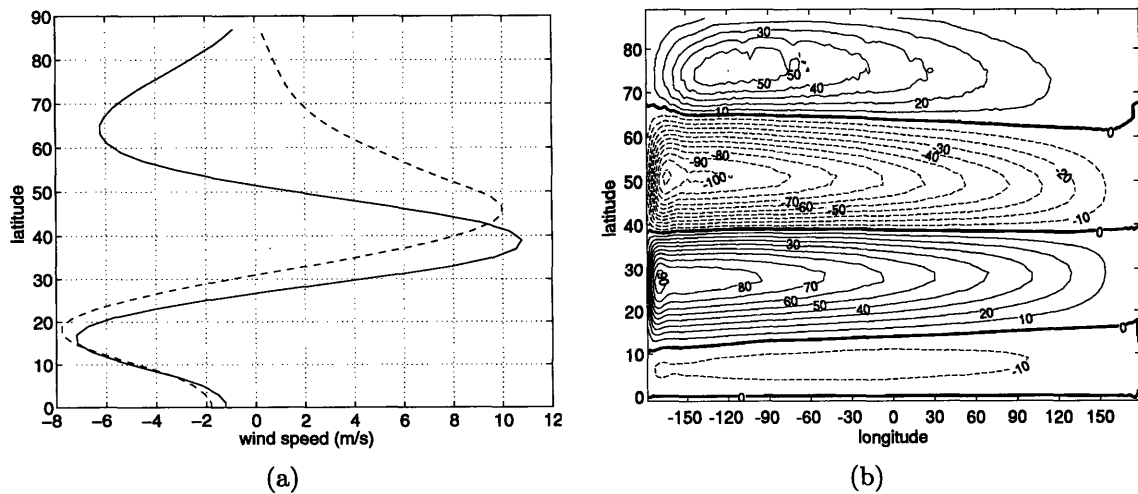


Figure 2-3: (a) surface winds as a function of latitude (vertical axis) in the aquaplanet (dashed line) and the ridge (solid line); units are m/s . (b) barotropic streamfunction on the lat-long grid, in units of Sv

Sverdrup [13] provided an estimation of the strength of oceanic gyres:

$$\beta \frac{\partial \Psi}{\partial x} = \frac{\text{curl}_z(\vec{\tau})}{\rho_0 D} \quad (2.1)$$

where β is the derivative of the Coriolis parameter with respect to latitude, Ψ is the barotropic streamfunction, τ is the wind stress, ρ_0 is the mean density of the water, D is the depth of the ocean, and curl_z is the z-component of the curl. To compute $\Psi(x)$ it is thus necessary to integrate equation (2.1) from the eastern boundary (where $\Psi = 0$) to x . Because the wind does not vary much with longitude, Ψ is expected to vary almost linearly from east to west. Latitudes where the wind reaches a minimum are thus expected to coincide with a minimum of the streamfunction, and vice-versa. Figure 2-3(a) and 2-3(b) show that this is indeed the case. Latitudes where the wind gradient reaches an extremum are expected to coincide with zeros for the streamfunction. This is also confirmed by figures 2-3(a) and 2-3(b). However computation of Ψ from equation(2.1) yields values twice as high as the ones observed in figure 2-3(b) because of losses due to friction and viscosity in the interior. The latter was found to account for 85% of the losses. The very existence of gyres requires the presence of a western boundary, where a western boundary flow closes the circulation as investigated by Stommel [12] and Munk [27]. Indeed while gyres are present in the ridge, a zonal flow is observed in the aquaplanet.

Figure (2-4) shows the difference between the time-mean SST and the time-mean zonally averaged SST on which were superimposed contour lines of the time-mean barotropic streamfunction in the ridge. At the western boundary a warm anomaly extends from 30° to 40° of latitude. It is explained by the anticyclonic subtropical gyre which advects warm water polewards at the western boundary. At the eastern boundary a cold SST anomaly is observed, which is explained by the anticyclonic subtropical gyre advecting cold water southwards. Similarly from 40° to 60° of latitude the cyclonic subpolar gyre advects cold waters southwards at the western boundary and warm waters poleward at the eastern boundary.

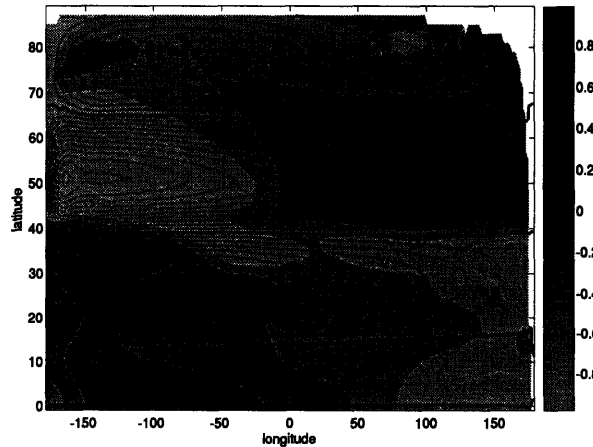


Figure 2-4: SST minus zonally averaged SST (filled contours, contour intervals are $0.5^\circ C$) and barotropic streamfunction (black contour lines, contour intervals are $10 Sv$) in the ridge

Figure 2-5(a) shows the time-mean zonal velocity at the surface of the ocean in the aquaplanet. It consists in a zonal pattern negative to the south of the line of 30° of latitude and positive to the north of this line. Velocities reach an extremum of $-0.8m/s$ at the equator and a maximum of $0.1m/s$ in middle latitudes. In this case the Sverdrup relation given by equation (2.1) is not valid anymore since the derivatives in x are essentially 0 due to the zonal configuration of the aquaplanet. Instead there exists an equilibrium between zonal wind stress and losses due to friction, so that ocean currents flow in the same sense as the stress applied at the surface. In the aquaplanet the easterlies observed below the line of 30° of latitude and the westerlies observed above this line explain the pattern of figure 2-5(a).

It will be seen below that residual circulation plays a role in the advection of SST anomalies in the aquaplanet. For this reason the zonally averaged residual circulation in the ocean of the aquaplanet is sketched in figure 2-5(b). We merely observe northwards currents to the south of the line of 35° of latitude and southwards currents to the north of this line. Marshall et al. [17] provide a more in-depth study of this pattern.

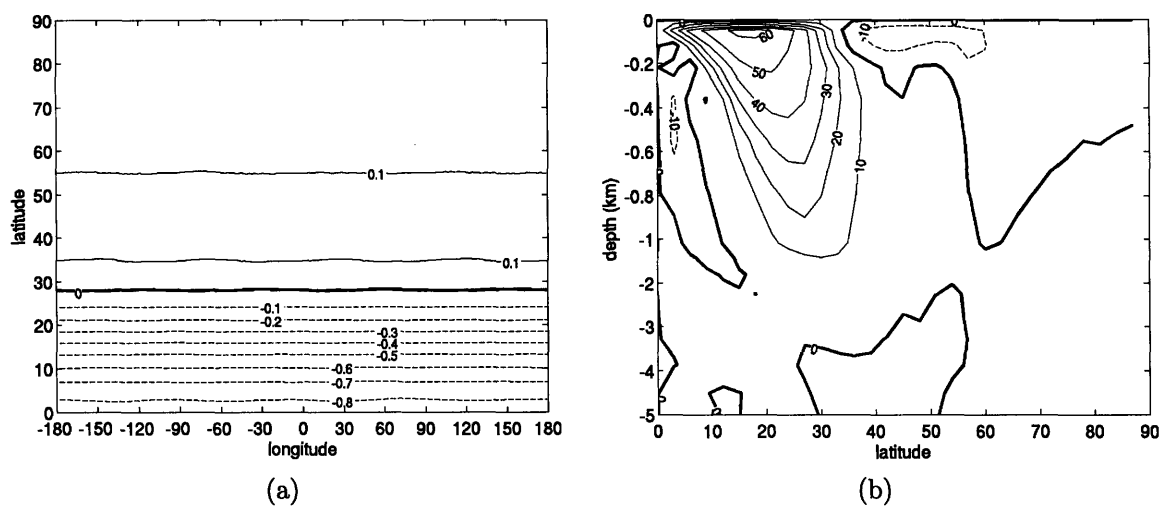


Figure 2-5: (a) time-mean zonal velocity in the first 50m of the ocean in the aquaplanet, in m/s (b) zonally averaged residual circulation in the ocean in the aquaplanet. Units are Sv

2.2.3 Sea surface temperature

Figure 2-6(a) shows the SST distribution in the ridge. The pattern corresponds to a negative equator to pole gradient: temperatures range from $34^\circ C$ at the equator to $10^\circ C$ at the poles. In the ridge gyres transport heat towards the poles and thus prevent the presence of ice there. The temperature gradient appears stronger at mid-latitudes and is not zonal. At the western boundary isentropes are advected by the gyres described above: in between 15 and 40° of latitude the anticyclonic subtropical gyre advects isentropes northwards at the western boundary and southwards in the interior. Above 40° of latitude the cyclonic subpolar gyre tilts the isentropes southwards at the western boundary and northwards in the interior. Figure 2-6(b) shows the SST

in the aquaplanet. As in the ridge, a negative equator to pole gradient is observed. However, the SST pattern is zonal due to the absence of gyres. Temperatures reach 0°C slightly below the 60^{th} parallel which delimits the ice line. The absence of gyres in the ocean thus coincides with the presence of ice at the poles in the aquaplanet. This emphasizes the significance of the amount of heat transported by gyres in the ocean.

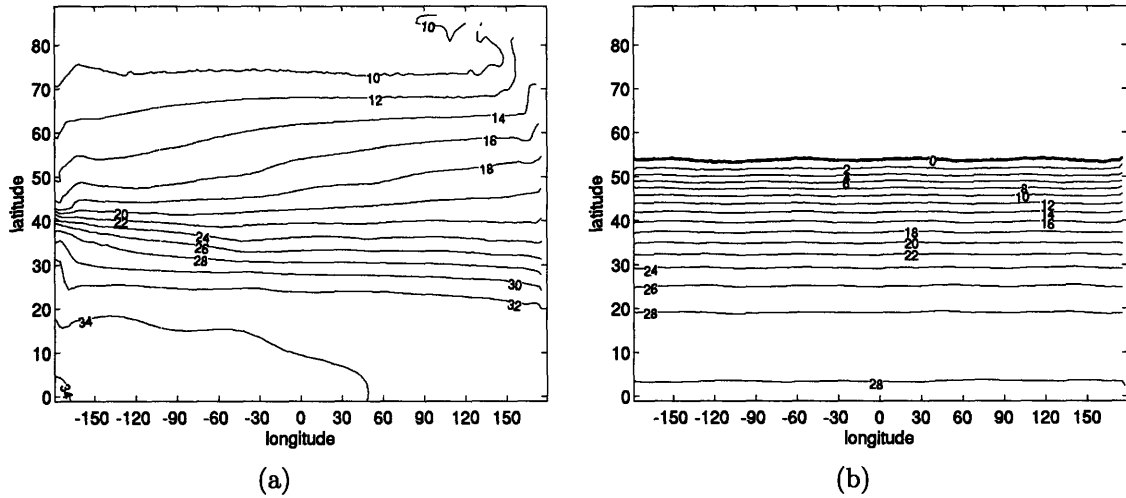


Figure 2-6: (a) mean sea surface potential temperature in the ridge, in units of $^{\circ}\text{C}$. (b) same as (a) for the aquaplanet

2.2.4 Thermocline

Figure 2-7(a) shows the contours of time-mean zonally-averaged potential temperature in the ocean in the ridge. A high temperature gradient is observed from the equator to the line of 50° of latitude, down to a depth of 1km . Below this depth and at higher latitudes the temperature gradient is weaker. A lens of warm water penetrates downwards from 10° to 40° of latitude. This feature is associated with Ekman pumping at these latitudes and Ekman suction at the equator. A deep convective region is observed over the poles. The thermocline in the ridge is thus quite similar to the one observed on Earth.

Figure 2-7(b) shows the contours of time-mean zonally-averaged potential temperature in the ocean in the aquaplanet. A warm lens of fluid penetrates downwards from a few degrees above the equator to 50° of latitude, down to a depth of 2km . At the poles, below the ice sheet, a temperature inversion can be noted which was found to be salinity-compensated. The steepest slope of the isotherms in the aquaplanet is in accordance with higher values of the barotropic streamfunction there.

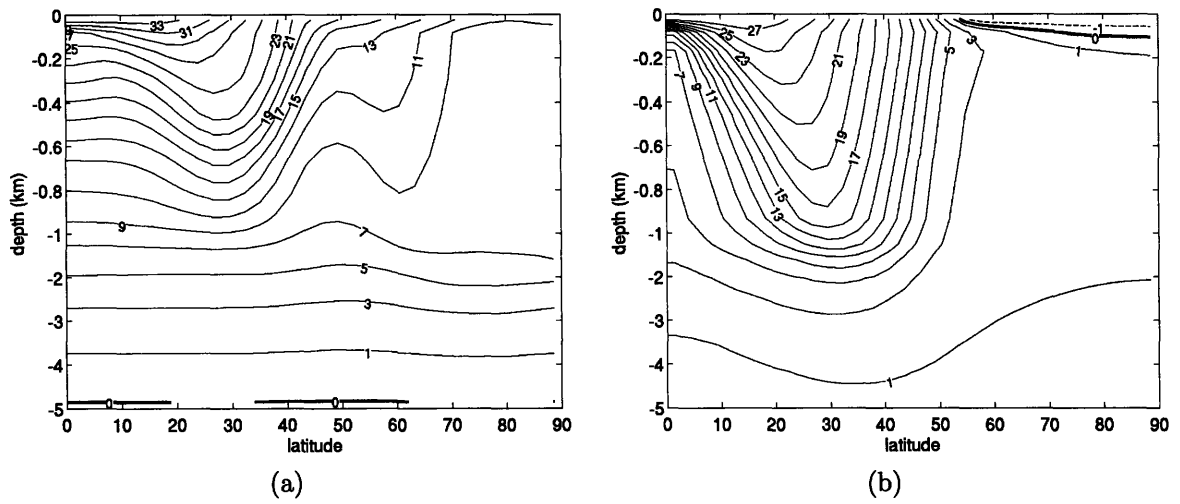


Figure 2-7: (a) time mean zonally-averaged potential temperature in the ocean in the ridge, in units of $^{\circ}C$. (b) same as (a) for the aquaplanet

Chapter 3

Variability in coupled climate models

Modes of variability of zonal wind, barotropic and baroclinic streamfunctions and SST were computed from an EOF analysis. For each field a thousand years of annually averaged fields was used. Note that the analysis was performed on the northern hemisphere only ($0^{\circ}N$ to $90^{\circ}N$).

3.1 Annular modes

Figure 3-1(a) shows the pattern of the first EOF of zonal wind speed in the ridge as a function of latitude and pressure. It accounts for more than eighty percent of the variance, and exhibits a dipole centered at 39° of latitude which extends from 15° to 75° . It reaches extrema of 1 and $2m/s$ at the ground at latitudes of 27° and 49° . This dipole corresponds to a meridional *wobbling* of the zonal jet. Its variability is internal to the atmosphere. Figure 3-1(c) shows the pattern of the first EOF of zonal wind stress in the ridge on the lat-long grid. It shows that the structure of the previously described dipole is zonal. Figure 3-2(a) shows the power spectrum associated with the first PC of zonal wind stress. The spectrum appears to be almost white, although a least square fit exhibits a power law in $s^{-0.35}$. We will thus say that the annular mode in the ridge exhibits a *slightly red* spectrum. Note that a power law in $s^{-0.22}$ was for instance found by Wunsch [7] using an index of the North Atlantic Oscillation (NAO). Figure 3-2(c) shows the auto-correlation of the first PC of zonal wind stress. It consists in a sharp peak, a signature of low persistence of the signal. Indeed the signal shows almost no correlation at lags exceeding one year. This auto-correlation confirms that we are in the presence of (slightly reddened) white noise.

Figure 3-1(b) presents the pattern of the first EOF of zonal wind speed in the aquaplanet as a function of latitude and pressure. It accounts for 69% of the variance and shows a dipole wider than in the ridge since it now extends to the pole. This reflects the absence of easterlies at the pole in the aquaplanet that was previously discussed using figure (2-2). The dipole exhibits weaker extrema than in the ridge, although this difference is small at the surface. This is once more consistent with

the mean state, which showed weaker winds in the aquaplanet, but of comparable strength at the surface. As in the ridge the structure of the first EOF of zonal wind stress at the ground is zonal, as shown by figure 3-1(d). The power spectrum corresponding to the first PC of zonal wind is given by figure 3-2(b). The spectrum is almost white with a peak at a period of twelve years. A power law in $s^{-0.13}$ was found to best fit the data, indicating a more white spectrum than in the ridge. The auto-correlation (figure 3-2(d)) shows a sharp peak, a signature of white noise, and weak low-frequency lobes indicating a decadal oscillation, consistently with the peak observed in the power spectrum. This features were analyzed in detail in the work by Marshall et al. [17].

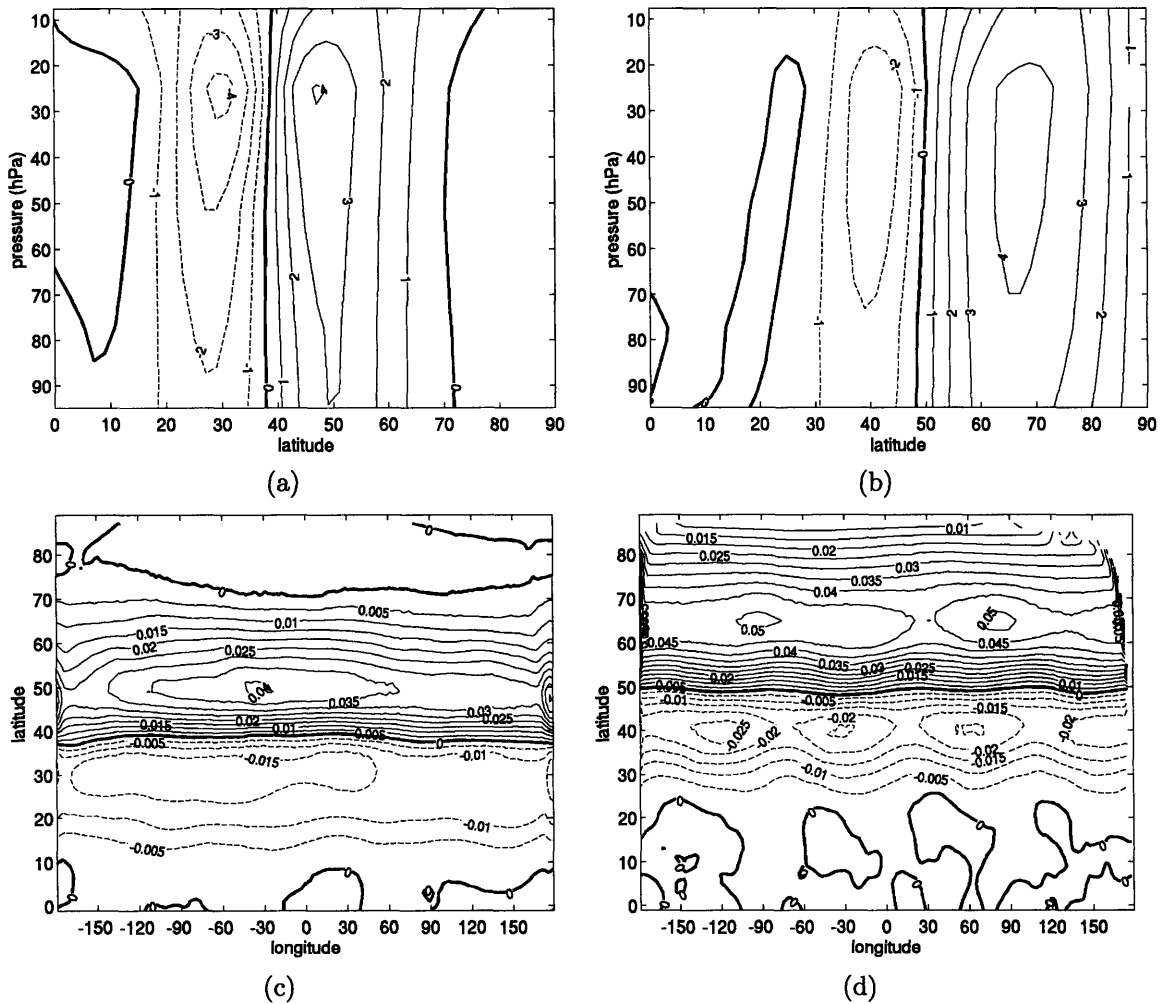


Figure 3-1: (a) pattern of the first EOF of zonal wind in the ridge as a function of latitude and pressure, in units of m/s . (b) same as (a) for the aquaplanet. (c) pattern of the first EOF of zonal wind stress in the ridge as a function of longitude and latitude. Units are N/m^2 . (d) same as (c) for the aquaplanet.

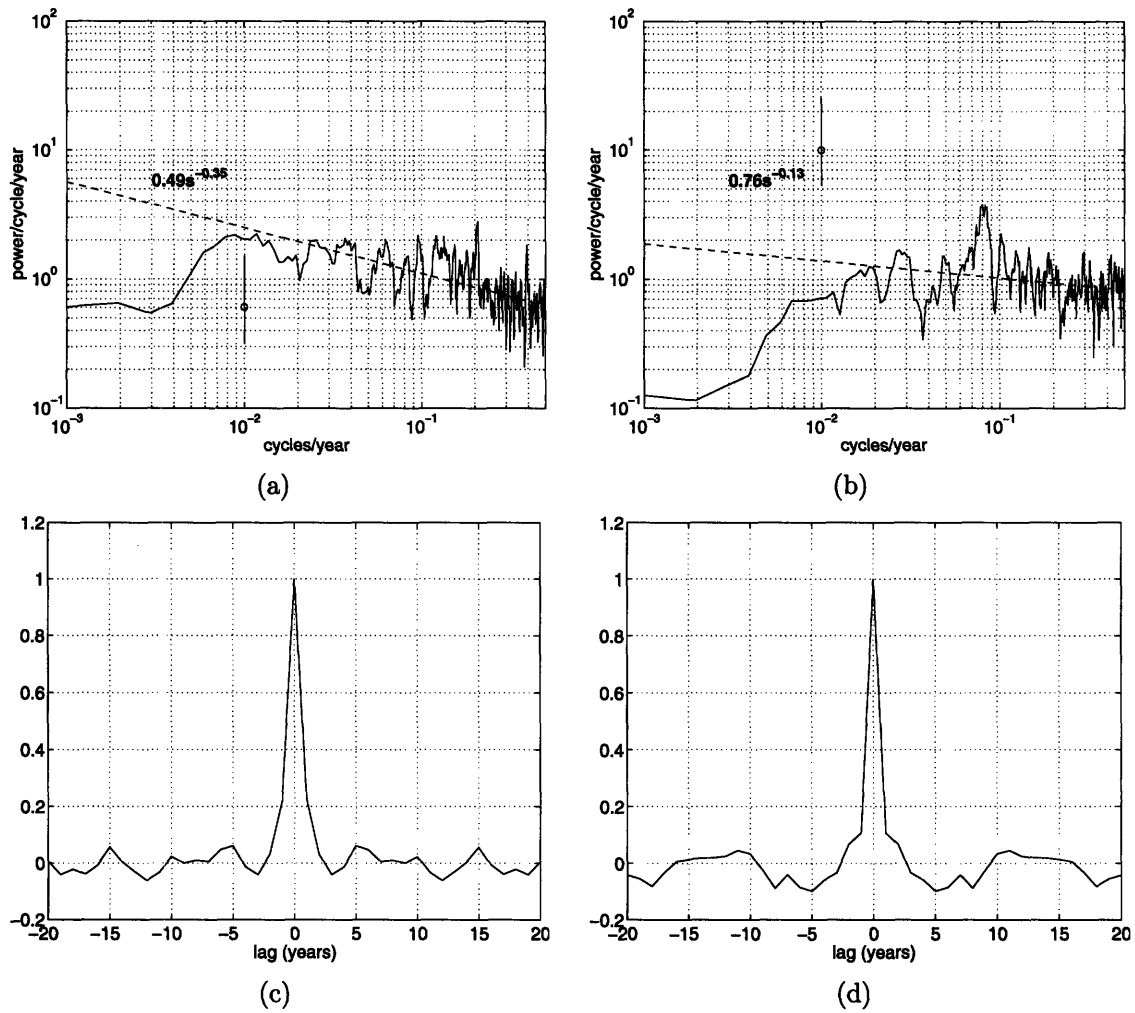


Figure 3-2: (a) power spectrum corresponding to the first EOF of zonal wind stress in the ridge (a 95% confidence interval is shown). (b) same as (a) for the aquaplanet. (c) corresponding auto-correlation in the ridge. (d) same as (c) for the aquaplanet

3.2 Variability in gyres

3.2.1 Barotropic variability

The first EOF of the barotropic streamfunction is shown in figure 3-3(a). It explains 86% of the variance and exhibits three anomalous gyres. A first gyre circulates cyclonically from 50° of latitude to the pole and reaches a maximum of 25*Sv* at the western boundary. A second gyre circulates anticyclonically from 20° to 50° of latitude with an observed minimum of -25*Sv*. A third weaker anticyclonic gyre appears in the tropics. These gyres seem to straddle between the time-mean gyres observed in the ridge (figure 2-3(b)) and hence to correspond to gyres forced north and south by the meridional *wobbling* of the zonal jet. These anomalous gyres were discussed by Marshall et al. [18] in the context of NAO forcing of the Atlantic, and denominated as *intergyre gyres*.

Can these anomalous gyres be explained by anomalous surface winds? If the wind was driving these anomalous gyres, we would expect a wind extremum to coincide with a 0 of the streamfunction (from Sverdrup's theory). In fact this happens at 50° of latitude. However the wind maximum at 29° of latitude does not coincide with a 0 of the streamfunction which appears to be shifted southwards by 9° of latitude. Similarly we expect the 0 wind anomaly line to coincide with an extremum of the streamfunction. This appears to be the case for the two main gyres. Computation of Ψ from the Sverdrup relation (2.1) using the first EOF of zonal wind stress yields values higher than the one observed in figure 3-3(a) by a factor of 3 to 1.5 for the subtropical and subpolar gyres respectively. In the latter case this difference is accounted for by friction and viscosity in the interior. In the case of the subtropical gyre however, only half of this difference is accounted for by friction and viscosity. It therefore seems that anomalous ocean gyres and anomalous wind patterns are closely related, although non-linear effects might be significant in the case of the subtropical gyre.

The power spectrum corresponding to the first EOF of the barotropic streamfunction is shown in figure 3-3(b). If we compare it to the power spectrum corresponding to the first EOF of zonal wind stress (figure 3-1(c)) we see that they are very similar. How similar? A coherence analysis (not shown) shows a very strong correlation of almost 1 at all frequencies between the two PCs. This strong correlation confirms that the barotropic signal responds very fast to the wind, as expected.

3.2.2 Baroclinic variability

A baroclinic signal was computed from the model using the hydrostatic pressure at a depth of 200*m*. This signal was then used as a streamfunction Ψ_c defined as:

$$\Psi_c = \frac{h}{\rho f} P_c \quad (3.1)$$

where P_c is the barotropic pressure, ρ the density of water, f the Coriolis parameter, and h the depth of the mixed layer.

The pattern of the first EOF of the baroclinic streamfunction is sketched in figure

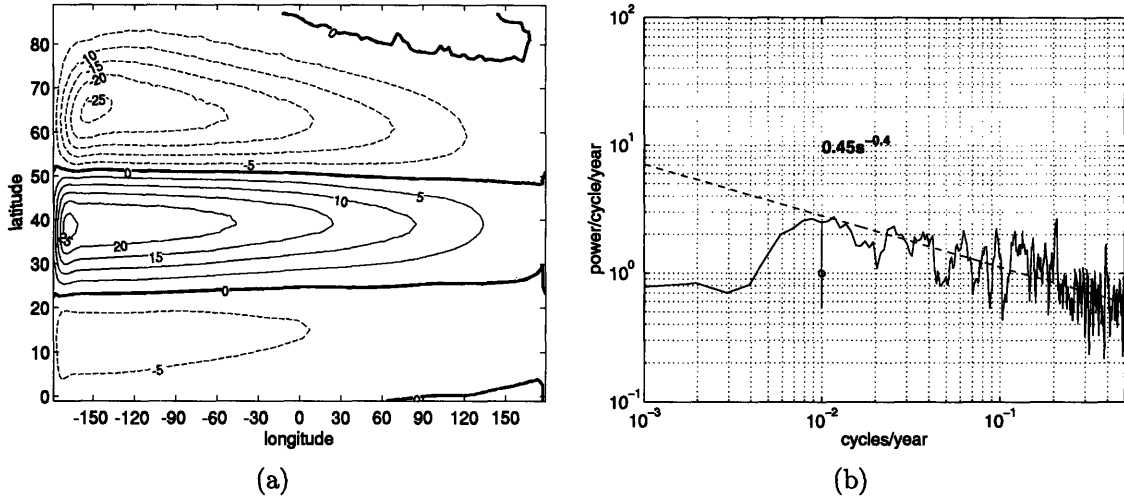


Figure 3-3: (a) pattern of the first EOF of the barotropic streamfunction in the ridge, in units of Sv . (b) corresponding power spectrum (a 95% confidence interval is shown)

3-4(a). It was found to account for 27% of the variance. It exhibits an anticyclonic gyre from 20° to 50° of latitude which reaches values of the order of $0.5Sv$ at the western boundary. A weaker cyclonic gyre extends from 50° to 75° of latitude and reaches maximum values of $0.1Sv$. The power spectrum is much *redder* than in the barotropic case, with a $s^{-2.4}$ slope at high frequencies (compared to $s^{-0.4}$ in the barotropic case).

Frankignoul, Müller, and Zorita [6] predicted that *baroclinic spectra are red with a high-frequency ω^{-2} decay that levels off at low frequency*. They considered the equation for forced baroclinic long waves proposed by White [26]:

$$\frac{\partial \Psi_c}{\partial t} + c_r \frac{\partial \Psi_c}{\partial x} = \text{curl}_z \left(\frac{\tau}{\rho_0 h} \right) \quad (3.2)$$

where Ψ_c is the baroclinic streamfunction, $c_r = -\beta L_\rho^2$ is the wave speed of long Rossby waves, L_ρ is the oceanic deformation radius, β the meridional gradient of the Coriolis parameter, τ the wind-stress and h the mean thickness of the upper layer. Solving for this equation in the Fourier domain (see appendix) using the appropriate boundary conditions yields the expression for the power spectrum:

$$\Phi_c(\omega) = \hat{\Psi}_c \hat{\Psi}_c^* = \frac{4\hat{F}_\tau^2}{\omega^2} \sin^2\left(\frac{\omega x}{2c_r}\right) \quad (3.3)$$

where ω is the frequency. At high frequencies the power spectrum of the baroclinic streamfunction is thus expected to follow a power law in s^{-2} . This explains the high frequency slope observed in figure 3-4(b). The auto-correlation of the first PC of the baroclinic streamfunction is sketched in figure 3-4(c)). It shows a large peak extending from lag 0 to lag 50 years, as well as a low-frequency oscillation of period 120 years. The large peak extending from lag 0 to lag 50 years indicates a long persistence of the signal. This was expected since the baroclinic signal is linked to the long time scale

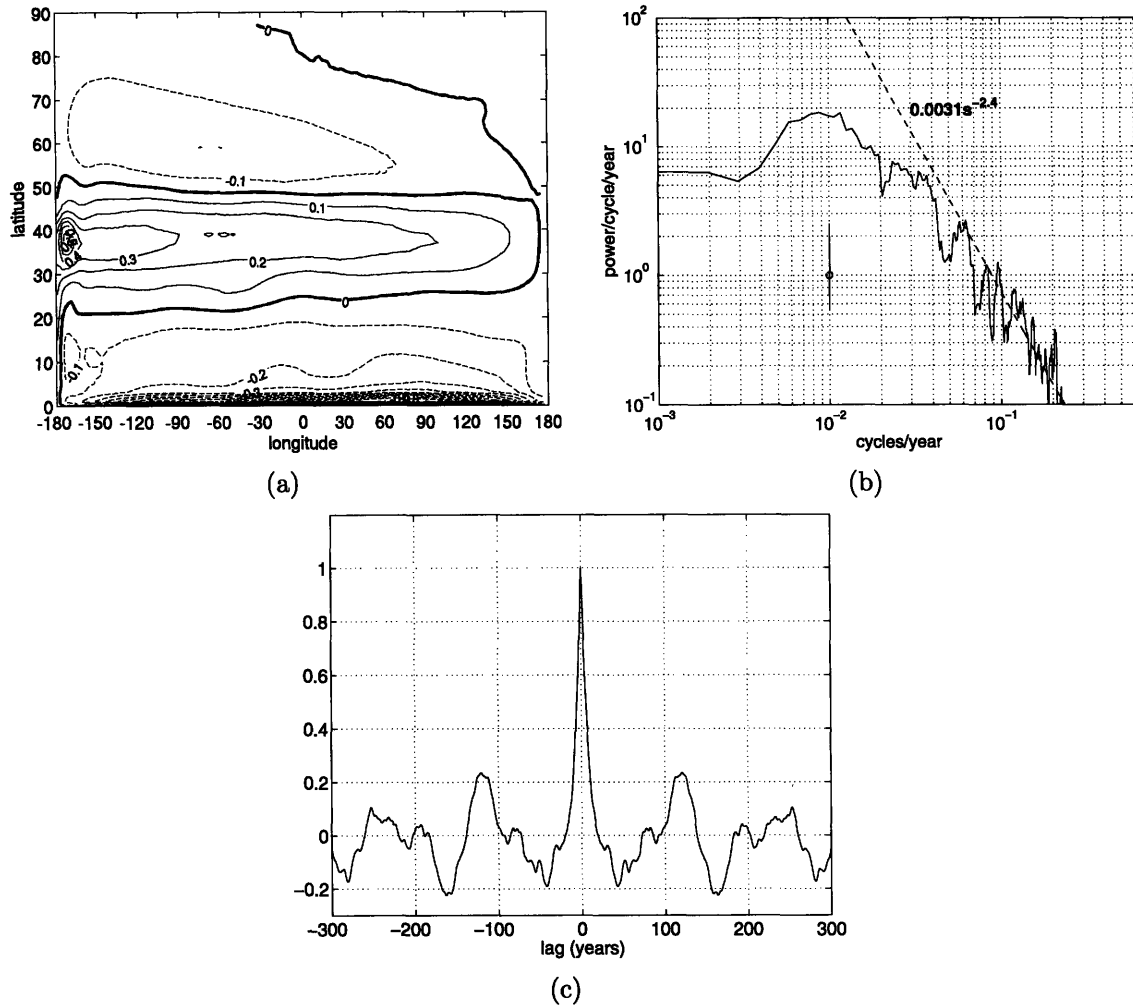


Figure 3-4: (a) pattern of the first EOF of the baroclinic streamfunction in the ridge, in units of Pa . (b) corresponding power spectrum (a 95% confidence interval is shown). (c) corresponding auto-correlation

adjustment induced by slow baroclinic Rossby waves. The low-frequency oscillation indicates the existence of a preferred frequency. The autocorrelation corresponding to equation (3.3) is obtained by taking the inverse Fourier transform of the power spectrum, which yields:

$$A(x, t) = \frac{c_r F}{x} \Lambda \left(\frac{tc_r}{x} \right) \quad (3.4)$$

Λ is the triangular function defined as:

$$\Lambda(t) = \begin{cases} 1 - |t| & \text{if } |t| < 1 \\ 0 & \text{if } |t| > 1 \end{cases} \quad (3.5)$$

We therefore expect this autocorrelation to be a triangular function reaching 0 at lag $\frac{x}{c_r}$. This model thus does not explain the centennial oscillations observed in the ridge experiment. We return to a discussion of possible mechanisms that can account

for this signal in section 5.2.

3.3 Sea surface temperature

Figure 3-5(a) presents the pattern of the first EOF of SST in the case of the ridge. It accounts for 30% of the variance. A tripole centered at 30° of latitude is clearly visible, which seems to be advected northwards at the western boundary. The southern part of this tripole reaches a minimum value of -0.2°C . The central part of this tripole reaches a maximum value of 0.2°C in the interior. The northern part of this tripole covers a larger area than the southern one and reaches a minimum value of -0.3°C in the interior. Note that such a tripole is observed in the real world at similar latitudes in the North Atlantic (see for instance Seager et al. [24]).

The power spectrum of the first PC of SST anomalies is sketched in figure 3-5(c). Monthly data were used in order to accurately show the high-frequency slope. Indeed when yearly data was used the power spectrum seemed to be fitted by a power law in s^{-1} at high frequencies due to the absence of data at these frequencies. Note that monthly data yield EOF and cross-correlation patterns similar to the ones obtained with yearly data. The power spectrum shows a plateau at frequencies higher than 0.03 cycles/year, and a linear slope corresponding to a power law in s^{-3} at high frequencies. The signal is therefore white at low frequencies, and red at high frequencies. Its shape of a plateau followed by a linear slope is reminiscent of the Frankignoul-Hasselmann [5] model except with a slope closer to s^{-3} rather than s^{-2} as suggested by Frankignoul and Hasselmann. Accordingly the cross-correlation function (figure 3-5(e)) shows a peak at small lags and weak values at decadal time scales. There is thus no sign of low-frequency variability in this case.

Figure 3-5(b) shows the pattern of the first EOF of SST in the aquaplanet which explains 18% of the variance. It exhibits a north-south dipole at 35 and 50° of latitude. This dipole reaches a maximum value of 0.2°C in the south and a minimum value of -0.8°C in the north. This EOF is thus stronger in amplitude than the EOF found in the ridge. The power spectrum resulting from this first EOF is shown by figure 3-5(d). Monthly data were used as in the case of the ridge. It is similar to the power spectrum obtained in the ridge, with a plateau at low frequencies and a linear slope fitted by a power law in s^{-3} at high frequencies. However a bump can be observed on this plateau at decadal time scales and another at yearly time scales. The former appears in the auto-correlation sketched in figure 3-5(f) in which low-frequency lobes are clearly visible and show decadal timescales of variability. The second and third EOFs in the aquaplanet were found to be wavy patterns accounting for 7% of the variance. The fourth EOF was found to account for 7% of the variance. It is a dipole that resembles the first EOF of SST both in shape and time-variation. Thus the first EOF of SST is chosen as a representation of the variability in the aquaplanet in the following.

Figure 3-6(a) shows the pattern of the second EOF of SST in the ridge. It accounts for 7% of the variance, compared to 30% for the first EOF of SST. Its main feature is an anomalous blob that extends from 40° to 60° of latitude over half the width of the

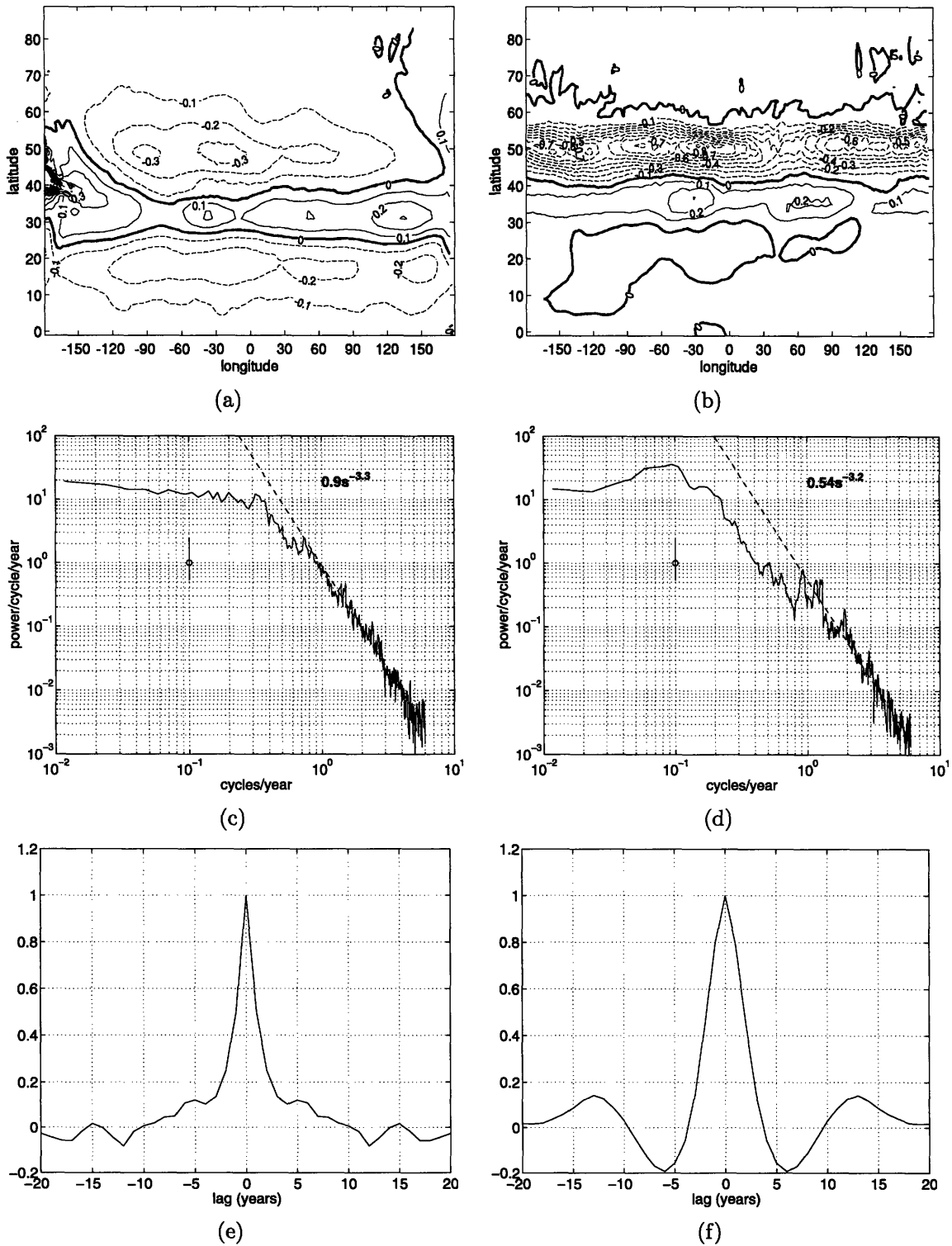


Figure 3-5: (a) pattern of the first EOF of SST in the ridge, in units of $^{\circ}C$. (b) same as (a) for the aquaplanet. (c) corresponding power spectrum in the ridge (a 95% confidence interval is shown). Monthly data were used in this case. (d) same as (c) for the aquaplanet. (e) corresponding auto-correlation in the ridge. (f) same as (e) for the aquaplanet

basin, and that reaches a maximum value of 0.3°C there. A weaker signal of opposite sign can be noted from 20° to 40° , reaching an extremum value of -0.05°C at the western and eastern boundaries. Finally a third positive anomalous band is visible in the neighborhood of the line of 70° of latitude. The auto-correlation of the second PC of SST in the ridge is sketched in figure 3-6(b). It exhibits a large peak from lag 0 to lag 50 years and an oscillation of period 120 years. This auto-correlation is very similar to the one obtained in the case of the baroclinic streamfunction discussed in section 3.2.2. Thus the second EOF of SST is very likely to be induced by the baroclinic streamfunction. We expect the anticyclonic baroclinic gyre of figure 3-4(a) to induce a warm water anomaly to the north of the line of 40° of latitude, and a cold water anomaly to the south of this line. This is what is observed in the pattern of the second EOF of SST, although the observed anomaly is weaker in the south than in the north. When using data averaged over 10 years the second EOF of SST in the ridge is found to explain 15% of the variance, compared to 37% for the first EOF of SST. At sufficiently low frequencies the second EOF of SST is hence significant. In the ridge it is thus the second EOF of SST which captures the low-frequency variability of the system.

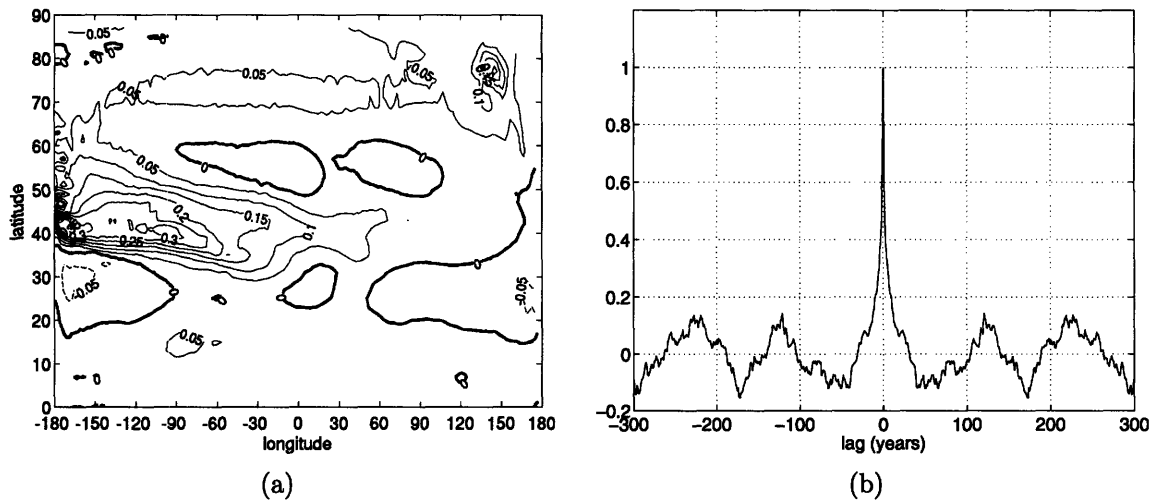


Figure 3-6: (a) pattern of the first EOF of SST in the ridge, in units of $^{\circ}\text{C}$. (b) corresponding auto-correlation

Chapter 4

Decadal variability in the aquaplanet

4.1 Dipole formation

In the aquaplanet the pattern of the first EOF of SST is a dipole, as shown by figure 3-5(b). In order to understand the mechanisms that influence this dipole, we compute the terms of the SST equation:

$$\frac{\partial T'}{\partial t} + \overline{\mathbf{u}_g} \cdot \nabla T' + \mathbf{u}'_g \cdot \nabla \overline{T} = Q' - \overline{\mathbf{u}_{Ek}} \cdot \nabla T' - \mathbf{u}'_{Ek} \cdot \nabla \overline{T} \quad (4.1)$$

In this equation bold characters represent vectors, overbars represent time means, and primes represent anomalies. T is the SST, \mathbf{u} the velocity vector, Q the air-sea heat flux, and subscripts g and Ek denote respectively the geostrophic and Ekman components of the velocity. \mathbf{u}_{Ek} is thus defined as $\left(\frac{\tau'_y}{\rho_o f}, -\frac{\tau'_x}{\rho_o f_o}, \frac{1}{\rho_o} \left(\frac{\partial \tau'_y}{\partial x f_o} - \frac{\partial \tau'_x}{\partial y f_o} \right) \right)$, where ρ_o is the water density, τ the surface wind stress and f_o the Coriolis parameter. Each term of equation (5.1) was regressed onto the first PC of SST with a lag of two months. Each term could thus be visualized two months before the SST tripole anomaly was formed. In the aquaplanet two terms were found to be significantly larger than the others: the Ekman forcing $\frac{C_o \tau'_x}{f_o} \frac{\partial \overline{T}}{\partial y}$ and the air-sea heat flux Q' . The others were orders of magnitude smaller. In particular Ekman pumping was found to be negligible.

Figure 4-1(a) shows the Ekman forcing term. It is a dipole centered on the line of 50° of latitude and extending from 30° to 60° of latitude. This dipole is positive in the south and negative in the north and reaches extremum values of respectively $+3W/m^2$ and $-4W/m^2$. A dipole was expected from the pattern of the first EOF of wind stress anomaly (figure 3-1(d)). The anomalous wind stress pattern exhibits eastward winds to the north and westward winds to the south which result (in the northern hemisphere) in a southwards Ekman transport in the north and a northwards Ekman transport in the south. This induces a negative Ekman anomaly in the north and a positive anomaly to the south, in accordance with the pattern of figure 4-1(a). Because ice shields the ocean from the wind above the line of 55° of latitude the

maximum eastwards wind stress that influences Ekman transport is only $0.03N/m^2$ while the maximum westwards wind stress is $-0.025N/m^2$ (see figure 3-1(d)). Since the temperature gradient at these latitudes is more or less constant with latitude the Ekman forcing pattern is therefore a dipole which is almost antisymmetric.

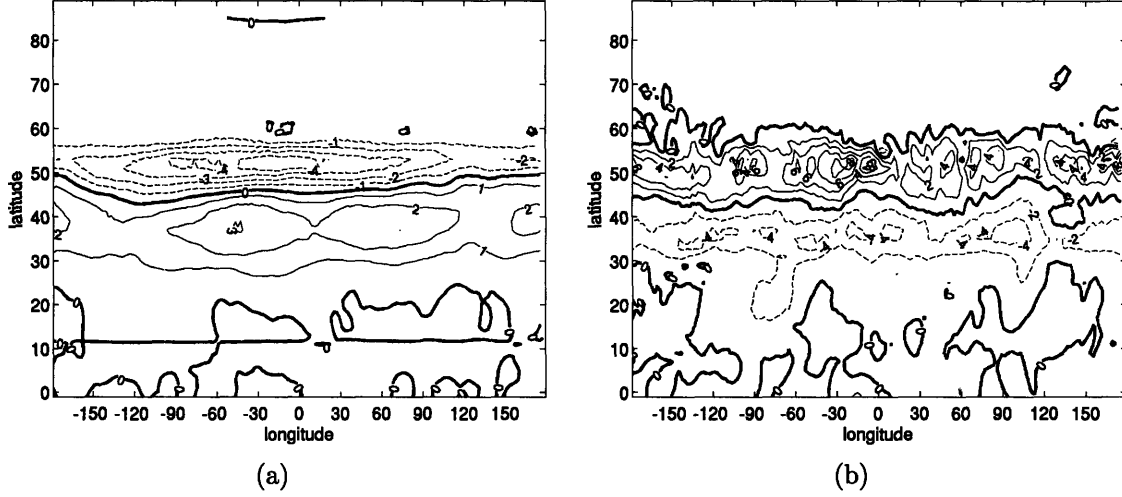


Figure 4-1: (a) regression of the Ekman anomaly $\frac{C_o \tau'_x}{f} \frac{\partial \bar{T}}{\partial y}$ onto the first PC of SST at lag 2 months (two months before the SST pattern materializes) in the aquaplanet. Units are W/m^2 and positive fluxes are downwards. (b) regression of the heat flux onto the first PC on SST at lag 2 months in the aquaplanet. Units are W/m^2 and positive fluxes are downwards

The heat flux term Q' is sketched in figure 4-1(b) where positive fluxes were chosen to indicate a flux from the atmosphere towards the ocean. It consists in a dipole centered on the line of 45° of latitude and that extends from 30° to 60° of latitude. It is negative in the south and positive in the north and reaches extremum values of -4 and $+8W/m^2$ there. Since the signs of this dipole are opposite to the ones of the first EOF of SST, heat fluxes contribute to a damping of the SST.

In the following we attempt to better understand this heat flux pattern by decomposing it into its various components. The total heat flux can be written as the sum of latent, sensible, longwave and shortwave fluxes:

$$Q = Q_{La} + Q_{Se} + Q_{LW} + Q_{SW} \quad (4.2)$$

These fluxes were regressed on the first PC of SST with a lag of two months. Latent and sensible heat fluxes were found to be the dominant ones, as in several studies making use of real data (see for example Sterl at al. [2], or Cayan [8]). Details about these fluxes are provided in the appendix. Latent and sensible fluxes were then approximated from the bulk formula:

$$Q_{La} = \rho_a L_a C_E |\mathbf{v}| (q^* - q^a) \quad (4.3)$$

$$Q_{Se} = \rho_a C_p C_H |\mathbf{v}| (T - T^a) \quad (4.4)$$

In these equations ρ_a is the air density, L_a the latent heat of evaporation of water,

C_E the transfer coefficient for latent heat, $|\mathbf{v}|$ the absolute velocity at the surface, q^* the saturation specific humidity, q^a the specific humidity of the air, C_H the transfer coefficient for sensible heat, C_p the specific heat of air at constant pressure, T the SST, and T^a the air temperature at the surface. We expect $|\mathbf{v}|$, q^* , q^a and T^a to be the parameters playing a role in the formation of the SST tripole as ρ_a , C_E and C_H are not expected to vary significantly. Equations (4.3) and (4.4) can be approximated in terms of time means and anomalies:

$$Q_{La} = \rho_a L_a C_E (|\mathbf{v}|' (\overline{q^* - q^a}) + \overline{|\mathbf{v}|} q^{*'} - \overline{|\mathbf{v}|} q^{a'}) \quad (4.5)$$

$$Q_{Se} = \rho_a C_p C_H (|\mathbf{v}|' (\overline{T - T^a}) + \overline{|\mathbf{v}|} T' - \overline{|\mathbf{v}|} T^{a'}) \quad (4.6)$$

As shown in the appendix, the dominant terms of these equations are:

$$\rho_a L_a C_E (|\mathbf{v}|' \overline{q^* - q^a}) + \frac{C_o \tau_x}{f} \frac{\partial \overline{T}}{\partial y} \quad (4.7)$$

where the first term represents the contribution of the wind through latent heat exchange, and the second the contribution of the wind through Ekman advection. This sum was regressed on the first PC of SST with a two years lag and is sketched in figure (4-2). In fact since the contribution of the wind through latent heat exchange is small compared to Ekman advection the pattern is mainly due to the latter and is thus a dipole.

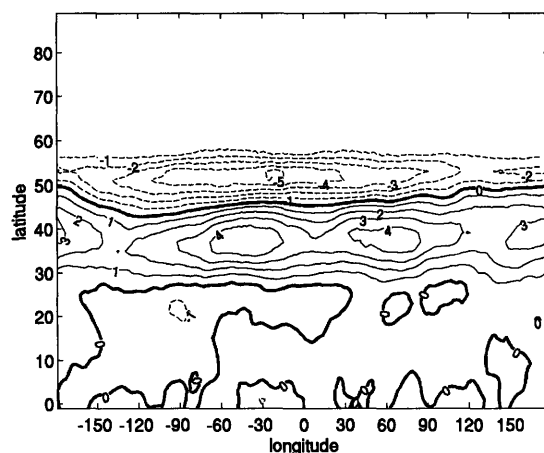


Figure 4-2: regression of $\rho_a C_o L_a |\mathbf{v}|' (\overline{q^* - q^a}) + \frac{C_o \tau_x}{f} \frac{\partial \overline{T}}{\partial y}$ onto the first PC of SST at lag 2 months in the aquaplanet. Units are W/m^2 and positive fluxes are downwards

4.2 Dipole evolution

In order to understand the evolution of the SST dipole in the aquaplanet, SST was regressed onto the PCs of the first EOF of zonal wind at different lags. The result of this computation for the aquaplanet is sketched in figure (4-3) for lags 0, -1, -2, -4, -6, and -8 years (when the ocean leads the atmosphere).

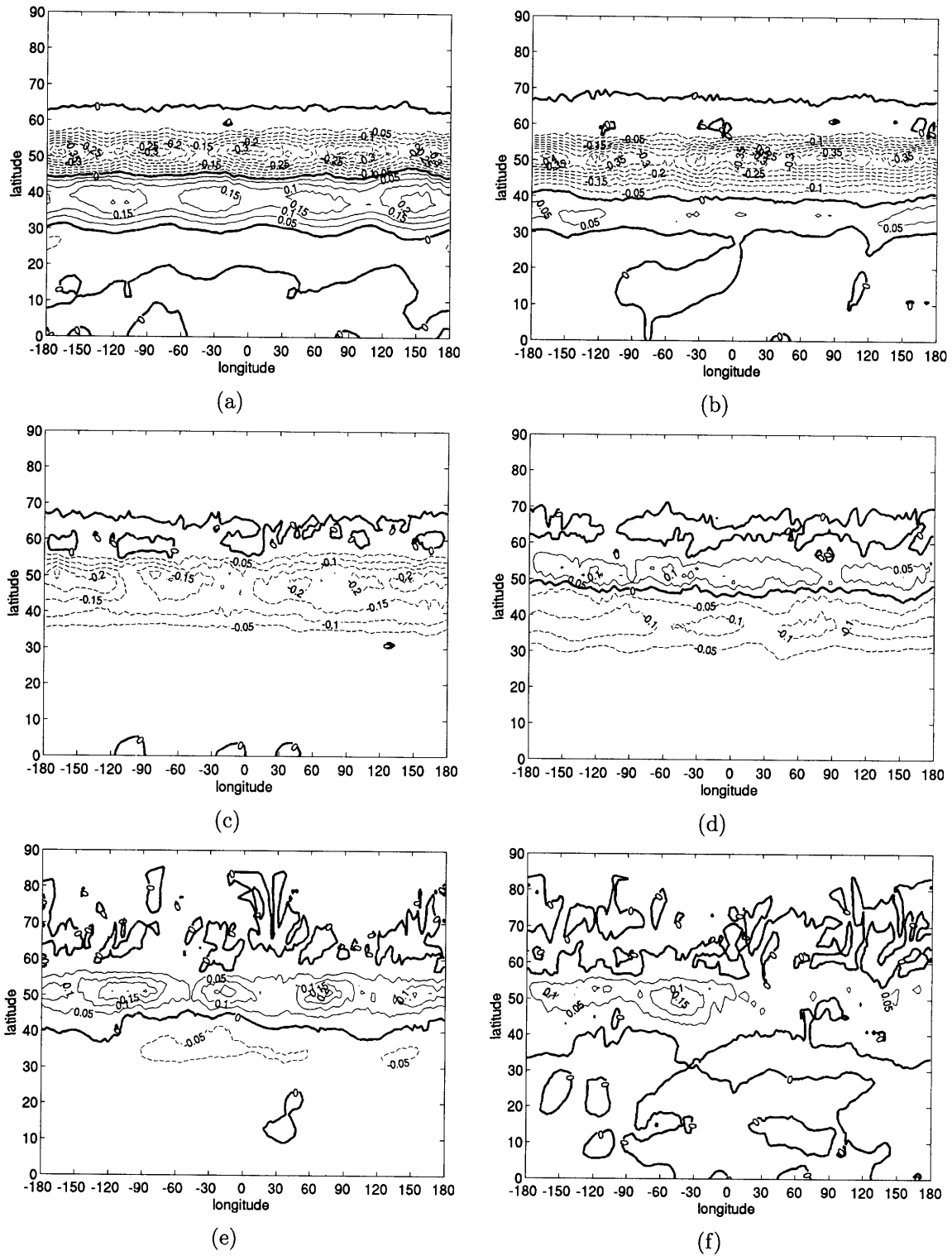


Figure 4-3: Regression of SST onto the PC of the first zonal wind EOF with lags 0, -1, -2, -4, -6, and -8 years (from (a) to (f)) in the aquaplanet. The ocean leads at negative lags

In the aquaplanet the pattern at lag 0 is very similar to the first EOF of SST, emphasizing the strong correlation between wind and SST. The dipole is slowly damped and advected southwards as time goes by. This suggests that SST anomalies are advected by mean meridional currents, which in the aquaplanet are directed southwards at mid-latitudes (see figure 2-5(b)). A comparison of the SST patterns at lag 0 and 4 (or 6) years reveals an inversion in the sign of the anomalies and a persistence of the signal, which are linked to the presence of decadal modes of variability in the aquaplanet. Indeed the auto-correlation of the first PC of SST in the aquaplanet shows negative lobes at lags of 6 years (see figure 3-5(f)).

Figure 4-4(a) shows the regression of the Ekman anomaly $\frac{C_o r'_x}{f} \frac{\partial \bar{T}}{\partial y}$ onto the first PC of SST 2 months after the formation of the SST. It is similar to the one discussed in the case of the dipole formation, but of weaker amplitude. This amplitude ranges from $+2W/m^2$ in the south to $-2W/m^2$ in the north, instead of $+3W/m^2$ and $-4W/m^2$ when the SST was lagging the atmosphere.

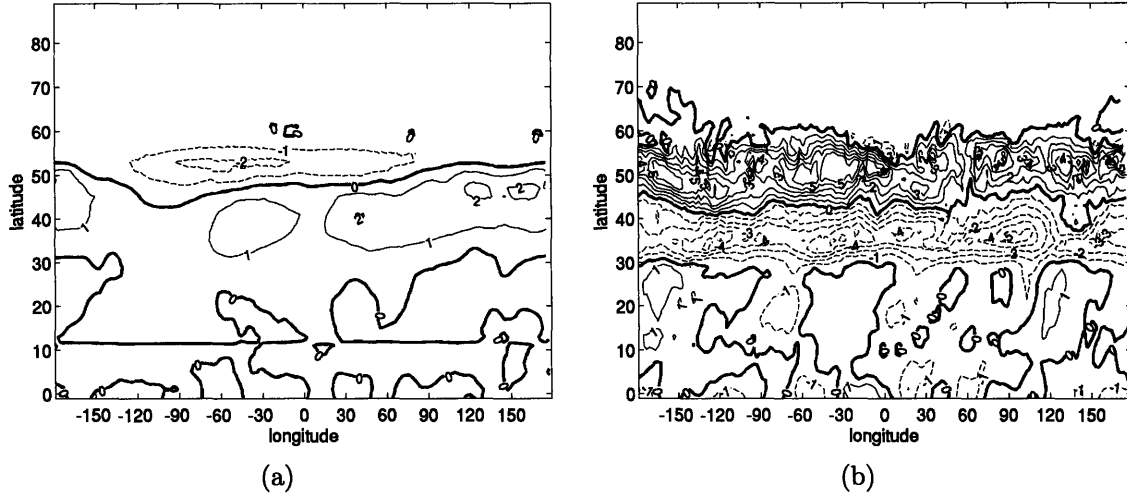


Figure 4-4: regression of (a) the Ekman anomaly $\frac{C_o r'_x}{f} \frac{\partial \bar{T}}{\partial y}$ and (b) heat fluxes onto the first PC of SST at lag -2 months in the aquaplanet. Units are W/m^2 and positive fluxes are downwards

Figure 4-4(b) shows the regression of the heat flux onto the first PC on SST at lag -2 months (two months after the SST was formed). It is very similar to the one discussed above in the case of the formation of the dipole in the aquaplanet. It is due to latent and sensible heat fluxes that were found to resemble the ones previously discussed (see figures 8-1(a) and 8-1(b) in the appendix) both in shape and amplitude. The part of sensible fluxes due to wind anomalies was found to be orders of magnitude smaller than the part due to SST and air temperature. The part of latent fluxes due to wind anomalies was found to resemble the one discussed in the case of the dipole formation but its amplitude was found to be smaller by a factor of 2.

In the aquaplanet the anomalous SST dipole is due to stochastic winds that generate temperature anomalies through Ekman transport and latent heat fluxes. Because $\rho_a L_a C_E |\mathbf{v}'| (\bar{q}^* - \bar{q}^a)$ is small in the aquaplanet and q^a follows q^* heat fluxes start damping the SST anomalies as soon as it forms. Stochastic wind anomalies are then first to decay, letting the more persistent latent fluxes damp the SST.

4.3 Simple model

4.3.1 Idealized equation for the evolution of SST anomalies

A simple model for the first EOF of SST in the aquaplanet was developed by Marshall, Ferreira, et al. [17] in the spirit of Saravanan and McWilliams [23]. From the above discussion, the first EOF of SST is believed to be advected by mean currents (as seen on figure 4-3), to be influenced by air-sea fluxes and by the wind. The air-sea flux damping might be weakened if SST feedbacks on the atmosphere. Indeed this would generate anomalous SST-induced winds, which would then feedback on the SST through Ekman transport and latent heat fluxes. We thus write our SST equation as:

$$\rho_o C_o h \frac{\partial T'}{\partial t} + \rho_o C_o h \bar{V}_{res} \frac{\partial T'}{\partial y} = Q' - \rho_o C_o h v'_{Ek} \frac{\partial \bar{T}}{\partial y} \quad (4.8)$$

In this equation overbars represent time means and primes represent anomalies. \bar{V}_{res} is the mean residual velocity advecting the SST anomalies as seen on figure (4-3), T is the SST, Q the air-sea heat flux, and subscript Ek denote the Ekman components of the velocity defined as $-\frac{\tau'_x}{\rho_o f}$. ρ_o is the water density, τ the surface wind stress, and f_o the Coriolis parameter. Following Hasselmann [19] we write the heat flux term as:

$$Q' = F_{HF} - \lambda_{HF} T' \quad (4.9)$$

where F_{HF} represents a stochastic process and λ_{HF} is the strength of the damping. Following Marshall et al. [18] We also assume that wind stress anomalies are the result of a stochastic process plus an air-sea feedback:

$$\tau'_x = F_\tau - f_\tau T' \quad (4.10)$$

where F_τ represents a stochastic process and f_τ the strength of the air-sea feedback. The Ekman transport term can be re-written using equation (4.10):

$$-\rho_o C_o h v'_{Ek} \frac{\partial \bar{T}}{\partial y} = \frac{C_o \tau'_x}{f} \frac{\partial \bar{T}}{\partial y} = -\frac{C_o f_\tau T'}{f_o} \frac{\partial \bar{T}}{\partial y} + \frac{C_o F_\tau}{f} \frac{\partial \bar{T}}{\partial y} = -\lambda_{Ek} T' + F_{Ek} \quad (4.11)$$

where λ_{Ek} is thus a function of the f_τ parameter:

$$\lambda_{Ek} = \frac{C_o f_\tau}{f} \frac{\partial \bar{T}}{\partial y} \quad (4.12)$$

This yields a new form of the SST equation (4.8):

$$\rho_o C_o h \frac{\partial T'}{\partial t} + \rho_o C_o h \bar{V}_{res} \frac{\partial T'}{\partial y} = \frac{C_o F_\tau}{f} \frac{\partial \bar{T}}{\partial y} - \lambda_{HF} T' - \lambda_{Ek} T' \quad (4.13)$$

F_τ is the part of the wind stress due to internal atmospheric dynamics, modeled as a white noise process in time but with large-scale standing pattern in space:

$$F_\tau = N(t)\sin(ky) = N(t)\sin\left(\frac{2\pi y}{L}\right) \quad (4.14)$$

where $y = 0$ corresponds to the northernmost latitude of the first EOF of SST, 60° , and $y = -L$ corresponds to the southernmost latitude of the first EOF of SST, 30° .

This model yields a frequency spectrum (see the appendix for details of the calculation):

$$\Phi(\omega) = \frac{k^2 \bar{V}_{res}^2 \delta^2 |\hat{N}|^2}{\left(k^2 \bar{V}_{res}^2 - \omega^2 + \frac{\lambda^2}{(\rho_o C_o h)^2}\right)^2 + 4\omega^2 \frac{\lambda^2}{(\rho_o C_o h)^2}} \quad (4.15)$$

where

$$\lambda = \lambda_{HF} + \lambda_{Ek} \quad (4.16)$$

represents the global damping, and $\delta = \frac{1}{\rho_o f h} \frac{\partial \bar{T}}{\partial y}$. This spectrum reaches a maximum at frequency ω_0 defined as:

$$\omega_0^2 = k^2 \bar{V}_{res}^2 - \frac{\lambda^2}{(\rho_o C_o h)^2} \quad (4.17)$$

We see that for ω_0 to exist, $k\bar{V}_{res}$ must be larger than $\frac{\lambda}{\rho_o C_o h}$; in other words the advective time scale must be larger than the damping time scale.

4.3.2 Quantitative analysis

In order to quantify λ_{HF} and λ_{Ek} , we follow Frankignoul and Hasselmann [5] and deduce from equations (4.9) and (4.10):

$$\lambda_{HF} = -\frac{\langle T^* Q \rangle}{\langle T^* T \rangle} \text{ and } f_\tau = -\frac{\langle T^* \tau_x \rangle}{\langle T^* T \rangle} \quad (4.18)$$

where $\langle A^* B \rangle$ denotes the covariance between A^* (the complex conjugate of A) and B . f_τ together with equation (4.12) then yield λ_{Ek} :

$$\lambda_{Ek} = -\frac{C_o}{f} \frac{\partial \bar{T}}{\partial y} \frac{\langle T^* \tau_x \rangle}{\langle T^* T \rangle} \quad (4.19)$$

In order to compute λ_{HF} in the aquaplanet, we use a zonally averaged version of the first EOF of SST. To each of these EOFs is associated a PC computed so that EOF patterns correspond to a signal amplitude of 1. In order to compute λ_{HF} using equation (4.18), we need to dimensionalize this time series. Following Marshall et al., we use the amplitude difference of the dipole as an index in order to do so. A time series value of +1 therefore corresponds to a dimensionalized value of 0.8°C in the case of the SST and $17\text{W}/\text{m}^2$ in the case of the heat flux. Computing equation

(4.18) then yields the curve sketched in figure 4-5(a). At negative lags, when SST leads, λ_{HF} decreases from $9W/m^2$ to $5W/m^2$ in 20 months. Figure 4-5(b) shows λ_{Ek} which is negative and drops from $-6W/m^2$ to $-4W/m^2$ in 20 months. Therefore there is a feedback from the SST towards the wind in the aquaplanet. This feedback is significant since λ_{HF} and λ_{Ek} have the same order of magnitude. In order to study further the interaction of the first EOF of SST with the atmosphere in the aquaplanet, atmosphere-only runs were integrated (see the appendix for details). They confirmed that SST anomalies were strong enough to feedback on the atmosphere in the aquaplanet. f_τ was found to be of the order of $0.01N/m^2/K$ yielding a value of λ_{HF} of the order of $-5W/m^2$, a value of the same order than the one discussed aboved.

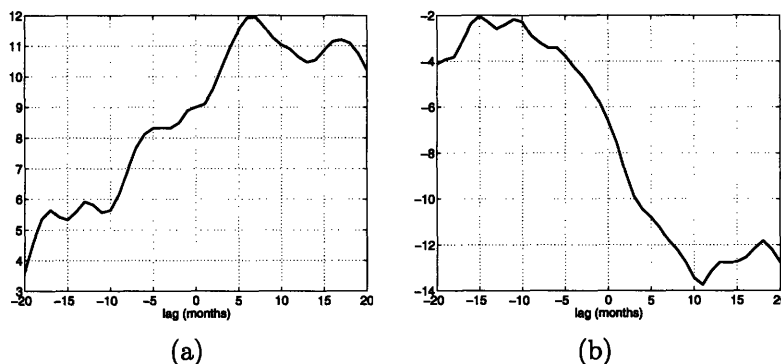


Figure 4-5: λ_{HF} (a) and λ_{Ek} (b) in the aquaplanet, in $W/m^2/K$

As in Fankignoul, Czaja et al. [4] the auto-correlation of the first PC of SST was used in order to obtain an estimation of the global damping λ defined by equation (4.16). A least squares fit of the auto-correlation function of the first PC of SST in the aquaplanet (see figure 4-6(b)) with an exponential function of the type $e^{-\frac{\lambda t}{\rho_0 C_o h}}$ yields $\lambda = 3.6W/m^2/K$ in the first months of the SST damping process if $h = 100m$. Using $L = 3300km$, $\bar{V}_{res} = 0.01m/s$, $h = 100m$, $\lambda = 3.6W/m^2/K$ in equation (4.17) shows that ω_0 exists and yields a time scale:

$$T_0 = \frac{2\pi}{\omega_0} = 12 \text{ years} \quad (4.20)$$

Note that if there were no feedback and $\lambda = \lambda_{HF} = 9W/m^2$ then there would be no peak in the spectrum of SST from equation (4.17). Figure 4-6(a) shows the power spectrum obtained from equation (4.15) superimposed to the power spectrum obtained from the aquaplanet experiment. The two curves are consistent. In particular the peak that appears in the aquaplanet is well matched by the simple model. Figure 4-6(b) shows the auto-correlation computed from equation (4.15) superimposed to the auto-correlation from the aquaplanet experiment. The two curves are again consistent. Thus equation (4.13) is believed to be a satisfactory model of the behavior of the first EOF of SST in the aquaplanet.

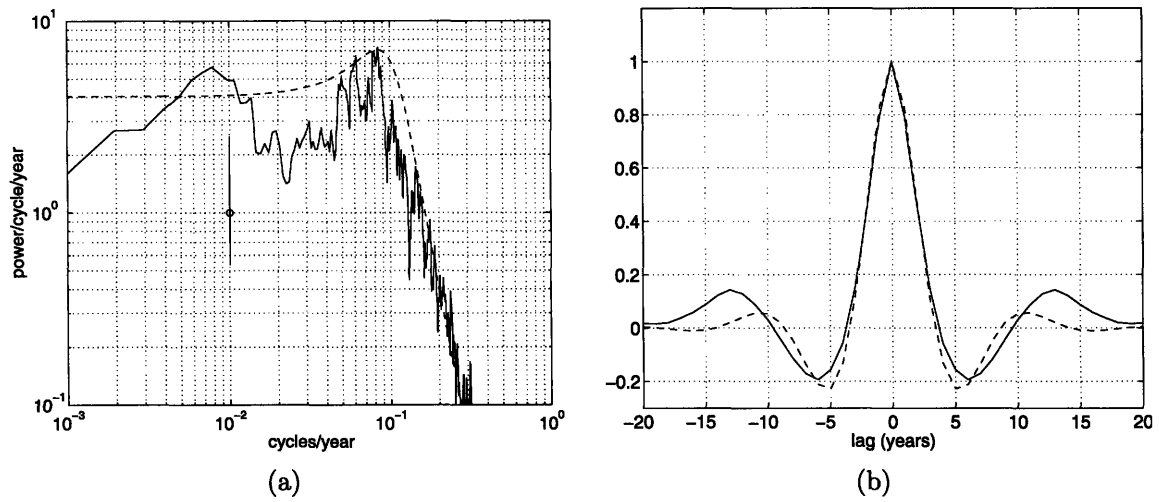


Figure 4-6: (a) Power spectrum of the first PC of SST in the aquaplanet (solid) and the corresponding theoretical spectrum (dashed) (b) Auto-correlation of the first PC of SST in the aquaplanet (solid) and the corresponding theoretical auto-correlation (dashed)

Chapter 5

Climate variability in the ridge

5.1 Decadal variability in the ridge

5.1.1 Tripole formation

In the ridge the pattern of the first EOF of SST is a tripole, as shown by figure 3-5(a). In order to understand the mechanisms that force this tripole the terms of the SST equation (5.1) were computed, as in the case of the aquaplanet.

$$\frac{\partial T'}{\partial t} + \overline{\mathbf{u}_g} \cdot \nabla T' + \mathbf{u}'_g \cdot \nabla \overline{T} = Q' - \overline{\mathbf{u}_{Ek}} \cdot \nabla T' - \mathbf{u}'_{Ek} \cdot \nabla \overline{T} \quad (5.1)$$

As in the case of the aquaplanet two terms were found to be significantly larger than the others: the Ekman forcing $\frac{C_o \tau'_x}{f} \frac{\partial \overline{T}}{\partial y}$ and the air-sea heat flux Q' . The others were orders of magnitude smaller. In particular advection by (strong) gyres as well as Ekman pumping were found to be negligible.

Figure 5-1(a) shows the Ekman forcing term $\frac{C_o \tau'_x}{f} \frac{\partial \overline{T}}{\partial y}$. It consists in an antisymmetric dipole centered on the line of 39° of latitude and extending from 20° to 60° of latitude. This dipole is positive to the south and negative to the north, reaching values of $\pm 5W/m^2$. A dipole was expected from the pattern of the first EOF of wind stress anomaly (figure 3-1(c)). This wind pattern is stronger above the line of 39° of latitude while the temperature gradient is weaker above this line. This results in a fairly antisymmetric anomalous Ekman dipole along the line of 39° of latitude. The anomalous wind stress pattern exhibits eastward winds to the north and westward winds to the south which result (in the northern hemisphere) in a southwards Ekman transport to the north and a northwards transport to the south. This induces a negative Ekman anomaly to the north and a positive anomaly to the south, in accordance with the pattern of figure 5-1(a).

The heat flux term is sketched in figure 5-1(b), where positive fluxes were chosen to indicate a flux from the atmosphere towards the ocean. From 10° to 35° of latitude air-sea fluxes are directed from the ocean to the atmosphere and reach an extremum of $-6W/m^2$. From 35° to 60° of latitude fluxes are mainly directed from the atmosphere to the ocean and reach extremum values of more than $10W/m^2$ at the basin boundaries. Air-sea fluxes are thus found to be driving the pattern of the first EOF of

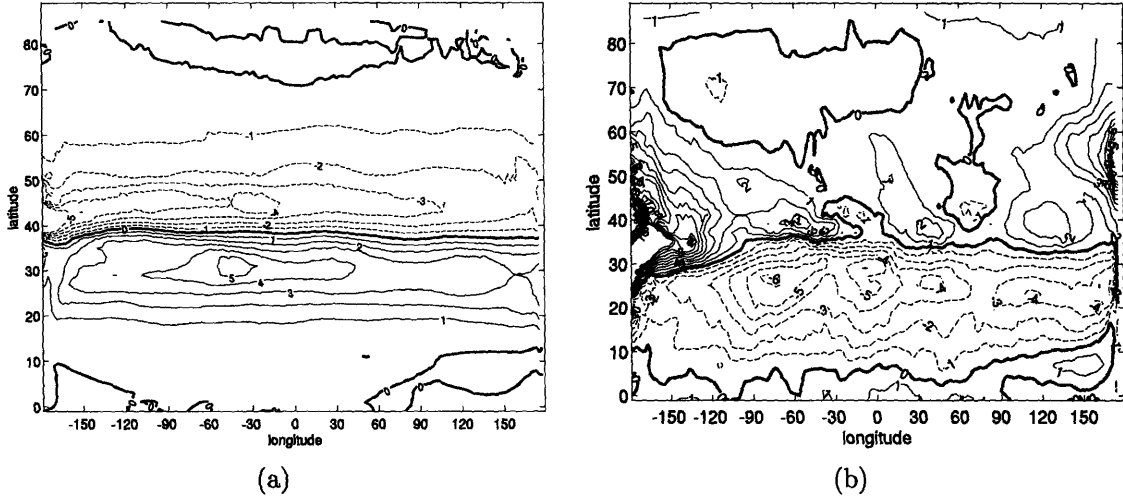


Figure 5-1: (a) regression of the Ekman anomaly $\frac{C_o \tau'_x}{f} \frac{\partial \bar{T}}{\partial y}$ onto the first PC of SST at lag 2 months (two months before the SST pattern materializes) in the ridge. Units are W/m^2 . (b) regression of the heat flux onto the first PC on SST at lag 2 months in the ridge. Values above $10W/m^2$ were discarded for readability. Units are W/m^2 . Positive fluxes are downwards

SST together with the Ekman transport. This is different from the aquaplanet case where we found that the Ekman transport was also driving the SST but the air-sea heat flux was damping it.

As in the aquaplanet case the heat flux was split into latent, sensible, longwave, and shortwave fluxes. Latent and sensible heat fluxes were also found to be the main components of the air-sea heat flux in this case, as developed at length in the appendix. As before these fluxes were then approximated from the bulk formula, before being approximated as time means and anomalies. The atmospheric anomalies that lead the SST were found to be:

$$\rho_a L_a C_E (|\mathbf{v}'| (\overline{q^*} - q^a) - \overline{|\mathbf{v}|} q^{a'}) + \frac{C_o \tau'_x}{f} \frac{\partial \bar{T}}{\partial y} \quad (5.2)$$

The first term represents the action of the wind through latent heat exchange, the second term the action of the specific humidity of the air through latent heat exchange, and the third term the action of the wind through Ekman advection. This sum was regressed onto the first PC of SST with a lag of two months, and is sketched in figure (5-2). It results in a tripole centered on the line of 30° of latitude, reaching extremum values of -10 , 8 and $-5W/m^2$ in the interior from north to south, and values of $10W/m^2$ at the boundaries. This pattern seems closely related to the pattern of the first EOF of SST in the ridge (figure 3-5(a)). Therefore the first EOF of SST in the ridge is induced by atmospheric variability with the three terms of equation (5.2) playing the leading role. The main difference with the aquaplanet is the contribution of the specific humidity of the air in this equation, as well as the more significant contribution of the wind through latent heat exchange, which leads to a tripole in this case, instead of the Ekman drive dipole in the aquaplanet.

The amplitude of the SST forcing in the ridge is thus stronger than in the aqua-

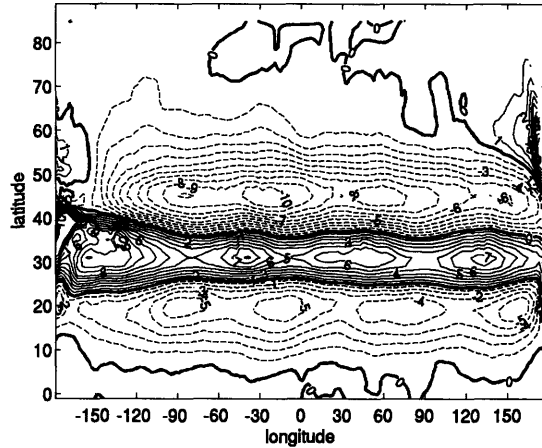


Figure 5-2: regression of $\rho_a C_o L_a (|v|'(\overline{q^* - q^a}) - \overline{|v|q^{a'}}) + \frac{C_o \tau_x'}{f} \frac{\partial \overline{T}}{\partial y}$ onto the first PC of SST at lag 2 months (two months before the SST pattern materializes) in the ridge. Units are W/m^2 and positive fluxes are downwards

planet, where it was found to reach maximum values of $10W/m^2$. However the first EOF of SST in the aquaplanet was found to be of stronger amplitude than the first EOF of SST in the ridge by a factor of two. A correlation of the first PC of the wind with the first PC of the SST in the two configurations is sketched in figure (5-3). Zonal wind stress and SST are well correlated in the ridge, but only for a period of five to ten months. Zonal wind stress and SST are less correlated in the aquaplanet, but the correlation remains constant for a longer period of time. In the aquaplanet the patterns of the first EOFs of SST and zonal wind stress share similar spatial features: both are zonal and act over the same range of latitudes and can be mutually reinforcing. When the zonal wind anomaly moves it keeps on forcing the SST pattern over a wide range of latitudes. This cannot happen in the ridge, where SST and zonal wind stress patterns are very different. Thus in the aquaplanet the SST forcing might be maintained for a longer time than in the ridge, resulting in a stronger anomaly.

5.1.2 Tripole evolution

In order to understand the evolution of the SST after it has been formed, SST was regressed onto the PCs of the first EOF of zonal wind at different lags. The result of this computation for the ridge is shown in figure (5-4) for lags 0, -1, -2, -4, -6, and -8 years (when the ocean leads the atmosphere).

The pattern at lag 0 is very similar to the first EOF of SST, emphasizing the strong correlation between wind and SST. The tripole then seems to fade away as time goes by, leaving a pattern that resembles that of the second EOF of SST at longer time scales. In order to understand this damping mechanism a term by term analysis of the SST equation was carried out. As in the case of the formation of the SST tripole the two dominant terms were found to be the Ekman anomaly $\frac{C_o \tau_x'}{f} \frac{\partial \overline{T}}{\partial y}$ and the heat flux anomaly Q' .

The Ekman anomaly was regressed on the first EOF of SST at lag -2. It is sketched

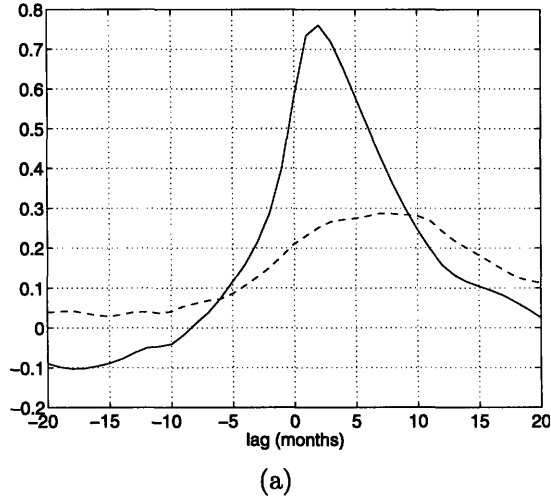


Figure 5-3: (a) cross-correlation of the first PC of SST with the first PC of zonal wind stress τ_x , in the aquaplanet (dashed) and in the ridge (solid). A positive lag indicates that the atmosphere leads the ocean

in figure 5-5(a). It has the same characteristics as the one discussed in the case of the SST formation. In particular it still forces the SST but its amplitude is weaker: it reaches extrema of $2W/m^2$ in the south and $-1W/m^2$ in the north against $5W/m^2$ and $-4W/m^2$ previously.

Figure 5-5(b) shows the regression of the heat flux term Q' onto the first PC of SST at lag -2 . It is a tripole centered on the line of 30° of latitude which reaches extremum values of $\pm 4W/m^2$ and which contributes to the damping of the SST tripole. This damping flux was found to be mainly due to latent fluxes. As in the case of the formation of the tripole, latent fluxes were split into fluxes due to anomalies in wind, fluxes due to saturation specific humidity, and fluxes due to the specific humidity of the air. The sum of the fluxes due to anomalies in saturation specific humidity and specific humidity of the air was found to be a tripole contributing to a damping of the SST tripole, as shown in figure 5-6(a). Therefore in the ridge damping always occurs as soon as the SST is formed. However this damping is initially dominated by wind anomalies that force the SST. Since these wind anomalies are stochastic they decay rapidly leaving the more persistent latent fluxes to damp SST.

5.1.3 Simple model

Idealized equation for the evolution of SST anomalies

From the above discussion the first EOF of SST is believed to be influenced by air-sea fluxes and by the wind. The air-sea flux damping might be weakened if SST feeds back on the atmosphere. Indeed this would generate anomalous SST-induced winds, which would then feedback on the SST through Ekman transport and latent heat fluxes. The difference with the aquaplanet case is the absence of advection. We thus write our SST equation as:

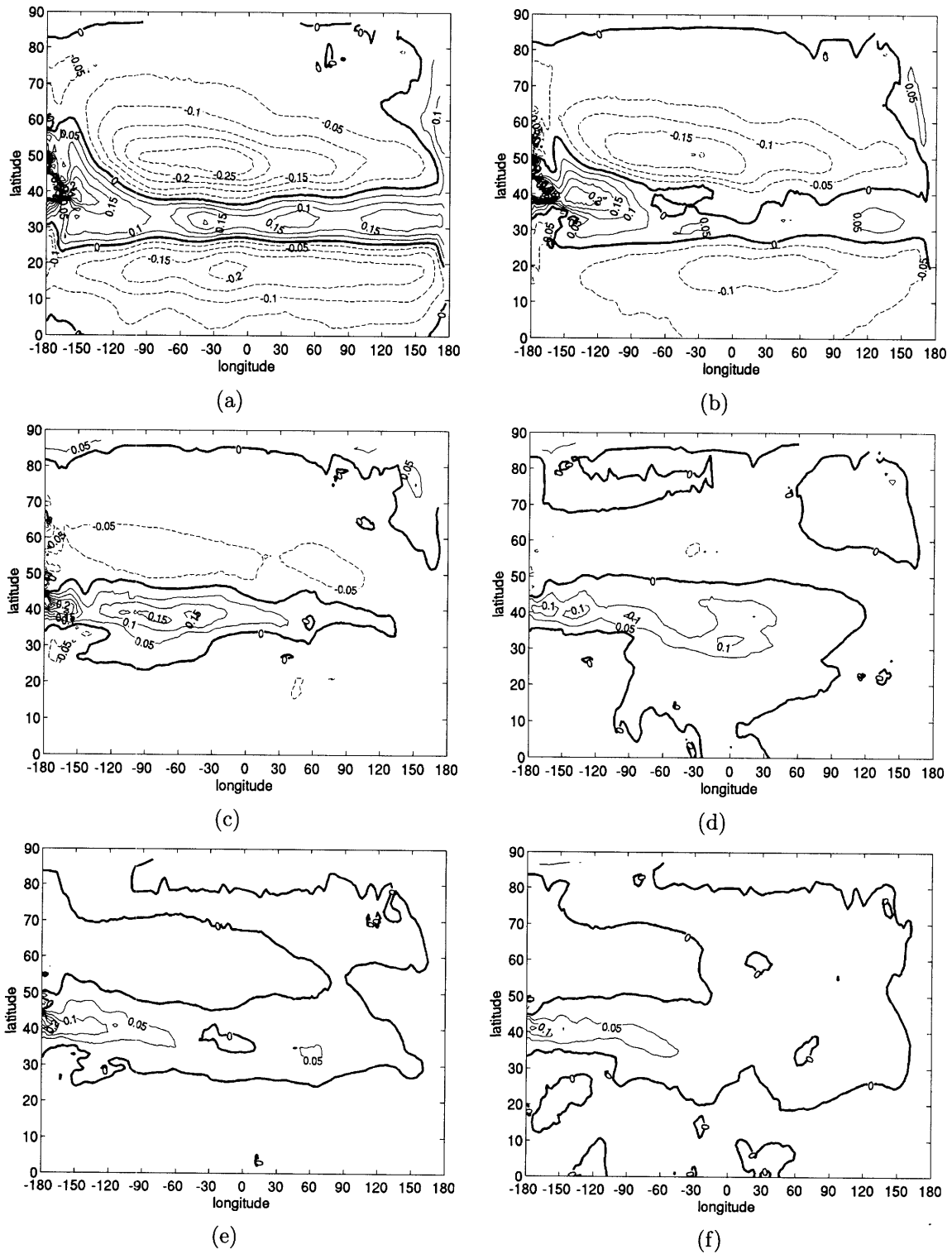


Figure 5-4: Regression of SST onto the PC of the first zonal wind EOF with lags 0, -1, -2, -4, -6, and -8 years (from (a) to (f)) in the ridge. The ocean leads at negative lags

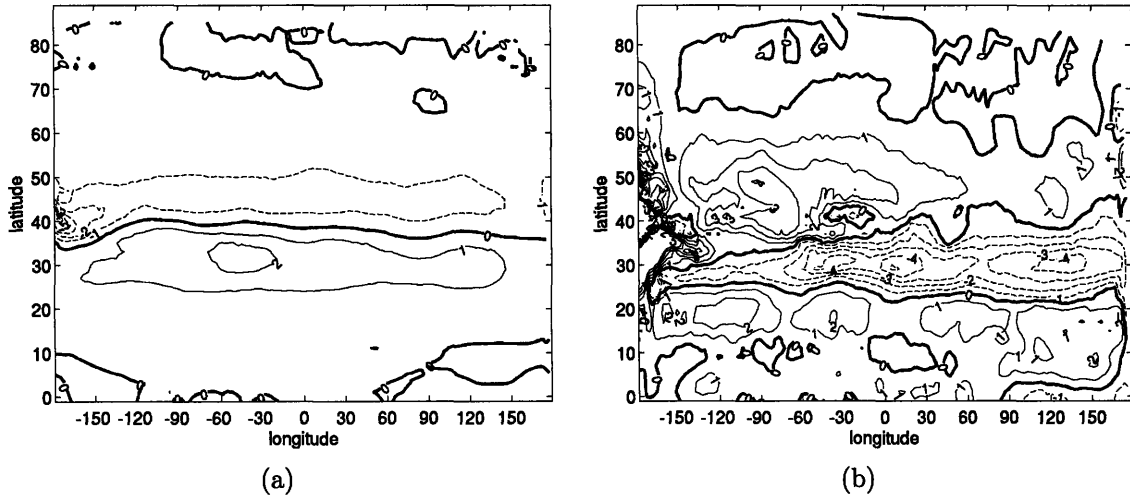


Figure 5-5: regression of (a) the Ekman anomaly $\frac{C_o r'_x}{f} \frac{\partial T}{\partial y}$ and (b) heat fluxes onto the first PC on SST at lag -2 months. Units are W/m^2 and positive fluxes are downwards

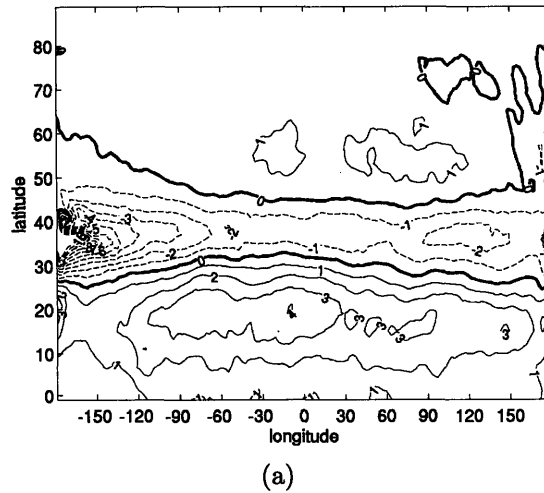


Figure 5-6: regression of (a) $\rho_a C_o L_a |v|'(\overline{q^* - q^a})$, (b) $\rho_a C_o L_a |v|(\overline{q^{*'} - q^{a'}})$ onto the first PC of SST at lag -2 months (two months after the SST pattern has materialized). Units are W/m^2 and positive fluxes are downwards

$$\rho_o C_o h \frac{\partial T'}{\partial t} = \frac{C_o F_\tau}{f} \frac{\partial \bar{T}}{\partial y} - \lambda_{HF} T' - \lambda_{Ek} T' \quad (5.3)$$

In this equation λ_{HF} and λ_{Ek} are the damping terms due to air-sea heat fluxes and the feedback term due to Ekman transport. This air-sea feedback was written as expressed in equation (4.11). This equation can also be written:

$$\rho_o C_o h \frac{\partial T'}{\partial t} = F - \lambda T' \text{ with } \lambda = \lambda_{HF} + \lambda_{Ek} \quad (5.4)$$

where F represents a stochastic forcing and λ represents the global damping due to damping by air-sea heat fluxes and feedback through Ekman transport.

Quantitative analysis

λ_{HF} and λ_{Ek} were first computed from equations (4.18) and (4.19), as in the case of the aquaplanet. Figure 5-7(a) shows that at negative lags, when SST leads, the damping term λ_{HF} is approximately $9W/m^2/K$ in the first months. Note that at positive lags it is another EOF that characterizes the heat flux; therefore values of λ_{HF} at positive lags are not given by figure 5-7(a).

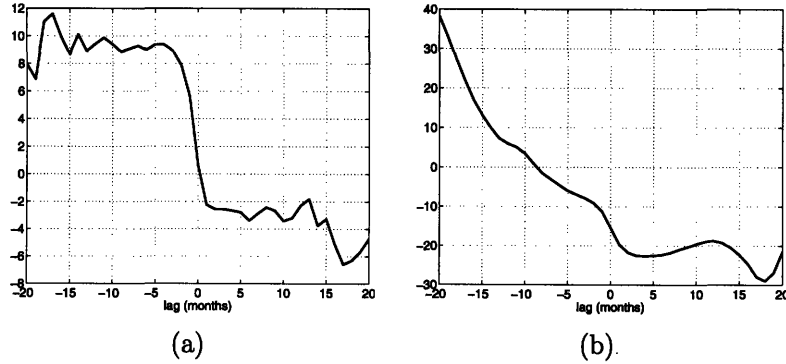


Figure 5-7: λ_{HF} (a) and λ_{Ek} (b) in the ridge, in $W/m^2/K$

Figure 5-7(b) shows λ_{Ek} which was computed in the same way as λ_{HF} . At negative lags, when SST leads, the value of λ_{Ek} increases from $-20W/m^2/K$ to $40W/m^2/K$ in twenty months. However this computation is thought to have little meaning as wind and SST are not correlated enough in this case. In particular small values of the PC of SST induce high values of λ_{Ek} . Atmosphere-only calculations were thus used in order to quantify the interaction of the SST with the atmosphere (see the appendix for more details). It was shown that f_τ was small, of the order of $0.005N/m^2/K$. These atmosphere-only calculations also showed that the reason for a feedback in the aquaplanet but none in the ridge is an EOF of stronger amplitude in the aquaplanet. In the ridge the amplitude of the SST pattern is likely to be weak enough to prevents any significant air-sea feedback to occur. Our simple model in the case of the first EOF of SST in the ridge is thus equation (5.3) where λ_{Ek} is zero, thus:

$$\rho_o C_o h \frac{\partial T'}{\partial t} = F_{HF} - \lambda_{HF} T' \quad (5.5)$$

and $\lambda_{HF} = 9W/m^2/K$. This expression was previously proposed by Hasselmann [19]. The corresponding power spectrum as a function of frequency is thus the classical result of Hasselmann:

$$\Phi(\omega) = \frac{|\hat{F}|^2}{\frac{\lambda_{HF}^2}{(\rho_o C_o h)^2} + \omega^2} \quad (5.6)$$

Figure 5-8(a) shows this theoretical spectrum superimposed to the spectrum obtained from the ridge experiment. The two curves are consistent. The corresponding auto-correlation as a function of lag t is given by:

$$\alpha(t) = e^{-\frac{\lambda_{HF}|t|}{\rho_o C_o h}} \quad (5.7)$$

Figure 5-8(b) shows the auto-correlation obtained from the ridge experiment superimposed to the curve defined by equation (5.7) where h was chosen to be 100m. The two curves match perfectly at lags smaller than 5 years, and less at larger lags. Values of the auto-correlation at large lags are not significant and can therefore be assumed to be due to noise. It is however likely that the first EOF of SST captures a low-frequency signal at the western boundary, where the high-frequency triple is superimposed to the low-frequency pattern captured by the second EOF of SST. Thus equation (5.5) is thought to be a satisfactory model of the first EOF of SST in the ridge. In particular no advection by mean gyres nor any air-sea feedback are needed in order to explain the behavior of the first EOF of SST in the ridge.

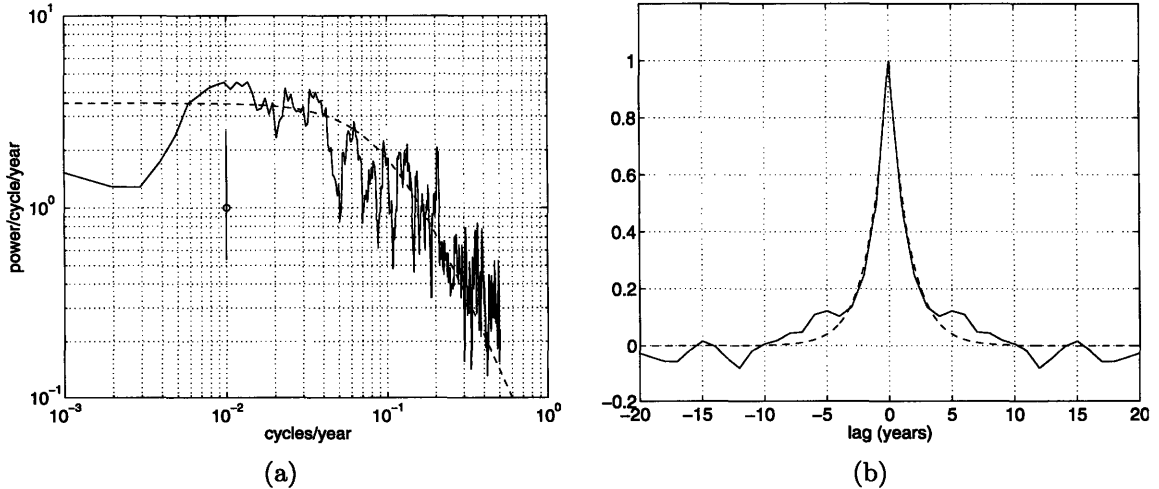


Figure 5-8: (a) Power spectrum of the first PC of SST in the ridge (solid) and the corresponding theoretical spectrum (dashed) (b) Auto-correlation of the first PC of SST in the ridge (solid) and the corresponding theoretical auto-correlation (dashed)

As in the aquaplanet a least squares fit of the auto-correlation function of figure 5-8(b) with an exponential function of the type $e^{-\frac{\lambda t}{\rho_o C_o h}}$ yields $\lambda = 8.5W/m^2/K$ in

the first years of the SST damping process if h is $100m$. Since we found $\lambda \approx \lambda_{HF} \approx 9W/m^2/K$ we deduce $\lambda_{Ek} \approx 0$ from the definition of λ . This confirms the absence of any air-sea feedback in the ridge assuming that our choice of h is accurate. Because the SST anomaly is weak compared to the one in the aquaplanet and does not benefit from any feedback, it is therefore quickly damped in the ridge case.

5.2 Centennial variability in the ridge

The auto-correlation of the first PC of baroclinic pressure and the autocorrelation of the second PC of SST in the ridge, which are sketched in figure 5-9(a), show a 120 years oscillation and covary in time. Thus slow baroclinic waves and the second EOF of SST have to be related in some way. To investigate further SST was regressed onto the PCs of the second EOF of SST at different lags. The result of this computation is shown in figure (5-10) for lags 6, 66, 121, 173, 228, and 294 years. A pattern similar to the one of the second EOF of SST is observed at each lag. Every 60 years the pattern changes sign, confirming the 120 years oscillation period detected in the auto-correlations of the PCs of baroclinic pressure and SST.

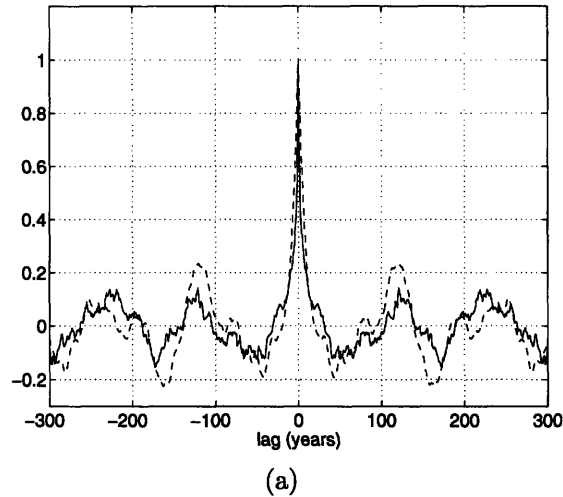


Figure 5-9: auto-correlation of the first PC of baroclinic pressure (dashed) and autocorrelation of the second PC of SST in the ridge (solid)

As previously discussed (see section 3.2.2) Zorita and Frankignoul [9] considered the equation proposed by White [26] in order to explain the behavior of the baroclinic streamfunction. Their model yields a solution which consists of the sum of a forced wave and a travelling wave (see the appendix for details of the calculation):

$$\Psi = \frac{F_o}{\omega} \sin(\omega t) + \frac{F_o}{\omega} \sin\left(\frac{\omega x}{c_r} - \omega t\right) \quad (5.8)$$

where F_o is the expected amplitude of the forcing. This solution yields a power spectrum with a high-frequency slope in -2 (see equation 3.3). A high-frequency slope in -2 is indeed observed when computing the power spectrum of the first PC

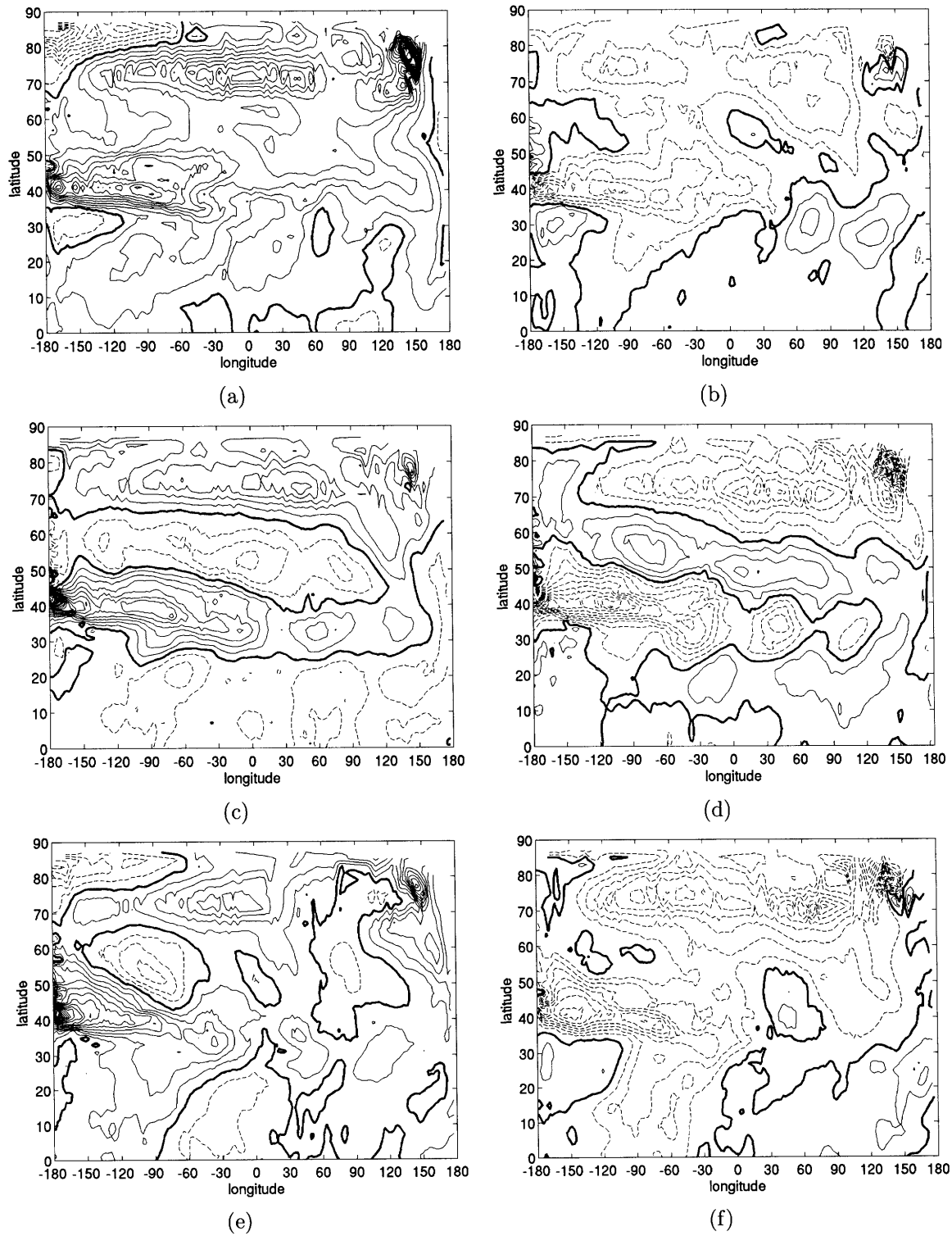


Figure 5-10: Regression of SST onto the PC of the first zonal wind EOF with lags 6, 66, 121, 173, 228, and 294 years (from (a) to (f)) in the ridge. Contour intervals are $0.01^{\circ}C$.

of baroclinic pressure (see figure 3-4(b)). However we expect the Frankignoul and Zorita model to generate a triangular auto-correlation (see equation (3.4)) reaching 0 at lag $\frac{x}{c_r}$. The shape of this auto-correlation is reminiscent of the exponential autocorrelation predicted by Hasselmann and Frankignoul [5] in the case of a SST forced by stochastic processes and damped by air-sea fluxes (see equation (5.7)). In the case of the Hasselmann model there is no preferred time scale as SST slowly adjusts at an exponential rate. However, in the case of the baroclinic streamfunction, the disturbance forced at location x by the forced wave of equation (5.8) is adjusted after the travelling wave of equation (5.8) has reached this location. Thus at location x , after a time $\frac{x}{c_r}$, the system is adjusted and has no memory of previous evolutions. A 0 auto-correlation is thus expected at lags larger than $\frac{x}{c_r}$ at location x .

The cross-correlation of the second PC of SST with the first PC of zonal wind is sketched in figure 5-11(a) together with the cross-correlation of the second PC of SST with the first PC of baroclinic pressure. The two curves show the same period of oscillation of 120 years. Thus the second EOF of SST, baroclinic pressure, and wind are closely related, and more importantly the atmosphere knows about the centennial oscillation which implies the existence of an air-sea feedback in this case.

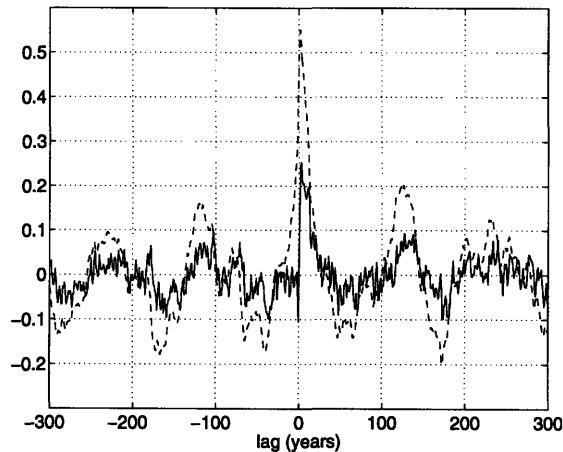


Figure 5-11: cross-correlation of the second PC of SST with the first PC of baroclinic pressure (dashed) and the first PC of zonal wind (solid). the SST leads at negative lags

In order to visualize the evolution of zonal wind stress anomalies and baroclinic streamfunction anomalies with time these two fields were regressed onto the PC of the second EOF of SST at different lags. The baroclinic streamfunction described by equation (5.8) consists in a forced wave and a travelling wave. The first EOF of the baroclinic streamfunction covaries with the wind and seems to capture the forced local response of the ocean to the wind. In order to visualize the travelling waves a third field consisting of the baroclinic streamfunction minus its first EOF was thus regressed onto the PC of the second EOF of SST at different lags. These regressions at lags -1, 3, 9, 33, and 66 years are sketched in figures (5-12) and (5-13).

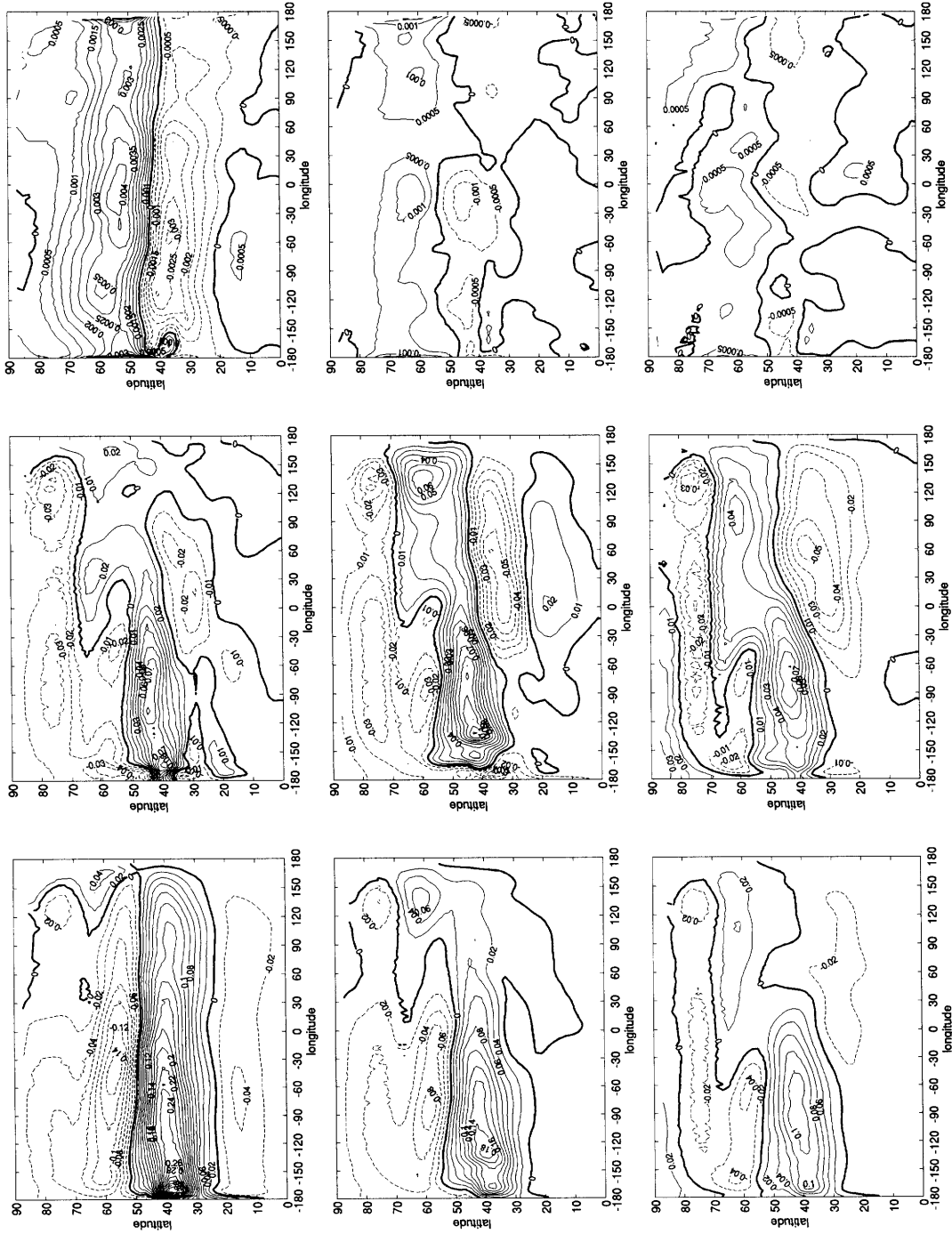


Figure 5-12: Regression of the baroclinic streamfunction (left column), the baroclinic streamfunction minus its first EOF (middle column) and the surface wind stress (right column) onto the second PC of SST at lags -1, 3, and 9 years (from top to bottom)

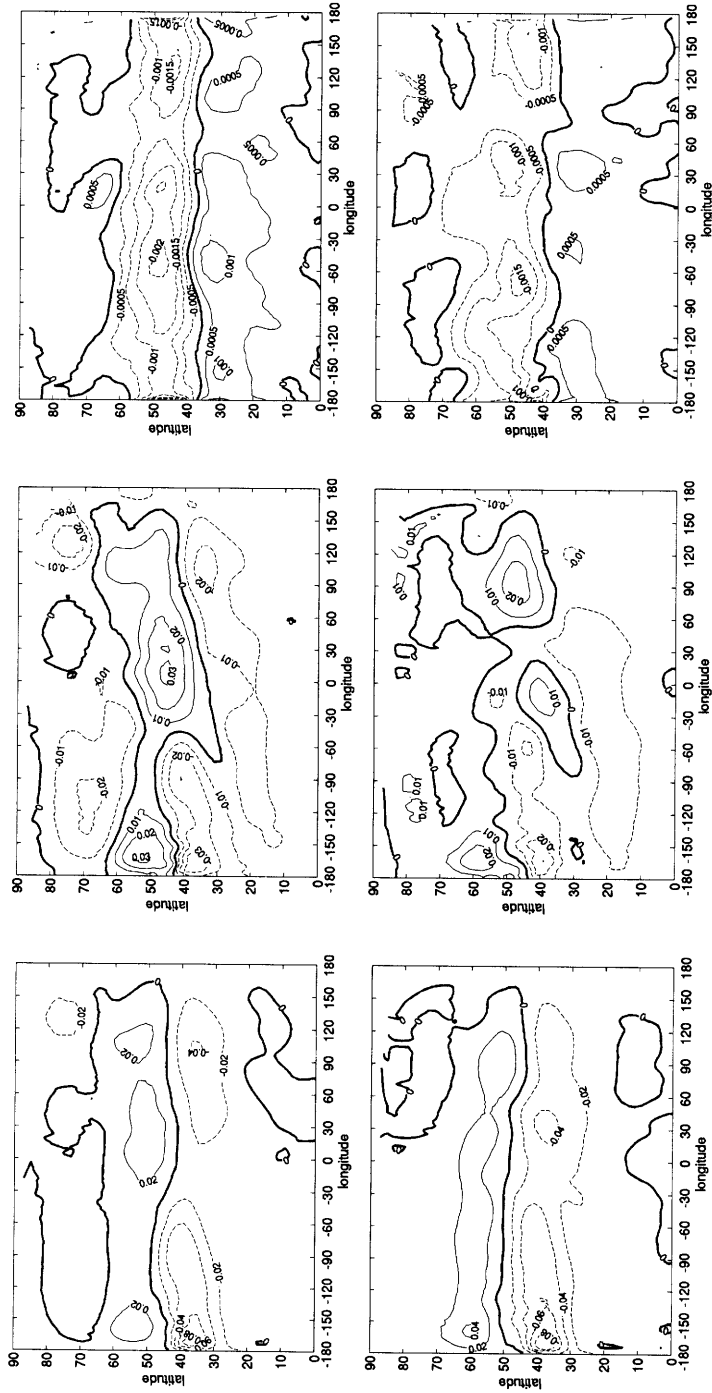


Figure 5-13: Regression of the baroclinic streamfunction (left column), the baroclinic streamfunction minus its first EOF (middle column) and the surface wind stress (right column) onto the second PC of SST at lags 33 and 66 years (from top to bottom)

At lag -1 year the zonal wind stress anomaly is a dipole positive in the north and negative in the south centered on the line of 40° of latitude. It coincides with a system of two baroclinic gyres that straddle the mean gyres of the ridge and which are the inter-gyre gyres of Marshall et al. [18]. At lag 3 years the anomalous zonal wind stress dipole is fading away, its amplitude being four times less than at lag -1 year. Simultaneously the northern inter-gyre gyre is being advected by the anticyclonic polar gyre. The pattern of the baroclinic streamfunction minus its first EOF shows that waves were generated at the eastern boundary: a positive anomaly is observed on the line of 60° of latitude, and a negative anomaly is observed on the line of 30° of latitude. At lag 9 years these waves are observed slightly more west. A westward propagation or advection must thus have taken place. At the same time the southern inter-gyre gyre is slowly being advected northwards. At lag 33 years propagating waves and advected inter-gyre gyres induce a more zonal pattern which resembles a dipole centered between the lines of 40° and 50° of latitude. This pattern coincides with a stronger zonal wind stress anomaly the amplitude of which is now half what it was at lag -1 . This zonal wind stress anomaly is a dipole which is centered on the line of 40° of latitude as the original dipole detected at lag -1 , but is of opposite sign. At lag 60 years the travelling waves reach the western boundary and the patterns of the three fields considered here resemble the patterns at lag -1 , with weaker amplitudes and opposite signs.

A possible mechanism explaining this sequence of events could thus be as follows: the wind forces locally a system of intergyre-gyres and triggers anomalous waves at the eastern boundary. The intergyre-gyre is then advected by mean currents, while anomalous Rossby waves propagate westwards. As the travelling waves reach the western boundary they generate an anomalous SST. This anomalous SST generates an inverted zonal wind stress dipole through an air-sea feedback. This inverted dipole forces an inverted system of intergyre-gyres and induces anomalous waves at the western boundary. The processus just described can repeat and yield to oscillations.

5.2.1 Idealized model of centennial variability

Marshall et al. [18] proposed a model for the mechanism suggested above, albeit without advection, which is expected to substantially affect Rossby wave speeds here. We thus consider one-dimensional linearized quasigeostrophic potential vorticity equation in a zonal current:

$$\frac{\partial \Psi'_c}{\partial t} + (\bar{U}_g - \beta L_\rho^2) \frac{\partial \Psi'_c}{\partial x} = -\frac{1}{\rho_o h} \frac{\partial \tau'_x}{\partial y} \quad (5.9)$$

where Ψ'_c is the anomalous baroclinic streamfunction in the upper layer of a two-layer ocean, \bar{U}_g is the zonal mean flow velocity, β is the meridional gradient of the Coriolis parameter, L_ρ is the oceanic deformation radius, ρ_o is the density of water, h is the height of the mean thickness of the upper layer, and τ'_x is the anomalous surface zonal wind stress. Wind anomalies are assumed to be the sum of an internal variability modelled as a white noise and a linear function of the SST anomalies T' :

$$\tau'_x = F_\tau - f_\tau T' \quad (5.10)$$

where F_τ represents a stochastic process, and f_τ is the strength of the air-sea feedback.

Marshall et al. [18] modelled the modulation of temperature differences across the mean position of the atmospheric jet stream yielding to the equation for the SST:

$$\rho_o h C_o \frac{\partial T'}{\partial t} = m \Psi'_m + g \Psi'_{c|w} - \lambda T' + F \quad (5.11)$$

where $m \Psi'_m$ represents the anomaly of heat transport by the MOC, $\Psi'_{c|w}$ represents the value of the anomalous baroclinic streamfunction at the western boundary, g is a measure of the efficiency of heat transport by the baroclinic streamfunction, λ represents damping and F_T is a stochastic forcing term. In the following we assume that it is baroclinic waves that are responsible for the dynamics of the system, and therefore neglect the influence of the MOC. Thus $m \Psi'_m = 0$. In the limit discussed by Bjerknes, [14] heat storage is neglected ($\frac{\partial T'}{\partial t} = 0$), and atmospheric heat transport anomalies exactly balance oceanic heat transport anomalies:

$$\lambda T' = g \Psi'_{c|w} \quad (5.12)$$

Equations (5.9), (5.10), and (5.12) yield (see the appendix):

$$\hat{\Psi}_c = \frac{\hat{F} \left(1 - e^{\frac{i\omega x}{\bar{U}_g - \beta L_\rho^2}} \right)}{-i\omega + \frac{g f_\tau}{\lambda} \left(1 - e^{-\frac{i\omega L}{\bar{U}_g - \beta L_\rho^2}} \right)} \quad (5.13)$$

where L is the width of the basin, and c_r , the effective Rossby wave velocity, is defined as:

$$c_r = \bar{U}_g - \beta L_\rho^2 \quad (5.14)$$

5.2.2 Quantitative analysis

In order to estimate equation (5.13) it is necessary to evaluate the values of $\bar{U}_g - \beta L_\rho^2$, g , λ , and f_τ . L_ρ^2 is computed from:

$$\begin{cases} L_\rho^2 = \frac{g' h}{f^2} \\ g' = g \frac{\rho_2 - \rho_1}{\rho_2} \end{cases} \quad (5.15)$$

where indices $i = 1$ and 2 represent respectively the upper and lower layers, g' is the reduced gravity, ρ_i the mean density of each layer. At 40° of latitude (where most of the SST signal lies), h was found to be $800m$ by inspection of the depth of the thermocline. ρ_i was computed in each layer by averaging the density in each layer. L_ρ was found to be of the order of 37 km. At 40° of latitude $\bar{U}_g = 0.015m/s$, so c_r

must be of the order of 0.01m/s. In particular c_r can be 0.008m/s which corresponds to 60 years for a Rossby wave to cross the basin.

Since we believe that the intergyre-gyre generates the second EOF of SST we can estimate $\frac{g}{\lambda}$ from:

$$\frac{g}{\lambda} = \frac{\langle \Psi_{c|w}^* T \rangle}{\langle \Psi_{c|w}^* \Psi_{c|w} \rangle} \quad (5.16)$$

This yields $\frac{g}{\lambda} = 10^{-7} K.s.m^{-3}$. An atmosphere-only calculation was carried out in order to estimate the strength of the air-sea feedback (see the appendix for details). This computation yielded a value of f_r of the order of $0.02 N/m^2/K$. We thus get $\frac{gf_r}{\lambda} = 2.10^{-9} s^{-1}$. The power spectrum and autocorrelation obtained with this value was superimposed to the ones obtained from the ridge experiment and are sketched in figures 5-14(a) and 5-14(b). Although our model is a very crude approximation of the reality the theoretical power spectrum obtained from equation (5.13) predicts reasonably well the one obtained from the first PC of the baroclinic streamfunction. In particular no major peak is observed, and a -2 high-frequency slope is found. The theoretical auto-correlation shows a peak at lag 0 that reaches 1 at decadal timescales and centennial oscillations, as in the autocorrelation obtained from the first PC of the baroclinic streamfunction.

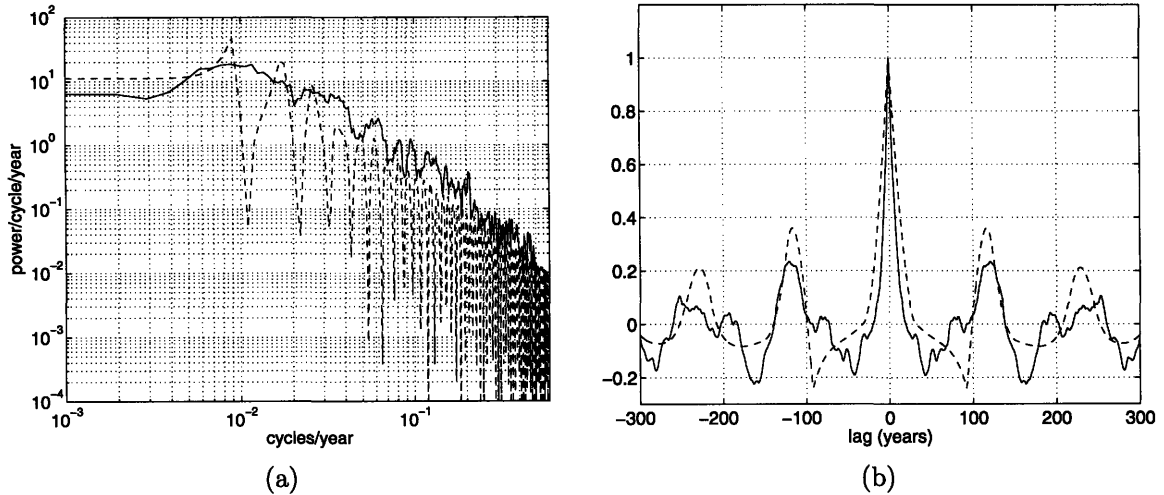


Figure 5-14: (a) Power spectrum of the first PC of baroclinic pressure (solid) and the theoretical power spectrum (dashed). (b) Auto-correlation of the first PC of baroclinic pressure (solid) and the theoretical auto-correlation (dashed).

Considering equation (5.13) we see that the period of oscillation depends on the value of $(\bar{U}_g - \beta L_\rho^2)$, and the existence of an oscillation depends on the value of $\frac{gf_r}{\lambda}$. We look for oscillations by looking for minima of the denominator of equation (5.13). Because an analytical expression of these minima could not be derived, equation (5.13) was plotted for various values of $\frac{gf_r}{\lambda}$. It was found that for oscillations to occur $\frac{gf_r}{\lambda}$ should be at least 7.10^{-10} , keeping all other parameters constant. Figure 5-15(b) shows the theoretical autocorrelation of the baroclinic streamfunction computed using

values of $\frac{gf_r}{\lambda}$ equal to 10^{-10} and 10^{-8} . Oscillations are absent in the former case, but are visible in the latter case. As $\frac{gf_r}{\lambda}$ increases the signal is less damped with time and harmonics can be observed. Would the damping be stronger by a factor of four, or the intergyre-gyre or the air-sea feedback be weaker by a factor of four, no oscillations would be expected. Would the damping be weaker or the intergyre gyre or the air-sea feedback be stronger, more oscillations would be expected to be visible.

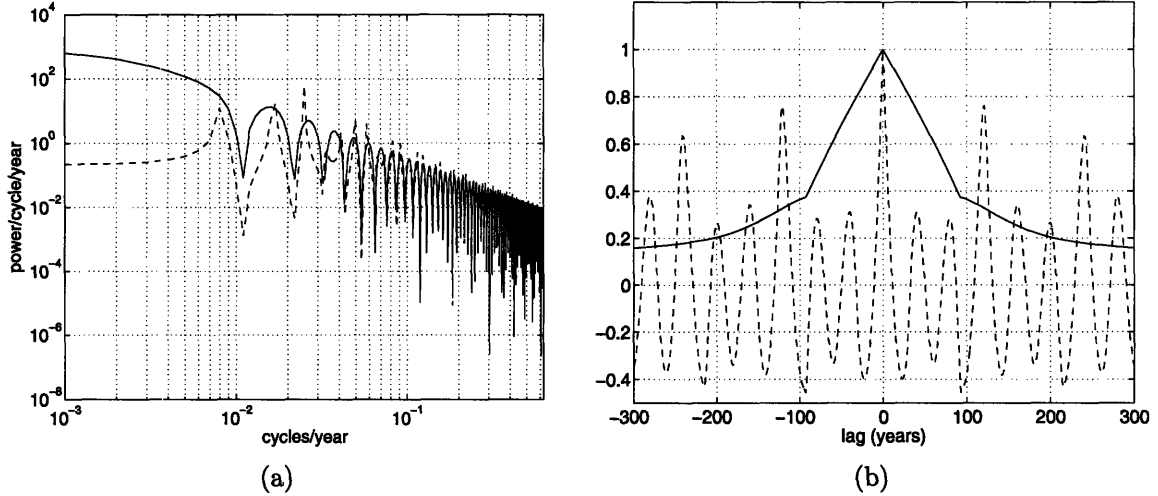


Figure 5-15: (a) Power spectrum of the first PC of baroclinic pressure with $\frac{gf_r}{\lambda} = 10^{-10}$ (solid) and $\frac{gf_r}{\lambda} = 10^{-8}$ (dashed). (b) Auto-correlation of the first PC of baroclinic pressure with $\frac{gf_r}{\lambda} = 10^{-10}$ (solid) and $\frac{gf_r}{\lambda} = 10^{-8}$ (dashed)

Figure 5-15(a) shows the theoretical power spectrum of the baroclinic streamfunction computed using values of $\frac{gf_r}{\lambda}$ equal to 10^{-10} and 10^{-8} . The two curves are similar at high frequencies, but the latter is lower at low frequencies. This low-frequency drop generates a peak at centennial timescales in the latter case, while this peak is absent in the former case. This is reminiscent of the work by D'andrea et al. [10] who attempted to confirm the ideas of Marshall et al. [18] by studying coupled atmosphere-ocean dynamics in the North Atlantic using a simple model featuring a three-layer quasi-geostrophic atmosphere coupled to a slab ocean. They showed the existence of a feedback at decadal timescales and longer that could reduce the power of the NAO at low frequencies. In our case the presence of a feedback would thus reduce the power of the annular modes at very long time scales. The presence of a drop in the power spectrum of the baroclinic streamfunction and of the annular modes at low frequencies in the ridge (see figures 3-4(b) and 3-2(a)) is thus in accordance with the existence of such a feedback.

The mechanism by Marshall et al. [18] is a possible explanation for the centennial oscillation observed in the ridge. However this mechanism invokes the existence of an air-sea feedback to explain an oscillation which persists for hundreds of years. To make sure that it is this mechanism rather than a mechanism internal to the ocean that is responsible for the centennial oscillations observed in the ridge ocean-only runs forced by winds that do not contain any oceanic feedback should be realized.

Chapter 6

Drake

As an illustration of the study developed in the previous chapters and in order to link it to the real world, a third configuration, the Drake, was used. As shown by figure 6-1 the setup is similar to the ridge case in the northern hemisphere, but the land barrier now extends only to the line of -45° of latitude in the southern hemisphere. This configuration is therefore closer to the real world than the aquaplanet or the ridge, since a Drake passage is thus enabled.

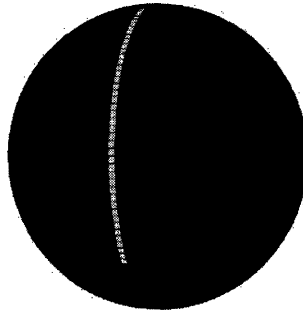


Figure 6-1: Illustration of the Drake configuration

6.1 Mean state

Figure 6-2(a) shows the wind patterns in the Drake as a function of latitude and pressure. In the northern hemisphere winds resemble the ones in the ridge (see figure 2-2(a)). In the southern hemisphere winds are slightly weaker and slightly shifted towards the pole, as in the aquaplanet. However there are easterlies at the poles and no ice is observed there which is a significant difference with the aquaplanet. Figure 6-2(b) shows the mean barotropic streamfunction in the Drake. In the northern hemisphere the situation is similar to the ridge, with gyres of strength and location comparable to the ones found in the ridge. In the southern hemisphere however a strong zonal current of $300 Sv$ is observed at high latitudes, while a subtropical gyre is generated at low latitudes. The southern hemisphere therefore seems to be in between

the case of the ridge and the aquaplanet. In the former gyres were present at every latitude and in the latter only zonal currents were enabled.

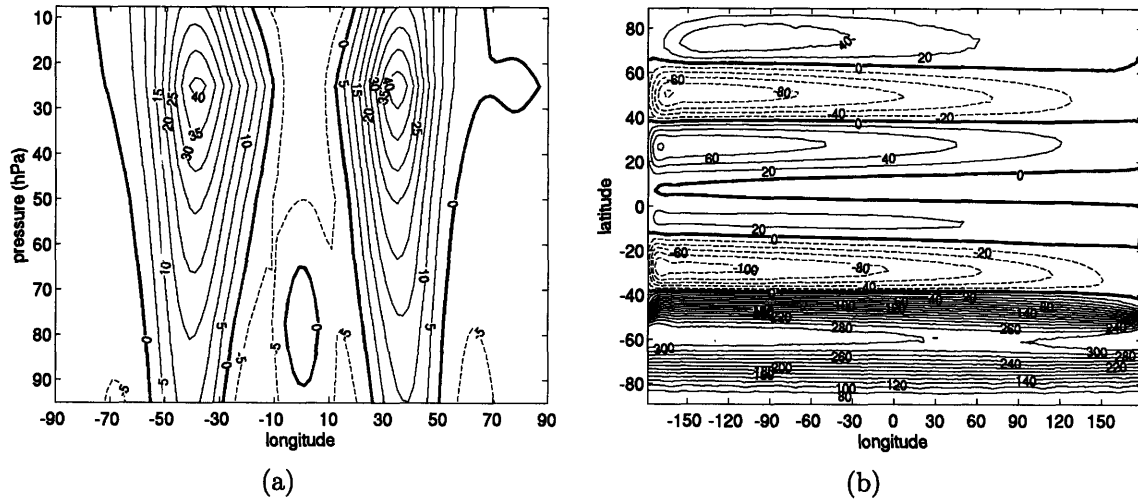


Figure 6-2: (a) zonal wind in the Drake as a function of latitude and pressure, in units of m/s (b) barotropic streamfunction on the lat-long grid. Units are Sv

6.2 Variability in the northern hemisphere

Figure 6-3(a) shows the pattern of the first EOF of SST in the northern hemisphere of the Drake. It is a tripole which is very similar to the one obtained in the ridge, both in shape and amplitude. Figure 6-3(b) shows the auto-correlation of the first PC of SST. This auto-correlation reveals a 120 years oscillation period which resembles the one obtained from the second EOF of SST in the ridge experiment. Figure 6-4(a) shows the regression of SST onto the PC of the first zonal wind EOF at lag -1 . It is the SST tripole of the first EOF of SST. Figure 6-4(b) shows the regression of SST onto the PC of the first zonal wind EOF at lag -2 . It resembles the pattern of the second EOF of SST in the ridge. The first EOF in the Drake therefore appears to capture both the short-term tripole and the long-term signal. The reason for this might have to do with the fact that both anomalies are localized at similar latitudes but have very different time scales.

In the northern hemisphere of the Drake experiment the setup is very similar to the one in the ridge, with a band of land that extends from the north pole to the equator. The mechanism observed there appears to be the one discussed in the ridge: a stochastically generated SST tripole is rapidly damped and a more persistent blob of anomalous SST oscillates with a period of 120 years.

6.3 Variability in the southern hemisphere

Figure 6-5(a) shows the pattern of the first EOF of SST in the southern hemisphere of the Drake. It is a tripole that resembles the one observed in the northern hemisphere,

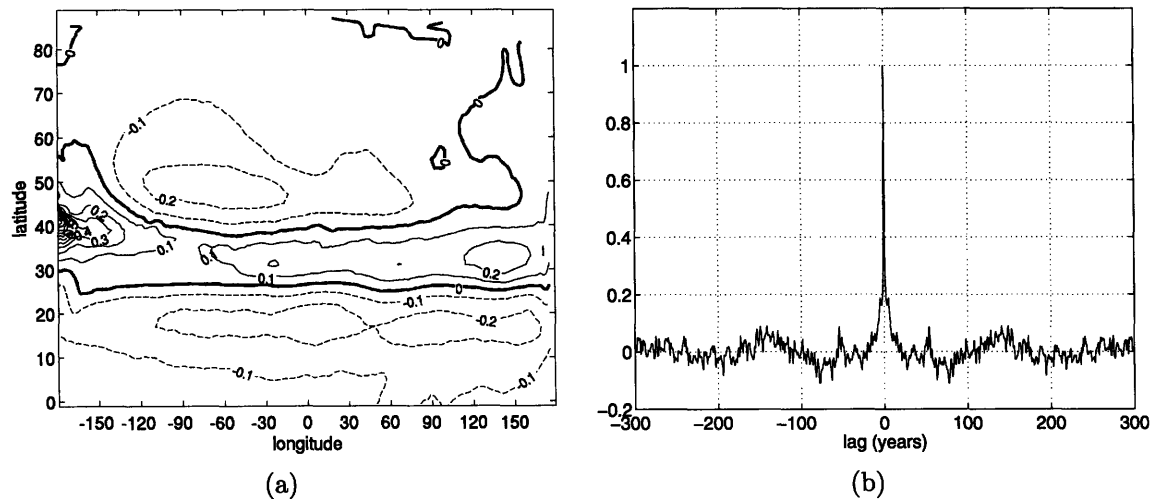


Figure 6-3: (a) pattern of the first EOF of SST in the northern hemisphere of the Drake. Units are $^{\circ}C$. (b) Auto-correlation of the first PC of SST in the northern hemisphere of the Drake from the GCM experiment

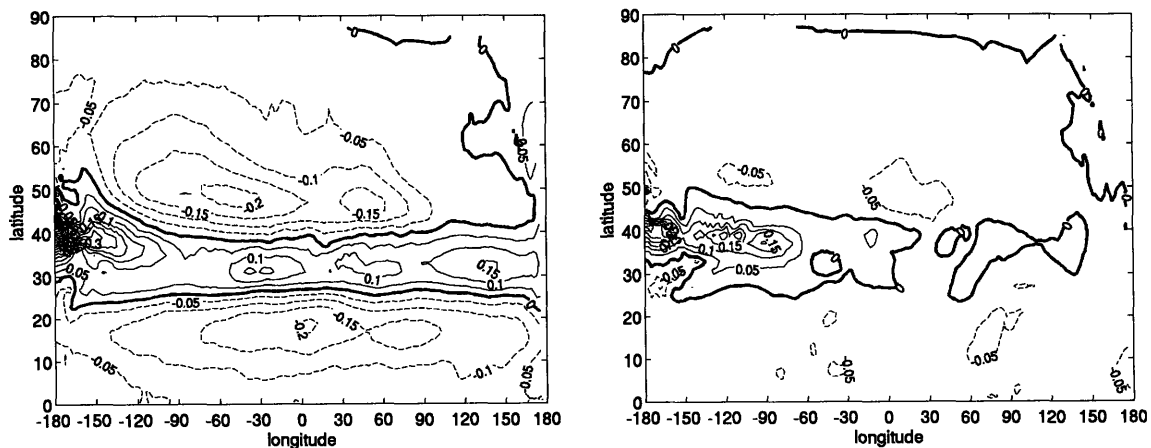


Figure 6-4: Regression of SST onto the PC of the first zonal wind EOF with lags -1, and -2 years (from left to right) in the northern hemisphere of the Drake.

but the amplitude of which is 2 to 3 times larger. The corresponding auto-correlation is sketched in figure 6-5(b). It exhibits a rather sharp peak at small lags, as well as a weak oscillation at decadal time-scales. This oscillation is more easily seen in the atmosphere as illustrated by figure 6-5(b). This oscillation confirms that it is the weakness of the amplitude of the tripole that prevents any oscillation from taking place in the ridge.

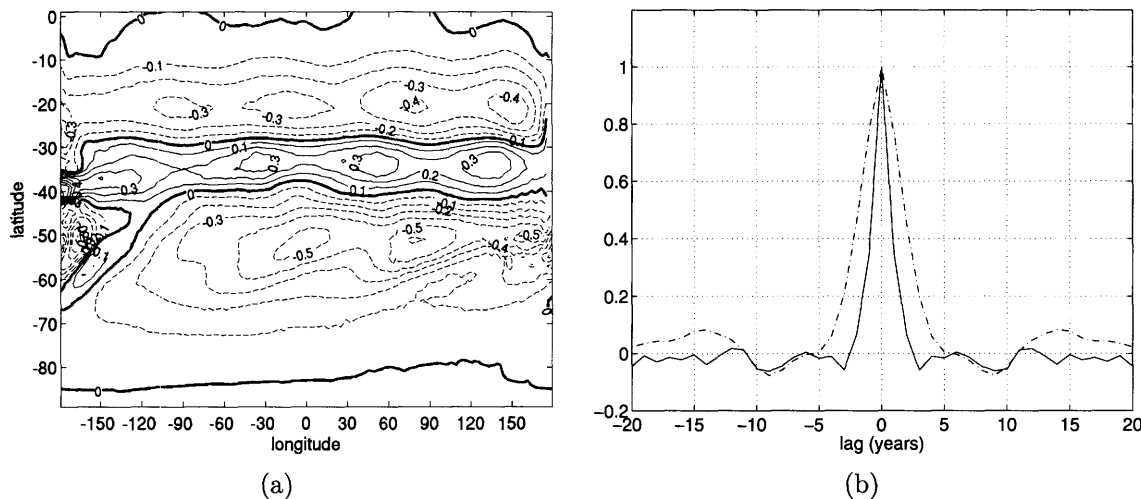


Figure 6-5: (a) pattern of the first EOF of SST in the southern hemisphere of the Drake. Units are $^{\circ}C$. (b) auto-correlation of the first PC of SST (solid) and of the first PC of air surface temperature (dash-dotted) in the southern hemisphere of the Drake

In order to understand the evolution of the SST anomaly with time, the regression of SST onto the PC of the first EOF of zonal wind was computed for several lags. The result of this computation is sketched in figures 6-6(a) to 6-6(f). The tripole is visible at lag 0 but is substantially stronger at lag -1 . In the aquaplanet the northern part of the dipole was found to be slightly stronger at lag -1 , but the southern part of the dipole was found to be significantly weaker at lag -1 . At lag -2 the pattern is negative and of weaker amplitude, which does not relate to any of the mechanisms discussed in the ridge or the aquaplanet. At lag -4 the pattern is a weak tripole the signs of which are the same as the initial tripole. At lags -6 and -8 years the remaining signal is weak and reminds the second EOF of SST in the ridge. However no centennial oscillations could be detected in this case.

In the southern hemisphere of the Drake experiment the setup reminds both the ridge and the aquaplanet. A stronger SST tripole is formed, as in the ridge, and seems to feedback on the atmosphere, as in the aquaplanet. It is not clear whether an oscillation occurs. A further specific study would thus be necessary in order to understand variability in the southern hemisphere of the Drake. We would expect an aquaplanet with a band of land extending from the North pole to the equator to behave similarly to the aquaplanet in the southern hemisphere. But in this case the setup is different enough from the aquaplanet or the ridge for a third mechanism to take place.

Chapter 7

Conclusions

Mechanisms of air-sea interaction and their relation to modes of climate variability were investigated using the coupled MIT GCM through two simple configurations: an aquaplanet in which gyres are absent and a ridgeworld where a ridge extending from pole to pole enables gyres in the ocean. An EOF analysis revealed the presence of atmospheric annular modes in both cases associated with almost white spectra at periods longer than a year. A decadal mode of variability was detected in the atmosphere and the ocean of the aquaplanet. This decadal variability was not observed in the ridge, where a weaker centennial mode of variability was found.

In the aquaplanet stochastic variability inherent to the annular modes in the atmosphere was found to be driving a SST dipole mainly through Ekman pumping. This anomalous SST was shown to be advected southwards by the mean flow, while being slowly damped by air-sea heat fluxes. An air-sea feedback was found to substantially diminish this damping, the atmosphere thereby enhancing the existing dipole through Ekman pumping. A simple stochastic model in the spirit of Saravanan and Mc Williams [23] involving stochastic wind forcing, advection by mean currents, and air-sea heat fluxes was found to capture the essence of the model. In particular decadal oscillations were reproduced.

In the ridge stochastic variability inherent to the annular modes in the atmosphere was found to drive a SST tripole of weaker amplitude than the dipole observed in the aquaplanet. This tripole was found to be generated by Ekman pumping and latent heat fluxes due to wind anomalies and specific humidity anomalies. The weak amplitude of this tripole resulted in a weaker air-sea feedback than in the aquaplanet. Thus damping was not diminished as it was in the aquaplanet and the tripole was quickly damped by air-sea fluxes, preventing any decadal mode of oscillation to occur. The simple stochastic model by Hasselmann [19] was found to capture the mechanism of the evolution of the SST anomalies with time.

In the ridge a weaker SST signal was found to oscillate with a period of 120 years. A similar oscillation occurred in the baroclinic streamfunction at a depth of 200 meters below the sea-surface. The baroclinic signal was found to be leading the SST signal by a year. The same oscillation was also detected in the atmosphere. Annular modes were found to locally force a baroclinic streamfunction extending over the whole basin with a lag of 1 year, and to induce baroclinic Rossby waves at the eastern boundary.

The forced local signal was then shown to be slowly advected by mean currents, while Rossby waves were found to slowly propagate towards the western boundary. These waves were shown to reach the western boundary on average 60 years after having been generated. It was shown that as the SST pattern formed by baroclinic waves becomes more zonal, an air-sea feedback enables an anomalous dipole to form in the atmosphere. This dipole was found to be weaker than the original dipole and of opposite sign. The process just described could then repeat, yielding oscillations of period 120 years. The simple stochastic model involving air-sea interaction imagined by Marshall et al. [18] was found to reproduce the observed oscillations well. This mechanism implies the existence of an air-sea feedback strong enough to affect the variability of annular modes. The presence of a drop in the power spectrum of the baroclinic streamfunction at low frequencies is in accordance with the existence of such a feedback, as discussed by D'Andrea et al. [10]. However in order to be sure that the centennial oscillations observed in the ridge are not internal to the ocean it would be necessary to integrate an ocean-only model forced by winds that would not include any feedback.

Finally, we discussed whether the results of the ridge and the aquaplanet experiments could explain a third experiment, the Drake, in which the band of land extends from the North pole to the line of 45° of latitude. In the northern hemisphere the mechanisms of variability were found to be very similar to the ones observed in the ridge. In particular a weak tripole was observed, and a centennial mode of variability was found to oscillate with a period of 120 years. In the southern hemisphere however a stronger tripole was observed, which might explain the weak decadal oscillation observed in the atmosphere although the mechanism at stake did not seem to be the one observed in the aquaplanet. In the southern hemisphere of the Drake both the configuration and the observation have elements of both the ridge and the aquaplanet. Further study is necessary in order to understand the mechanisms of variability there. Since the Drake configuration can be regarded as a rough approximation of the contemporary world, variability in the ridge can be regarded as an approximation of the contemporary variability in the northern hemisphere. Because the basin of the ridge is 10 times larger than the Atlantic basin we would expect the centennial oscillation observed in the ridge to correspond to a decadal oscillation in the Atlantic, the evidence of the existence of which is increasing.

Chapter 8

Appendix

8.1 Power spectrum of baroclinic waves

The equation for forced baroclinic long waves as proposed by White [26] is:

$$\frac{\partial \Psi}{\partial t} + c_r \frac{\partial \Psi}{\partial x} = \text{curl}_Z \left(\frac{\tau}{\rho_0 h} \right) \quad (8.1)$$

where Ψ_c is the baroclinic streamfunction, $c_r = -\beta L_\rho^2$ is the wave speed of long Rossby waves, L_ρ is the oceanic deformation radius, β the meridional gradient of the Coriolis parameter, τ the wind-stress and h the mean thickness of the upper layer.

A Fourier transform of equation (8.1) yields:

$$i\omega \hat{\Psi} + c_r \hat{\Psi}_x = \hat{F}_\tau \quad (8.2)$$

where the right hand-side of equation(8.1) was written a stochastic process F_τ and the Fourier transform of $f(t)$ was defined as:

$$\hat{F} = F(\omega) = \int_{-\infty}^{+\infty} f(t) e^{-i\omega t} dt \quad (8.3)$$

where the notation used by Bracewell [25] was used. We thus get the homogeneous equation:

$$i\omega \hat{\Psi} + c_r \hat{\Psi}_x = 0 \quad (8.4)$$

which yields:

$$\hat{\Psi} = C e^{-\frac{i\omega x}{c_r}} \quad (8.5)$$

where C is a constant of integration. A particular solution of equation (8.2) is:

$$\hat{\Psi}_p = \frac{\hat{F}_\tau}{i\omega} \quad (8.6)$$

So expressing that $\hat{\Psi}$ is 0 at the eastern boundary ($x = 0$) yields:

$$i\omega\hat{\Psi} = \hat{F}_\tau \left(1 - e^{-\frac{i\omega x}{c_\tau}}\right) \quad (8.7)$$

The $i\omega$ term allows us to use the derivative theorem relative to Fourier transforms, and the $e^{-\frac{i\omega x}{c_\tau}}$ term results in a delay in the time domain:

$$\frac{\partial\Psi}{\partial t} = F_\tau - F_\tau \left(t - \frac{x}{c_\tau}\right) \quad (8.8)$$

Assuming F_τ of the form $F_o \cos(\omega_0 t)$ and integrating yields:

$$\Psi = F_o \frac{\sin(\omega_0 t)}{\omega_0} + F_o \frac{\sin\left(\omega_0\left(\frac{x}{c_\tau} - t\right)\right)}{\omega_0} \quad (8.9)$$

Using a trigonometric identity we finally get:

$$\Psi(x, t) = \frac{2F_o}{\omega_0} \sin\left(\frac{\omega_0 x}{2c_\tau}\right) \cos\left(\frac{\omega_0 x}{2c_\tau} - \omega_0 t\right) \quad (8.10)$$

which was previously derived by White [26]. The power spectrum of the signal can be derived from equation (8.7). We start by re-writing this equation:

$$\hat{\Psi} = \frac{2\hat{F}_\tau e^{-\frac{i\omega x}{2}}}{\omega} \sin\left(\frac{\omega x}{2c_\tau}\right) \quad (8.11)$$

which yields the power spectrum:

$$\Phi(\omega) = \hat{\Psi}\hat{\Psi}^* = \frac{4\hat{F}_\tau^2}{\omega^2} \sin^2\left(\frac{\omega x}{2c_\tau}\right) \quad (8.12)$$

8.2 Forcing of the first EOF of SST in the aqua-planet

The total heat flux can be written as the sum of latent, sensible, longwave and shortwave fluxes:

$$Q = Q_{La} + Q_{Se} + Q_{LW} + Q_{SW} \quad (8.13)$$

These fluxes were regressed on the first PC of SST with a lag of two months. Latent and sensible heat fluxes were found to be the dominant ones, as in several studies making use of real data (see for example Sterl et al. [2], or Cayan [8]).

Figure 8-1(a) shows the regression of latent fluxes onto the first PC of SST at lag 2 months (two months before the SST pattern materializes) in the aquaplanet. This pattern consists in a dipole centered on the line of 45° of latitude and that extends from 30° to 60° of latitude. It is negative in the south and positive in the north and reaches extremum values of -3 and $+4W/m^2$ there. This dipole is therefore very similar to the total heat flux dipole of figure 4-1(b) but with weaker values in the north. Figure 8-1(b) shows the corresponding latent heat flux anomaly. It is a dipole

centered on the line of 45° of latitude and extends from 30° to 60° of latitude. It is negative in the south and positive in the north and reaches extremum values of -1 and $+4W/m^2$ there. Latent and sensible fluxes can be approximated from the bulk formula:

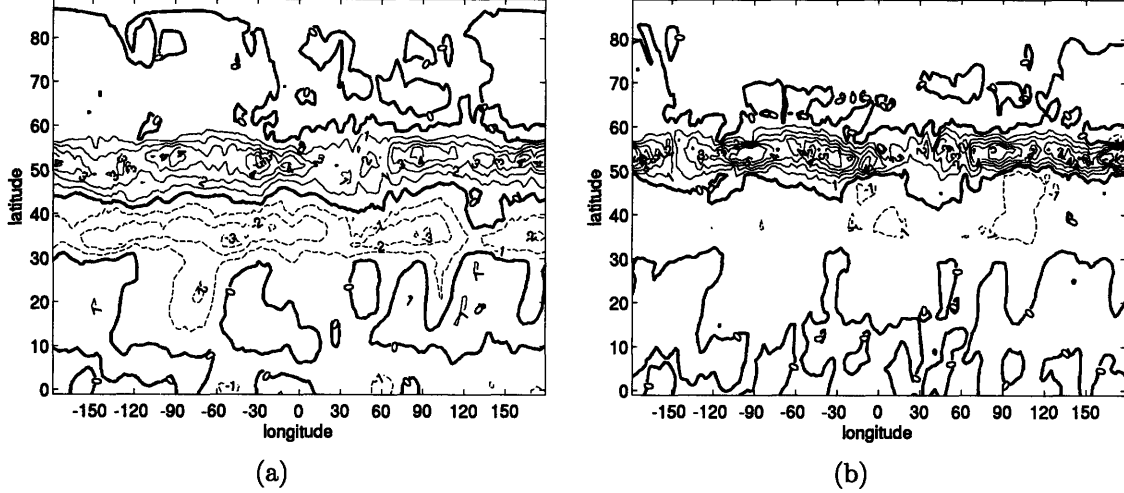


Figure 8-1: (a) regression of latent heat fluxes onto the first PC of SST at lag 2 months (two months before the SST pattern materializes) in the aquaplanet. Units are W/m^2 and positive fluxes are downwards. (b) regression of sensible heat fluxes onto the first PC on SST at lag 2 months in the aquaplanet. Units are W/m^2

$$Q_{La} = \rho_a L_a C_E |\mathbf{v}| (q^* - q^a) \quad (8.14)$$

$$Q_{Se} = \rho_a C_p C_H |\mathbf{v}| (T - T^a) \quad (8.15)$$

In these equations ρ_a is the air density, L_a the latent heat of evaporation of water, C_E the transfer coefficient for latent heat, $|\mathbf{v}|$ the absolute velocity at the surface, q^* the saturation specific humidity, q^a the specific humidity of the air, C_H the transfer coefficient for sensible heat, C_p the specific heat of air at constant pressure, T the SST, and T^a the air temperature at the surface. We expect $|\mathbf{v}|$, q^* , q^a and T^a to be the parameters playing a role in the formation of the SST tripole as ρ_a , C_E and C_H are not expected to vary significantly.

Equations (8.14) and (8.15) can be approximated in terms of time means and anomalies:

$$Q_{La} = \rho_a L_a C_E (|\mathbf{v}'| \overline{(q^* - q^a)} + \overline{|\mathbf{v}|} q^{*'} - \overline{|\mathbf{v}|} q^{a'}) \quad (8.16)$$

$$Q_{Se} = \rho_a C_p C_H (|\mathbf{v}'| \overline{(T - T^a)} + \overline{|\mathbf{v}|} T' - \overline{|\mathbf{v}|} T^{a'}) \quad (8.17)$$

Each term of equation (8.16) and (8.17) was then regressed on the first PC of SST with a lag of two months. Figure 8-2(a) shows the first term on the right hand-side of equation (8.16), which is due to wind anomalies. Above 20° of latitude this

term appears to be a weak tripole. The first band of this tripole extends from 20° to 30° of latitude and reaches an extremum of $-1.5W/m^2$. The second band of the tripole extends from 30° to 45° of latitude and reaches a maximum of $+1.5W/m^2$. The third band extends from 45° of latitude to the pole with a weaker extremum of $-0.5W/m^2$. Below the line of 20° of latitude some positive anomalies are observed. Consider the zonal wind speed showed in figure 2-3(a). Let's assume that the wind pattern moves north by a few degrees. This results in a westward wind anomaly below 45° of latitude, and an eastward wind anomaly above this latitude. From 20° to 30° of latitude the wind is westward, so the westward anomaly translates into a positive anomaly of $|v|$. From 30° to 45° of latitude the wind is eastward, so the westward anomaly translates into a negative anomaly of $|v|$. Above 45° of latitude the wind is eastward, so the eastward anomaly translates into a positive anomaly of $|v|$. This yields the previously described tripole, the signs of which are opposite to the ones deduced above because of the convention of flux that was chosen.

Figure 8-2(b) shows the sum of the second and third terms of equation (8.16) which are due to anomalies of saturation specific humidity and anomalies of the specific humidity of the air. Both are dipoles and so is the resulting pattern of their sum. It is centered on the line of 40° of latitude and extends from 30° to 60° of latitude. It is negative in the south and positive in the north and reaches extremum values of $-2W/m^2$ and $+1W/m^2$ there. This dipole explains the heat flux pattern of figure 8-1(a), although its amplitude is smaller: this amplitude difference might be due to the constants used in the bulk formulation of the latent heat flux.

The dominant terms of equation (8.17) were found to be the terms due to SST and air surface temperature. The first term of equation (8.17) which is due to wind anomaly is not shown here as it was found to be negligible due to a small $\overline{T - T^a}$ term in the aquaplanet. Figure 8-2(c) shows the sum of the second and third term on the right hand-side of equation (8.17), which are due to SST and air temperature anomalies. It is a dipole which is similar to the dipole of latent heat fluxes of figure 8-1(b) both in shape and amplitude. The sensible heat flux pattern is therefore mainly due to SST and air temperature anomalies in this case.

Figure (8-3) shows a cross-correlation of the first PC of the specific humidity of the air, the air surface temperature, and the surface wind stress with the first PC of SST at different lags. The wind appears to be correlated to the SST for 10 months, although this correlation is not very strong. This feature is very different from the ridge case (see below) where this correlation was found to be less persistent and of stronger amplitude. The zonal character of the aquaplanet and the fact that all the anomalies discussed above are dipoles located at the same latitude than wind anomalies might explain this persistence. Air temperature and the specific humidity of the air appear to be more highly correlated with the SST. These correlations reach their maximum at lag 0 which indicates that it is the wind alone that forces the SST in this case.

This encourages us to sum the atmospheric anomalies that lead the SST:

$$\rho_a L_a C_E (|v| \sqrt{q^* - q^a}) + \frac{C_o \tau'_x}{f} \frac{\partial \overline{T}}{\partial y} \quad (8.18)$$

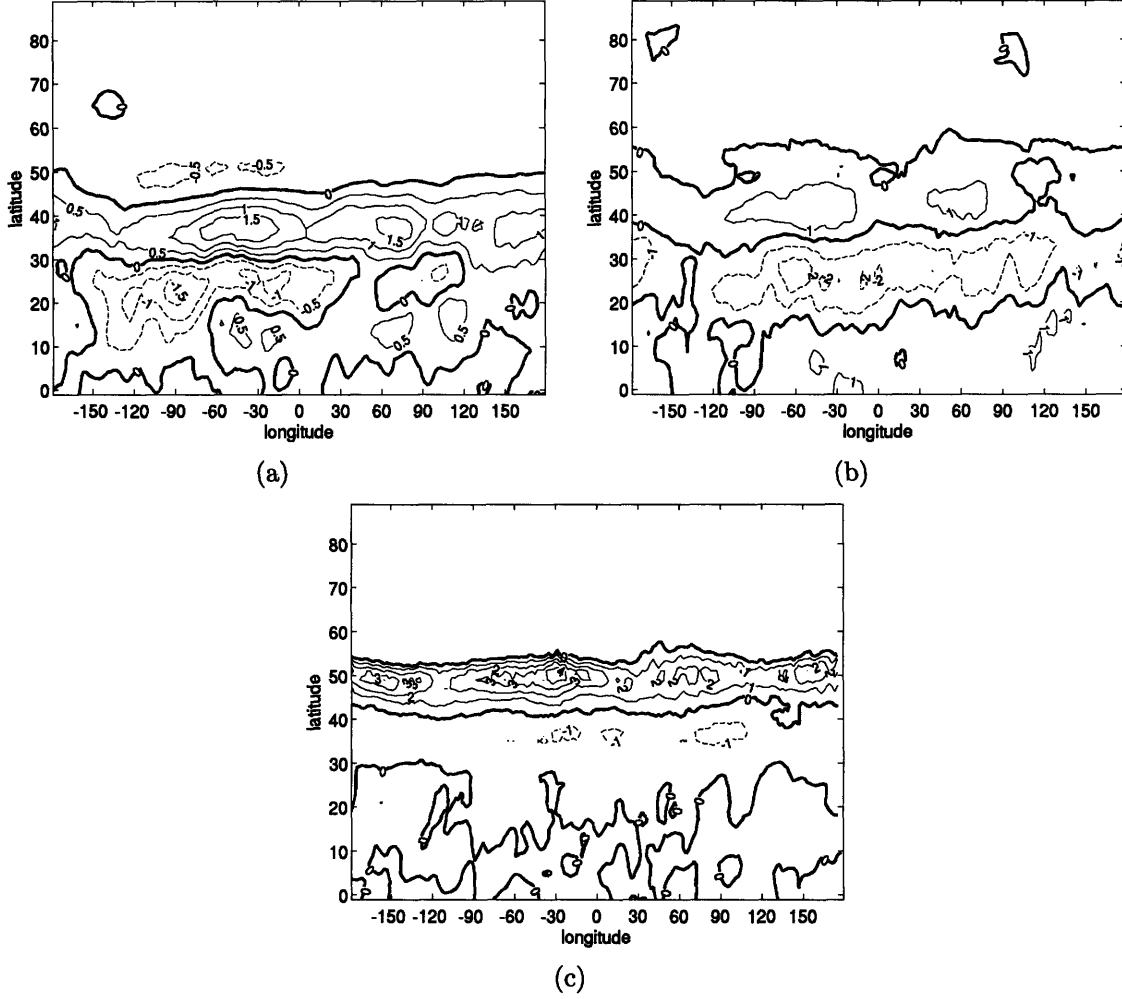


Figure 8-2: regression of latent and sensible fluxes onto the first PC of SST in the aquaplanet at lag 2 months: (a) $\rho_a C_o L_a |v|'(\bar{q}^* - q^a)$, (b) $\rho_a C_o L_a |v|'(q^{*'} - q^{a'})$ (c) $\rho_a C_p C_H |v|'(T' - T^{a'})$. Units are W/m^2 and positive fluxes are downwards

8.3 Solution of the idealized coupled model in the aquaplanet

We consider the SST equation:

$$\rho_o C_o h \frac{\partial T'}{\partial t} + \rho_o C_o h \bar{V}_{res} \frac{\partial T'}{\partial y} = \frac{C_o F_\tau}{f} \frac{\partial \bar{T}}{\partial y} - \lambda_{HF} T' - \lambda_{Ek} T' \quad (8.19)$$

In this equation \bar{V}_{res} is the mean residual velocity advecting the SST anomalies as seen on figure (4-3). λ_{HF} and λ_{Ek} are the damping term due to air-sea heat fluxes and the feedback term due to Ekman transport. F_τ is the part of the wind stress due to internal atmospheric dynamics, modeled as a white noise process in time but with large-scale standing pattern in space:

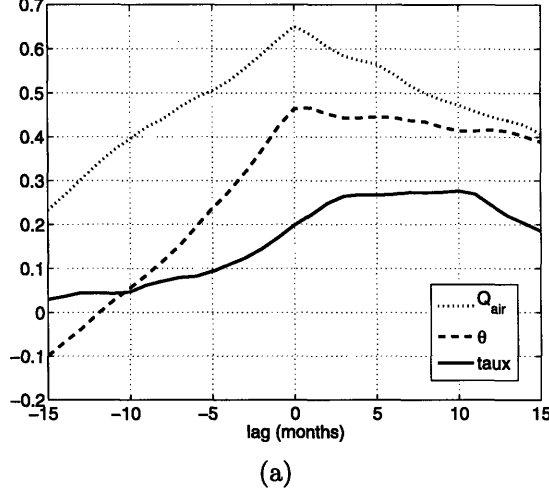


Figure 8-3: (a) cross-correlation of the first PC of SST with the first PC of q^a the specific humidity of the air (dotted), the first PC of θ air temperature at the surface (dashed), and the first PC of τ_x zonal wind stress at the surface (solid) in the aquaplanet. A positive lag indicates that the atmosphere leads the ocean

$$F_\tau = N(t)\sin(ky) = N(t)\sin\left(\frac{2\pi y}{L}\right) \quad (8.20)$$

where $y = 0$ corresponds to the northernmost latitude of the first EOF of SST, 60° , and $y = -L$ corresponds to the southernmost latitude of the first EOF of SST, 30° .

A Fourier transform of equation (8.19) yields:

$$\left(-i\omega + \frac{\lambda}{\rho_o C_o h} + \bar{V}_{res}\partial_y\right)\hat{T} = \delta\hat{N}\sin(ky) \quad (8.21)$$

where $\hat{T} = \hat{T}(\omega, y)$, $\hat{N} = \hat{N}(\omega)$, and $\delta = \frac{1}{\rho_o f h} \frac{\partial \bar{T}}{\partial y}$, and $\lambda = \lambda_{HF} + \lambda_{Ek}$.

We know the solution is of the form:

$$\hat{T} = a e^{-\frac{(\lambda-i\omega)}{\bar{V}_{res}}y} + b \cos(ky) + c \sin(ky) \quad (8.22)$$

Coefficients b and c are determined by substituting equation (8.22) into equation (8.21). At the ice line $T = 0$, so coefficient a is obtained from the boundary condition $\hat{T}(y = 0, t) = 0$. The solution can thus be written:

$$\hat{T} = \frac{k\bar{V}_{res}\delta\hat{T}}{k^2\bar{V}_{res}^2 + (\lambda - i\omega)^2} \left(e^{-\frac{(\lambda-i\omega)}{\bar{V}_{res}}y} + \frac{\lambda - i\omega}{k\bar{V}_{res}}\sin(ky) \right) \quad (8.23)$$

The term of equation (8.23) which is outside the brackets depends only on frequency, while the term within the brackets includes a spatial modulation. Equation (8.24) is the spectrum of the first term which was found to be a good approximation of the spectrum:

$$\Phi(\omega) = \frac{k^2 \bar{V}_{res}^2 |\hat{N}|^2}{\left(k^2 \bar{V}_{res}^2 - \omega^2 + \frac{\lambda^2}{(\rho_o C_o h)^2}\right)^2 + 4\omega^2 \frac{\lambda^2}{(\rho_o C_o h)^2}} \quad (8.24)$$

8.4 Forcing of the first EOF of SST in the ridge

The total heat flux can be written as the sum of latent, sensible, longwave and shortwave fluxes:

$$Q = Q_{La} + Q_{Se} + Q_{LW} + Q_{SW} \quad (8.25)$$

These fluxes were regressed on the first PC of SST with a lag of two months. As in the aquaplanet latent and sensible heat fluxes were found to be the dominant ones. Figure 8-4(a) shows the latent heat flux which compares well to the pattern of total heat flux discussed above (figure 5-1(b)) both in shape and amplitude, although it appears to be weaker at the basin boundaries. This difference is due to the sensible heat flux which is sketched in figure 8-4(b). This flux is negligible in the interior compared to the latent heat flux, but reaches maximum values of $4W/m^2$ and $3W/m^2$ at the western and eastern boundaries. As in the case of the aquaplanet latent and sensible fluxes can be approximated as:

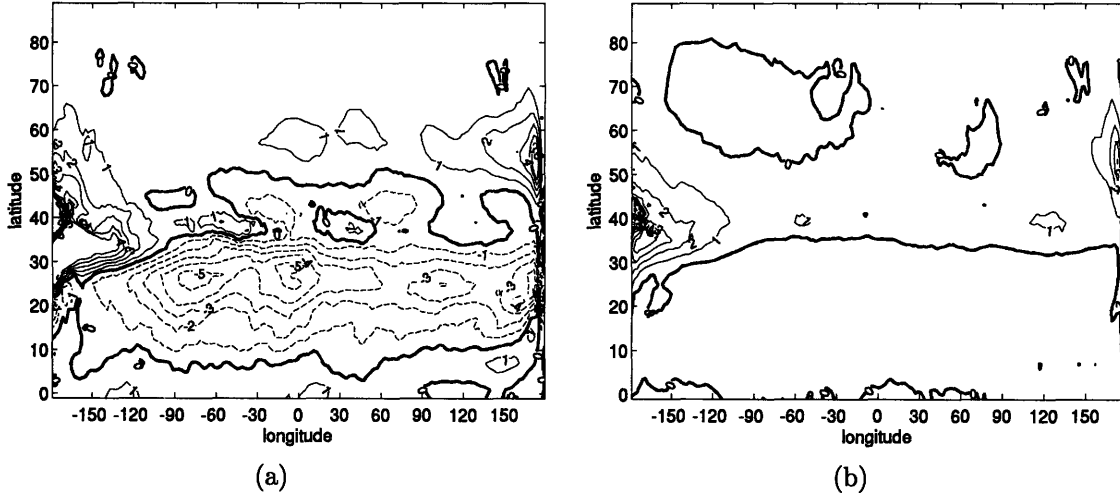


Figure 8-4: (a) regression of latent fluxes onto the first PC of SST at lag 2 months (two months before the SST pattern materializes) in the ridge. Values above $10W/m^2$ were discarded for readability. Units are W/m^2 and positive fluxes are downwards. (b) regression of sensible fluxes onto the first PC on SST at lag 2 months in the ridge. Units are W/m^2

$$Q_{La} = \rho_a L_a C_E (|\mathbf{v}'| (\overline{q^* - q^a}) + \overline{|\mathbf{v}| q^{*'}} - \overline{|\mathbf{v}| q^{a'}}) \quad (8.26)$$

$$Q_{Se} = \rho_a C_p C_H (|\mathbf{v}'| (\overline{T - T^a}) + \overline{|\mathbf{v}| T'} - \overline{|\mathbf{v}| T^{a'}}) \quad (8.27)$$

Each term of equations (8.26) and (8.27) was then regressed on the first PC of

SST with a lag of two months. Figure 8-5(a) shows the first term on the right hand-side of equation (8.26), which is due to wind anomalies. It is a quadrupole with a zonal structure. A first negative band extends from 10° to below 30° of latitude and reaches values of $-7W/m^2$ in the interior. A second positive band extends from below 30° to below 40° of latitude and reaches values of $4W/m^2$ in the interior. A third band extends from below 40° to 55° of latitude and reaches values of $-4W/m^2$ in the interior. The fourth positive band extends from 55° to 70° of latitude and is weaker, with a maximum of $1W/m^2$ in the interior. This quadrupole is a direct consequence of the wobbling of the zonal jet. Consider the zonal wind speed showed in figure 2-3(a). Let's assume that the wind pattern moves north by a few degrees. This results in a westward wind anomaly below 39° of latitude, and an eastward wind anomaly above this latitude. From 15° to 27° of latitude the wind is westward, so the westward anomaly translates into a positive anomaly of $|v|$. From 27° to 39° of latitude the wind is eastward, so the westward anomaly translates into a negative anomaly of $|v|$. From 39° to above 50° of latitude the wind is eastward, so the eastward anomaly translates into a positive anomaly of $|v|$. Above 50° of latitude the wind is westward, so the eastward anomaly translates into a negative anomaly of $|v|$. This yields the quadrupole of figure 8-5(a) the signs of which are opposite to the ones deduced above because of the convention of flux that was chosen.

Figure 8-5(b) shows the second term on the right hand-side of equation (8.26), which is due to anomalies of saturation specific humidity. It is a tripole centered on the line of 40° of latitude which reaches extrema of $\pm 5W/m^2$ and which contributes to the damping of the SST tripole. This pattern is a consequence of q^* being a function of SST.

Figure 8-5(c) shows the third term on the right hand-side of equation (8.26), which is due to anomalies of the specific humidity the air. In the interior the most significant signal is observed between the lines of 25° and 40° of latitude, where it reached an extremum value of $-5W/m^2$. At the basin boundaries positive anomalies are observed which reach maximal values of $+5W/m^2$. At the boundaries and above the line of 45° of latitude q^a acts as to balance q^* . However from 25° to 40° of latitude the anomaly due to the specific humidity of the air might be due to some atmospheric forcing.

Terms of equation (8.27) were found to be of smaller influence and hence were not plotted here. The first term on the right hand-side of equation (8.27) was found to explain the weak pattern observed in the interior of figure 8-4(b). The two other terms were found to be tripoles of opposite strength the sum of which was found to explain the stronger signal detected at the boundaries of figure 8-4(b).

Figure 8-6(a) shows a cross-correlation of the first PC of the parameters of equations (8.26) and (8.27) with the first PC of SST. Wind and specific humidity of the air appear to be leading the SST by two months, and the air temperature and specific humidity at saturation by one month. Although q^* seems to respond to the SST, as seen above, it nevertheless seems to affect it, since it leads the SST signal by one month. But more interestingly it seems that it is the atmosphere, via the wind and q^a that leads every anomaly. As seen above, the sensible heat flux was found to be small, except at the boundaries, where an anomaly was due to the difference between

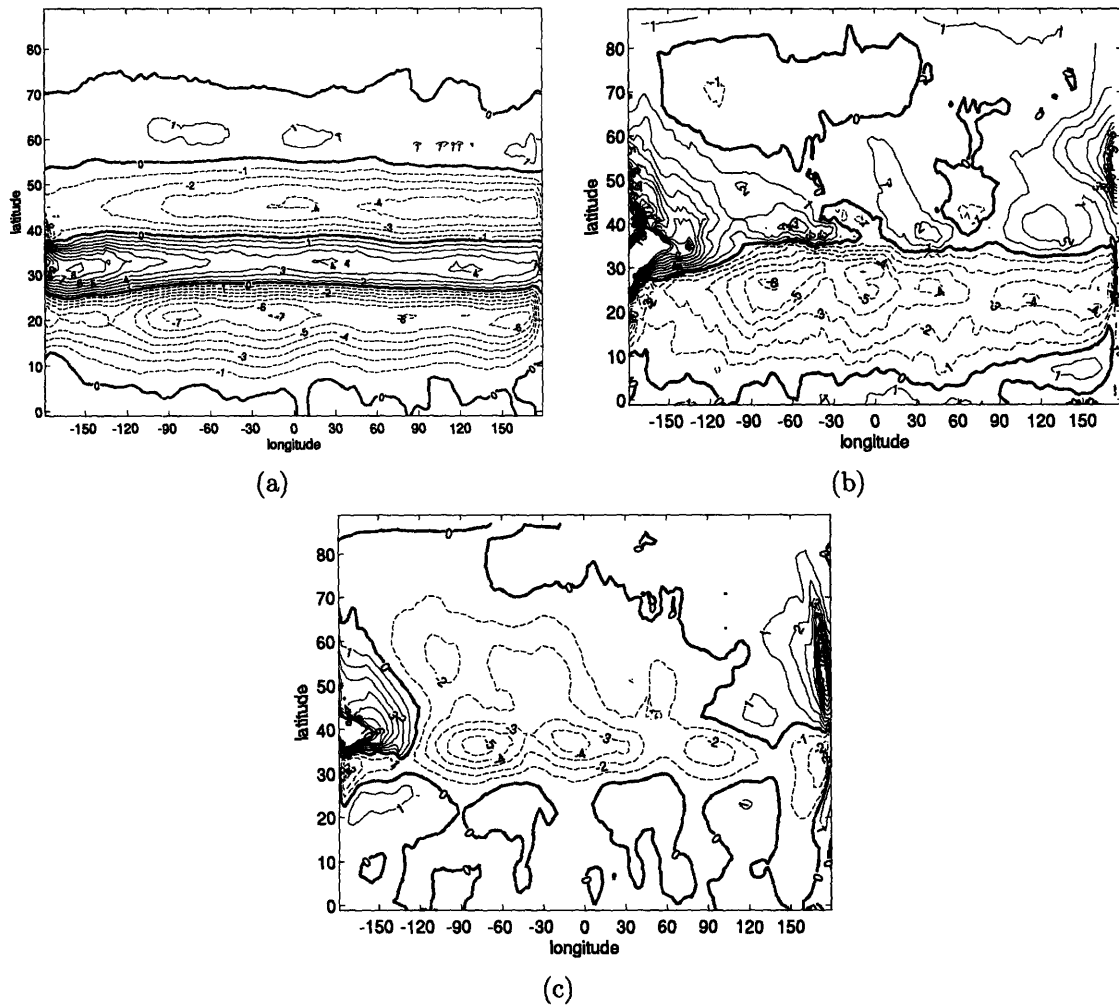


Figure 8-5: regression of latent fluxes onto the first PC of SST in the ridge: (a) $\rho_a C_o L_a |v|'(\overline{q^*} - q^a)$, (b) $\rho_a C_o L_a |v| q^{*'}$, and (c) $-\rho C_o L_a |v| q^{a'}$ at lag 2 months (two months before the SST pattern materializes). Values above $10W/m^2$ were discarded for readability. Units are W/m^2 and positive fluxes are downwards

SST and air temperature. Figure 8-6(a) shows that both saturation specific humidity and air temperature are led by wind anomalies.

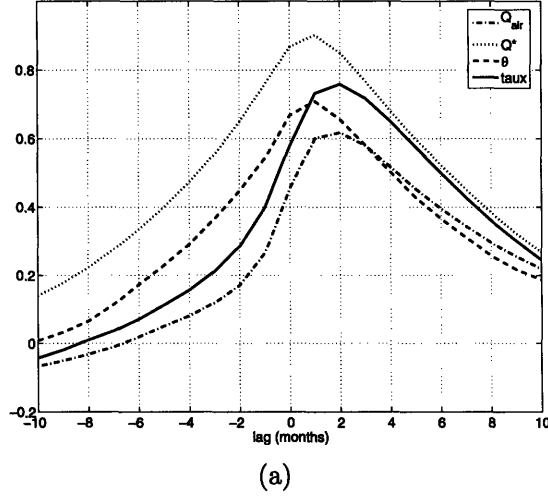


Figure 8-6: (a) cross-correlation of the first PC of SST with the first PC of q^* absolute humidity at the surface (dotted), the first PC of θ air temperature at the surface, the first PC of zonal wind stress τ_x at the surface (solid), and the first PC of q^a , the specific humidity of the air at the surface (dash-dotted) in the ridge. A positive lag indicates that SST lags

This encourages us to sum all the atmospheric anomalies that lead the SST:

$$\rho_a L_a C_E (|\mathbf{v}'| (\overline{q^*} - \overline{q^a}) - \overline{|\mathbf{v}|} q^{a'}) + \frac{C_a \tau'_x}{f} \frac{\partial \overline{T}}{\partial y} \quad (8.28)$$

8.5 Power spectrum of baroclinic waves with air-sea feedback

We consider the set of equations:

$$\begin{cases} \frac{\partial \Psi}{\partial t} + (\overline{U}_g - \beta L_\rho^2) \frac{\partial \Psi}{\partial x} = -\frac{1}{\rho_o h} \frac{\partial \tau_x}{\partial y} \\ \lambda T = g \Psi|_w \\ \tau_x = F_\tau - f_\tau T \end{cases} \quad (8.29)$$

which yields:

$$\frac{\partial \Psi}{\partial t} + c_\tau \frac{\partial \Psi}{\partial x} = F - \frac{g f_\tau}{\lambda} \Psi_{x=-L} \quad (8.30)$$

where F is a stochastic process, $x = -L$ denotes the western boundary of the basin, and c_τ is the effective Rossby wave speed in the basin defined as:

$$c_\tau = \overline{U}_g - \beta L_\rho^2 \quad (8.31)$$

Taking the Fourier transform of equation (8.30) and assuming F to be a stationary random process with zero mean and a white frequency in space yields:

$$i\omega\hat{\Psi} + c_\tau \frac{\partial\hat{\Psi}}{\partial x} = \hat{F} - \frac{gf_\tau}{\lambda} \hat{\Psi}_{x=-L} \quad (8.32)$$

The homogeneous equation brings:

$$\hat{\Psi}_h = Ae^{\frac{i\omega x}{c_\tau}} \quad (8.33)$$

Where A is a constant. Since Ψ must vanish at the eastern boundary we get:

$$\hat{\Psi} = B \left(1 - e^{\frac{i\omega x}{c_\tau}}\right) \quad (8.34)$$

And B is obtained by substituting (8.34) in (8.32):

$$\hat{\Psi} = \frac{\hat{F} \left(1 - e^{\frac{i\omega x}{c_\tau}}\right)}{-i\omega + \frac{gf_\tau}{\lambda} \left(1 - e^{-\frac{i\omega L}{c_\tau}}\right)} \quad (8.35)$$

8.6 Determination of f_τ from atmosphere-only runs

In order to study further the interaction of the SST with the atmosphere, several atmosphere-only runs were integrated. For each one of these runs a different SST forcing was used. In experiment *RwNoEOF* the atmosphere was forced by the mean SST computed from the coupled model with the ridge configuration, the seasonal forcing of which was removed. In experiment *RwEOF* the atmosphere was forced by the previous SST map on which the first EOF of SST in the ridge was superimposed in the northern hemisphere. The corresponding runs in the aquaplanet were denominated by the names *AqNoEOF* and *AqEOF*. Would the SST feedback on the atmosphere the response of the atmosphere to experiments *EOF* and *NoEOF* would then be different. These experiments were thus designed to quantify the SST feedback on the atmosphere. As noted before the amplitude of the first EOF of SST is larger in the aquaplanet than in the ridge by a factor of 2. Because this difference of amplitude could have an impact on air-sea interaction, a fifth experiment, *RwEOF23*, was integrated. In experiment *RwEOF23* the atmosphere was forced by the SST map of experiment *RwNoEOF* on which was superimposed the first EOF of SST in the ridge multiplied by 2 in the northern hemisphere and multiplied by 3 in the southern hemisphere. This experiment was designed to understand the impact of the amplitude of the SST anomaly on its eventual feedback on the atmosphere. Finally experiments *RwEOF₂* and *RwEOF23₂* are the same as experiments *RwEOF* and *RwEOF23* but make use of the second EOF of SST in the ridge instead of the first EOF of SST. Each experiment was integrated over 500 years and made use of a climatology integrated over 100 years.

The atmosphere-only models without EOFs superimposed on the mean SST were found to reproduce well the results of the coupled model.

8.6.1 Forcing with the first EOF of SST in the ridge

Figure 8-7(a) shows the difference between the mean zonal wind stress in experiment *RwEOF* and the mean zonal wind stress in experiment *RwNoEOF*. In the northern hemisphere it reveals a zonal band of magnitude $-0.002N/m^2$ from the equator to 20° of latitude. A signal of magnitude $0.002N/m^2$ can be seen at mid-latitudes. It is possible to quantify f_τ using the amplitude of zonal means of the wind stress and the first EOF of SST. We simply approximate f_τ as:

$$f_\tau = \frac{\Delta\tau_x}{\Delta SST} \quad (8.36)$$

Deltas were computed at the latitudes where the extrema of amplitude of the SST anomalies were found. In this case we find that f_τ is of the order of $0.005N/m^2/K$, which is a small value.

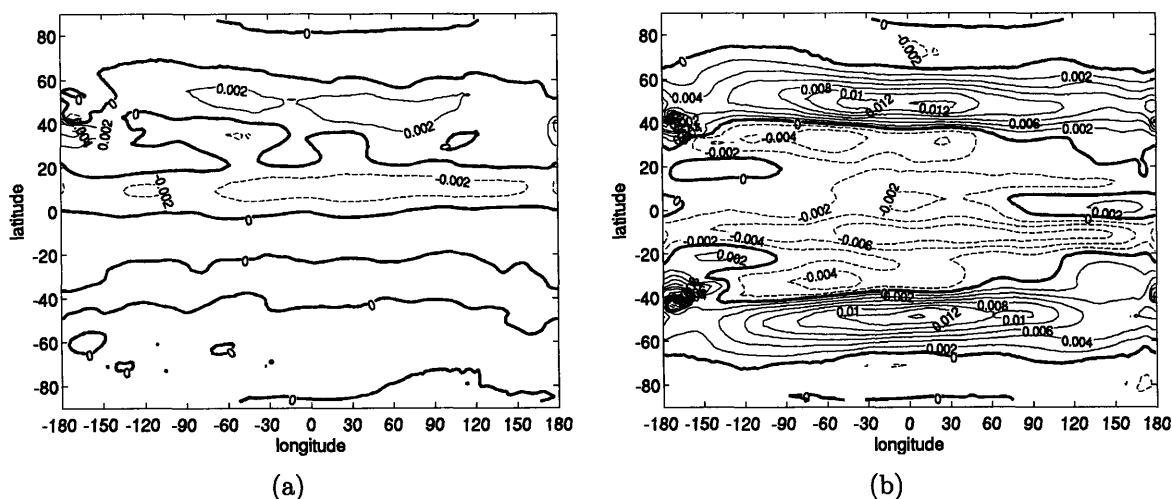


Figure 8-7: (a) difference of mean zonal wind stresses of experiments *RwEOF* and *RwNoEOF*, in N/m^2 (b) difference of mean zonal wind stresses of experiments *RwEOF23* and *RwNoEOF*, in N/m^2

Figure 8-8(a) shows f_τ computed from:

$$f_\tau = -\frac{\langle T^* \tau_x \rangle}{\langle T^* T \rangle} \quad (8.37)$$

As discussed before it appears that $f_\tau c$ does not really exist in the ridge since the curve shown by figure 8-8(a) is probably meaningless at negative lags. The two computations therefore imply that the feedback in the ridge is very small.

Figure 8-7(b) shows the difference between the mean zonal wind stress in experiment *RwEOF23* and the mean zonal wind stress in experiment *RwNoEOF*. In the northern hemisphere, which was forced by twice the first EOF of SST, a positive signal extends to 40° of latitude and reaches a maximum values of $-0.004N/m^2$. Above, a large signal extends up to 70° of latitude and reaches a maximum amplitude of $0.012N/m^2$. At high latitudes a smaller signal of amplitude $-0.001N/m^2$ is observed. Using equation (8.36) we find that $f_\tau = 0.02N/m^2/K$. Would the SST

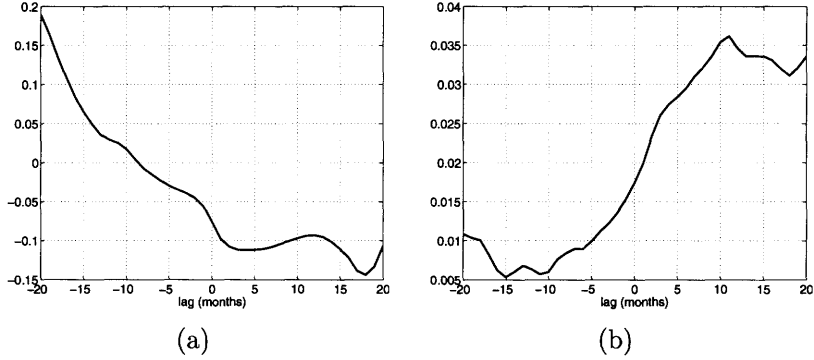


Figure 8-8: (a) f_τ in the ridge (b) f_τ in the aquaplanet

anomaly be stronger it would thus result in a significant air-sea interaction in the ridge. It is thus likely that the weak amplitude of the SST anomaly in the ridge is the reason why there is no feedback from the ocean to the atmosphere in the ridge. In the southern hemisphere, which was forced by three times the first EOF of SST, patterns and values are very similar to the ones found in the northern hemisphere. The only difference is a strong zonal response at the equator, which does not appear in the northern hemisphere. A computation of f shows that the anomalous wind is remarkably similar in both hemispheres, as if a threshold had been reached. Because the forcing is 1.5 times stronger than in the northern hemisphere the feedback is now $f_\tau = 0.01N/m^2/K$. f_τ is thus not a linear function of the amplitude of the SST. If the SST is too weak f is very small, but as the amplitude of SST reaches a specific value, a significant feedback is observed.

8.6.2 Forcing with the second EOF of SST in the ridge

Figure 8-9(a) shows the difference between the mean zonal wind stress in experiment $RwEOF_2$ and the mean zonal wind stress in experiment $RwNoEOF$. In the northern hemisphere, which was forced by the second EOF of SST, a dipole reaching values of $0.002N/m^2$ in the south and $-0.004N/m^2$ in the north can be seen at mid-latitudes. Using equation (8.36) yields a value for the feedback of the order of $0.02N/m^2/K$, which is significantly stronger than in the case of the first EOF of SST.

At the difference of experiment $RwEOF23$ where a wind of similar amplitude was found in both hemispheres, $RwEOF23_2$ yields an air-sea feedback of the same amplitude in both hemispheres, the value of which is $f_\tau = 0.01N/m^2/K$. As in the case of the second EOF of SST f is not a linear function of the amplitude of the SST. However the second EOF of SST is strong enough to enable the existence of a significant air-sea feedback.

8.6.3 Forcing with the first EOF of SST in the aquaplanet

Figure 8-10(a) shows the difference between the mean zonal wind stress in experiment $AqEOF$ and the mean zonal wind stress in experiment $AqNoEOF$. In the northern

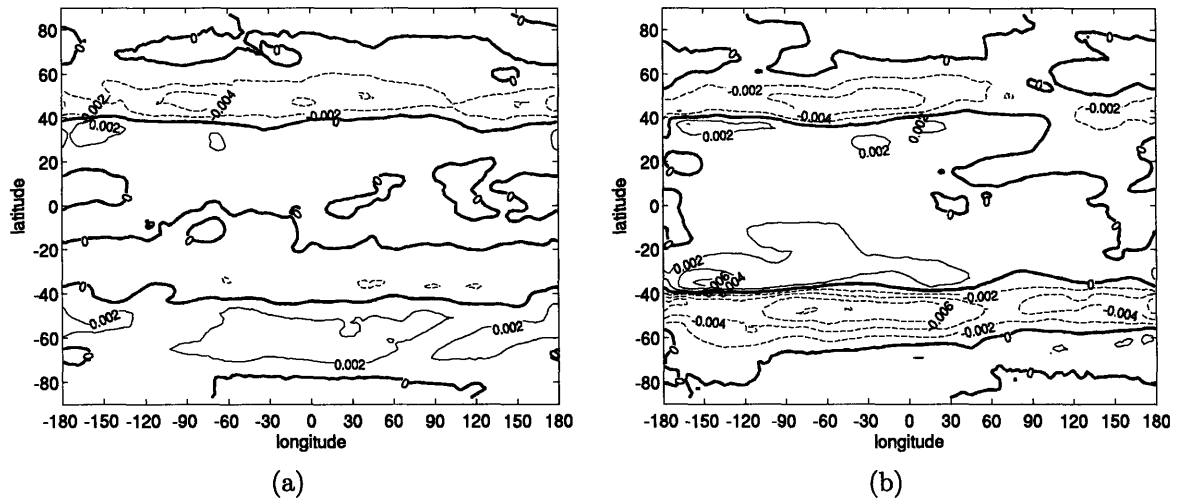
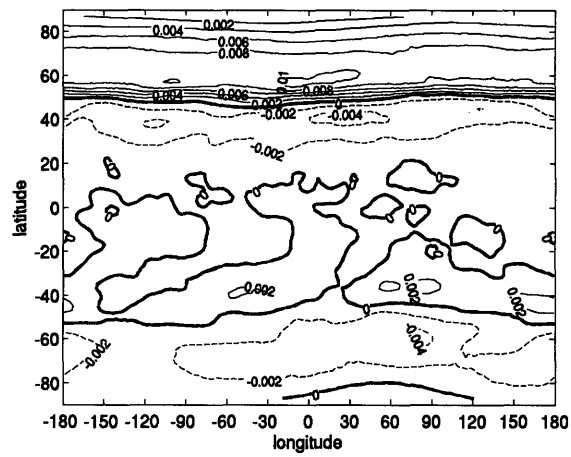


Figure 8-9: (a) difference of mean zonal wind stresses of experiments $RwEOF_2$ and $RwNoEOF$, in N/m^2 (b) difference of mean zonal wind stresses of experiments $RwEOF_{232}$ and $RwNoEOF$, in N/m^2

hemisphere a dipole extends from 20° to the equator, centered on the line of 50° of latitude. Its amplitude varies from $-0.003N/m^2$ in the south to $0.01N/m^2$ in the north. In the southern hemisphere, where no EOF was added to the climatology, amplitudes of the difference in mean wind-stress between the two experiments are of the order of $0.002N/m^2$. Since the patterns are similar in the north and in the south, with weaker amplitudes in the south, it is likely that the pattern seen in the south has to do with the EOF that was added to the climatology in the northern hemisphere and is therefore likely not to be only an error. Be this as it may the SST seems to be feeding back on the atmosphere in this case, as f_τ is found to be $0.015N/m^2/K$. Figure 8-8(b) shows the f_τ parameter computed from equation (8.37). At negative lags (when the SST leads the atmosphere) f_τ is of the order of $0.01N/m^2$. The two calculations thus yield the same order of magnitude for the air-sea feedback, confirming that the SST in the aquaplanet is strong enough to feedback on the atmosphere, which in turn leads to a positive feedback on the SST through Ekman transport anomalies and enables low-frequency oscillations.



(a)

Figure 8-10: (a) difference of mean zonal wind stresses of experiments *AqEOF* and *AqNoEOF*, in N/m^2 (b) difference of mean zonal wind stresses of experiments *AqEOF23* and *AqNoEOF*, in N/m^2

Bibliography

- [1] Adcroft A., Campin J.-M., Hill C.N., and Marshall J. C. Implementation of an atmosphere-ocean general circulation model on the expanded spherical cube. *Mon. Wea. Rev.*, 132(12):2845–2863, 2004.
- [2] Sterl A. and Hazeleger W. Coupled variability and air-sea interaction in the south atlantic ocean. *Climate Dynamics*, 21:559–571, 2003.
- [3] Deser C. and Blackmon M.L. Surface climate variations over the north atlantic ocean during winter: 1900-1989. *J. Climate*, 6:1743–1753, 1993.
- [4] Frankignoul C., Czaja A., and L’Heveder B. Air-sea feedback in the north atlantic and surface boundary conditions for ocean models. *Journal of Climate*, 11:2310–2324, 1997.
- [5] Frankignoul C. and Hasselmann K. Stochastic climate models, part ii. application to sea-surface temperature anomalies and thermocline variability. *Tellus*, 29:289–305, 1977.
- [6] Frankignoul C., Muller P., and Zorita E. A simple model of the decadal response of the ocean to stochastic wind forcing. *J. Phys. Oceanogr.*, 27:1533–1546, 1997.
- [7] Wunsch C. The interpretation of short climate records, with comments on the north atlantic oscillation and southern oscillations. *Bulletin of the American Meteorological Society*, 80:245–255, 1999.
- [8] Cayan D.R. Latent and sensible heat flux anomalies over the northern oceans: driving the sea surface temperature. *Journal of Physical Oceanography*, 22:859–881, 1992.
- [9] Zorita E. and Frankignoul C. Modes of the north-atlantic decadal variability in the ecam/lsg coupled ocean-atmosphere general circulation model. *Journal of Climate*, 10:183–200, 1997.
- [10] D’Andrea F., Czaja A., and Marshall J. Impact of anomalous heat transport on the north atlantic oscillation. *American Meteorological Society*, 18:4955–4969, 2005.

- [11] Molteni F. Atmospheric simulations using a gcm with simplified physical parameterizations. i: model climatology and variability in multidecadal experiments. *Climate Dynamics*, 20(175-191), 2003.
- [12] Stommel H. The westward intensification of wind-driven ocean currents. *Trans. Am. Geophys. Union*, 29:202–206, 1948.
- [13] Sverdrup H.U. Wind-driven currents in a baroclinic ocean; with application to the equatorial currents of the eastern pacific. *Proc. Natl. Acad. Sci.*, 33:318–326, 1947.
- [14] Bjerknes J. Atlantic air-sea interaction. *Advances in Geophysics*, 10:1–82, 1964.
- [15] Marshall J., Hill C., Perelman L., and Adcroft A. Hydrostatic, quasi-hydrostatic, and nonhydrostatic ocean modeling. *J. Geophysical Res.*, 102(C3):5733–5752, 1997.
- [16] Marshall J., Hill C., Perelman L., Adcroft A., and Heisey C. A finite-volume, incompressible navier stokes model for studies of the ocean on parallel computers. *J. Geophysical Res.*, 102(C3):5753–5766, 1997.
- [17] Marshall J., Ferreira D., Campin J.-M., and Enderton D. Studies of the mean climate and variability of an atmosphere and ocean on an aqua-planet. *To appear in the Journal of the Atmospheric Sciences*, 2007.
- [18] Marshall J., Johnson H., and Goodman J. A study of the interaction of the north atlantic oscillation with ocean circulation. *Journal of Climate*, 14(7):1399–1421, 2001.
- [19] Hasselmann K. Stochastic climate models. part i: theory. *Tellus*, 28:473–485, 1976.
- [20] Winton M. A reformulated three-layer sea ice model. *Journal of Atmospheric and Oceanic Technology*, 17(4):525–531, 2000.
- [21] Cessi P. Thermal feedback on windstress as a contributing cause of climate variability. *J. Climate*, 13:232–244, 2000.
- [22] Gent P.R. and McWilliams J.C. Isopycnal mixing in ocean circulation models. *Journal of Physical Oceanography*, 20(1):150–155, 1990.
- [23] Saravanan R. and McWilliams J.C. Advective ocean-atmosphere interaction: an analytical stochastic model with implications for decadal variability. *Journal of Climate*, 11(2):165–188, 1997.
- [24] Seager R, Kushnir Y, Visbeck M, Naik N, Miller J, Krahnemann G, and Cullen H. Causes of atlantic ocean climate variability between 1958 and 1998. *Journal of Climate*, 13:2845–2862, 2000.

- [25] Bracewell R.N. *The Fourier transform and its applications*. McGraw-Hill, 1965. ISBN 0-07-007015-6.
- [26] White W.B. Annual forcing of baroclinic long waves in the tropical north pacific ocean. *Journal of Physical Oceanography*, 7:50–61, 1977.
- [27] Munk W.H. On the wind-driven ocean circulation. *J. Meteor.*, 7:79–93, 1950.
- [28] Kushnir Y. Interdecadal variations in north atlantic sea surface temperature and associated atmospheric conditions. *Journal of Climate*, 7:141–157, 1994.